DNA SELF-ASSEMBLY DRIVEN BY BASE STACKING

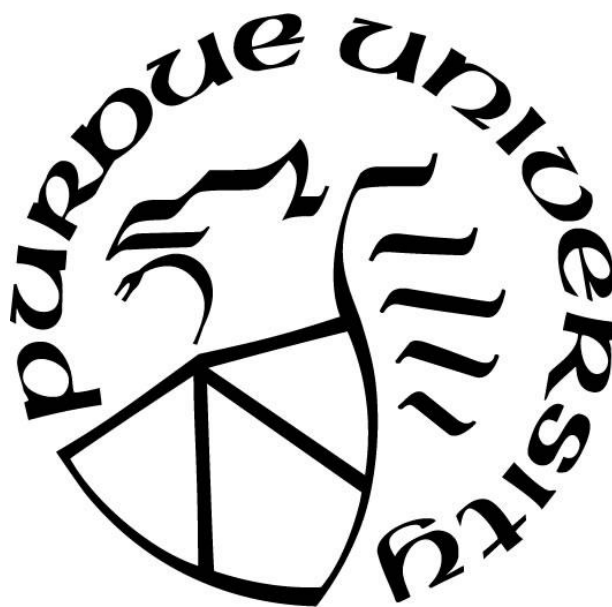by

Longfei Liu

A Dissertation

Submitted to the Faculty of Purdue University

In Partial Fulfillment of the Requirements for the degree of

Doctor of Philosophy

Department of Chemistry

West Lafayette, Indiana

May 2019

THE PURDUE UNIVERSITY GRADUATE SCHOOL
STATEMENT OF COMMITTEE APPROVAL

Dr. Chengde Mao, Chair
    Department of Chemistry
Dr. Hilkka Kenttämaa
    Department of Chemistry
Dr. Jianguo Mei
    Department of Chemistry
Dr. Garth Simpson
    Department of Chemistry

Approved by:
    Dr. Christine A. Hrycyna
        Head of the Graduate Program

For my dear parents and wife

ACKNOWLEDGMENTS

TABLE OF CONTENTS

LIST OF TABLES

LIST OF FIGURES

ABSTRACT

Author: Liu, Longfei. PhD
Institution: Purdue University
Degree Received: May 2019
Title: DNA Self-Assembly Driven by Base Stacking
Committee Chair: Chengde Mao

DNA nanotechnology has provided programming construction of various nanostructures at nanometer-level precision over the last three decades. DNA self-assembly is usually implemented by annealing process in bulk solution. In recent several years, a new method thrives by fabricating two-dimensional (2D) nanostructures on solid surfaces. My researches mainly focus on this field, surface-assisted DNA assembly driven by base stacking. I have developed methods to fabricate DNA 2D networks via isothermal assembly on mica surfaces. I have further explored the applications to realize quasicrystal fabrication and nanoparticles (NPs) patterning.

In this dissertation, I have developed a strategy to assemble DNA structures with 1 or 2 pair(s) of blunt ends. Such weak interactions cannot hold DNA motifs together in solution. However, with DNA-surface attractions, DNA motifs can assemble into large nanostructures on solid surface. Further studies reveal that the DNA-surface attractions can be controlled by the variety and concentration of cation in the bulk solution. Moreover, DNA nanostructures can be fabricated at very low motif concentrations, at which traditional solution assembly cannot render large nanostructures. Finally, assembly time course is also studied to reveal a superfast process for surface-assisted method compared with solution assembly.

Based on this approach, I have extended my research scope from 1D to 2D structures assembled from various DNA motifs. In my studies, I have successfully realized conformational change regulated by DNA-surface interaction and steric effect. By introduction of DNA duplex

"bridges" and unpaired nucleotide (nt) spacers, we can control the flexibility/rigidity of DNA nanomotifs, which helps to fabricate more delicate dodecagonal quasicrystals. The key point is to design the length of spacers. For 6-point-star motif, a rigid structure is required so that only 1-nt spacers are added. On the other hand, 3-nt spacers are incorporated to enable an inter-branch angle change from 60° to 90° for a more flexible 5-point-star motif. By tuning the ratio of 5 and 6 -point-star motifs in solution, we can obtain 2D networks from snub square tiling, dodecagonal tiling, a mixture of dodecagonal tiling and triangular tiling, and triangular tiling.

Finally, I have explored the applications of my assembly method for patterning NPs. Tetragonal and hexagonal DNA 2D networks have been fabricated on mica surfaces and served as templates. Then modify the surfaces with positively-charged "glues", *e.g.* poly-L-lysine (PLL) or Ni^{2+}. After that, various NPs have been patterned into designated lattices, including individual DNA nanomotifs, gold NPs (AuNPs), proteins, and silica complexes. Observed NP lattices and fast Fourier Transform (FFT) patterns have demonstrated the DNA networks' patterning effect on NPs.

CHAPTER 1.   INTRODUCTION

1.1   Overview of DNA Nanotechnology

DNA, or deoxyribonucleic acid, is a molecule carrying the genetic instructions used in the growth, development, functioning, and reproduction of all known living organisms and many viruses.[1] The concept of DNA nanotechnology was first brought up by Dr. Nadrian C. Seeman in the early 1980s.[2-4] In the following several decades, DNA has been exploited to construct various DNA nanostructures.[5-14] Based on the strict base pairing rule, in which adenine (A) pairs with thymine (T) and cytosine (C) pairs with guanine (G), DNA nanostructures can be designed and controlled with exceptional programmability and high precision.[15] This makes DNA nanotechnology broadly applicable in many fields, including inorganic nanostructure manipulations,[16-21] protein assembly,[22-27] biophysical and biomedical applications.[28-35]

1.1.1   DNA Double Helix

DNA double helix, also known as DNA duplex, contains two DNA strands, which hybridize with each other by base-pairing rule. Each DNA strand is composed of monomeric units called nucleotides. Each nucleotide contains three components: a sugar called deoxyribose, a phosphate group, and one of four nitrogen-containing nucleobases (Figure 1.1).[1]
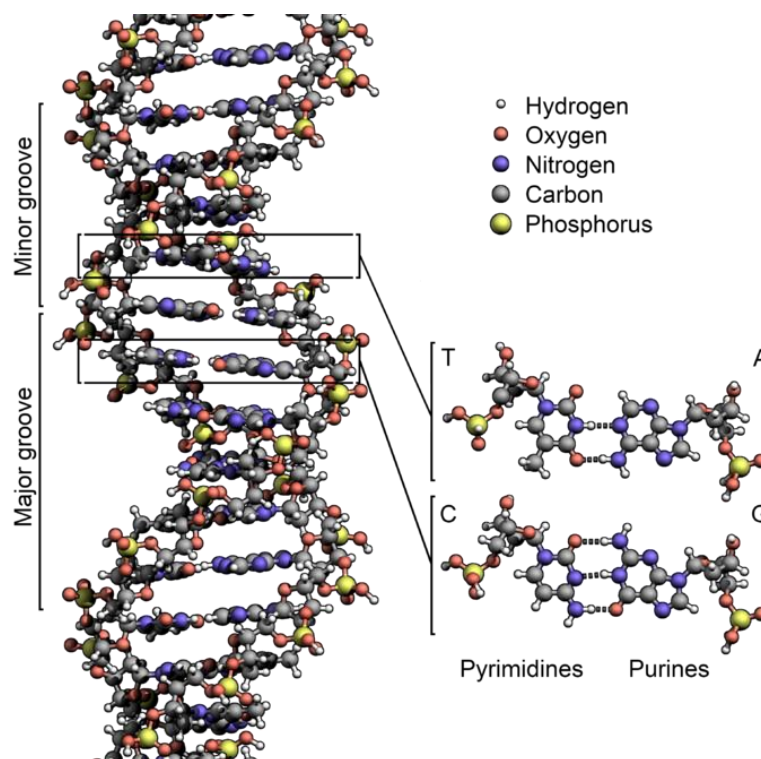
Figure 1.1. The structure of DNA double helix.[1]

The unique double helix structure of DNA was firstly revealed by Dr. Watson and Dr. Crick in 1953.[36] One DNA strand anti-parallelly associates with its complimentary strand via base-pairing rule. The base-pairing rule strictly regulates the DNA-DNA hybridization, which is determined by the four nitrogen-containing nucleobases (A, T, G, and C). A always pairs with T and G always pairs with C, recognized by inter-base hydrogen bonding (Figure 1.2). The most common formation of DNA duplex is a B-form right-handed helix structure, which has a diameter of 2 nm and a pitch of 3.4 nm. One turn of this type of duplex contains 10.5 base pairs. Besides B-DNA, other types are also reported, including left-handed Z-DNA and right-handed A-DNA. The differences among these three types of DNA duplexes are shown in Table 1.1.
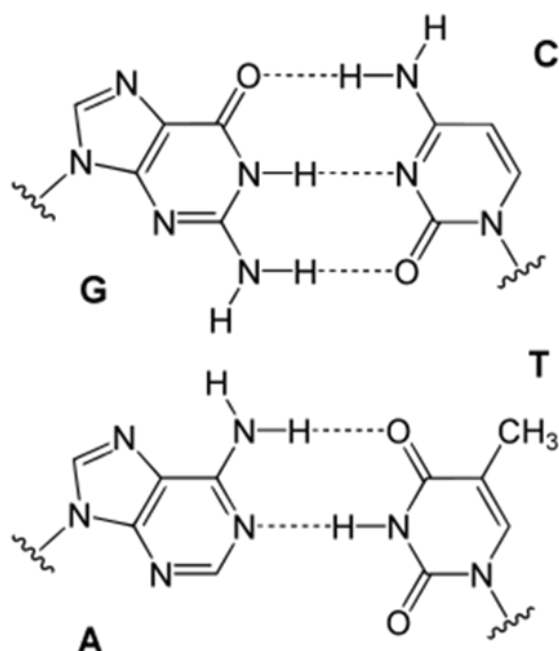
Figure 1.2. The depiction of DNA base pairs via hydrogen bonding.[37]

Table 1.1. Comparison between A, B, and Z-type DNA duplexes.[38]

Geometry attribute:	A-type	B-type	Z-type
Helix sense	right-handed	right-handed	left-handed
Repeating unit	1 bp	1 bp	2 bp
Rotation/bp	32.7°	34.3°	60°/2
Mean bp/turn	11	10.5	12
Inclination of bp to axis	+19°	−1.2°	−9°
Rise/bp along axis	2.6 Å (0.26 nm)	3.4 Å (0.34 nm)	3.7 Å (0.37 nm)
Rise/turn of helix	28.6 Å (2.86 nm)	35.7 Å (3.57 nm)	45.6 Å (4.56 nm)
Mean propeller twist	+18°	+16°	0°
Glycosyl angle	anti	anti	pyrimidine: anti, purine: syn
Nucleotide phosphate to phosphate distance	5.9 Å	7.0 Å	C: 5.7 Å, G: 6.1 Å
Sugar pucker	C3'-endo	C2'-endo	C: C2'-endo, G: C3'-endo
Diameter	23 Å (2.3 nm)	20 Å (2.0 nm)	18 Å (1.8 nm)

1.1.2   The Principle of DNA Nanotechnology - Branched DNA Molecules and Sticky-Ended Cohesion

In nature, DNA exist as double helices in which two DNA strands are associated following the base-pairing rule. However, this kind of interaction can only render one-dimensional (1D) nanostructures, which is not available for complicated two-dimensional (2D) or three-dimensional (3D) systems. This problem was firstly solved by the proposal of branched DNA molecules.[3,4] In 1983, Dr. Seeman brought up the scheme of branched DNA molecule, a four-way Holliday junction structure (Figure 1.3). The branched DNA molecule contains four 16-nt, single-stranded DNAs. Due to the unique sequence of DNA strands, the junction point cannot migrate thus a stable four-way structure survives with each branch containing 8-base pair (bp) duplex. This design a landmark of the early DNA nanotechnology because it enables development of DNA structures from 1D to 2D.
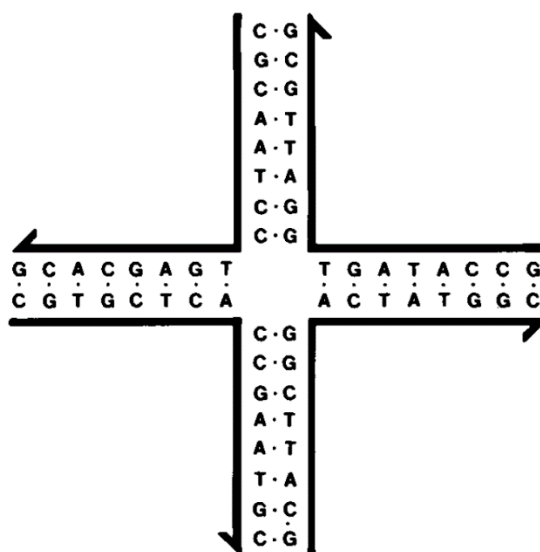
Figure 1.3. The structure of DNA four-way junction.[3]

Another problem is how to associate individual DNA motifs into large DNA architectures. The most commonly used linkage is sticky-ended cohesion (Figure 1.4). Single-stranded overhangs from two different DNA duplexes can hybridize to form a long, continuous duplex when they are complementary to each other. Combining these two principles, large DNA architectures can be readily fabricated (Figure 1.5).
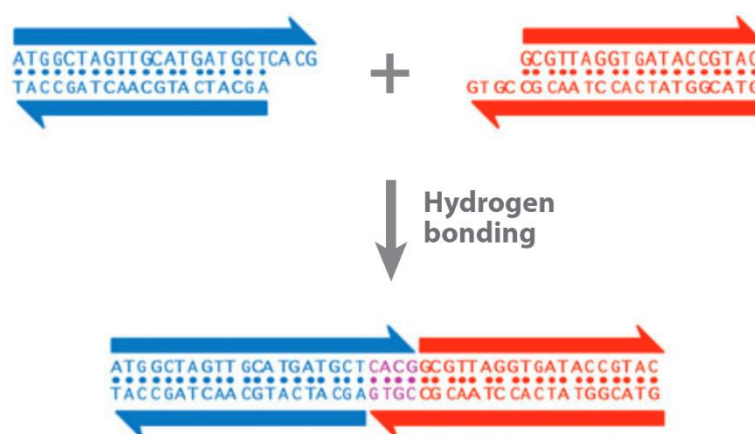
Figure 1.4. Scheme of the sticky-ended cohesion.[39]
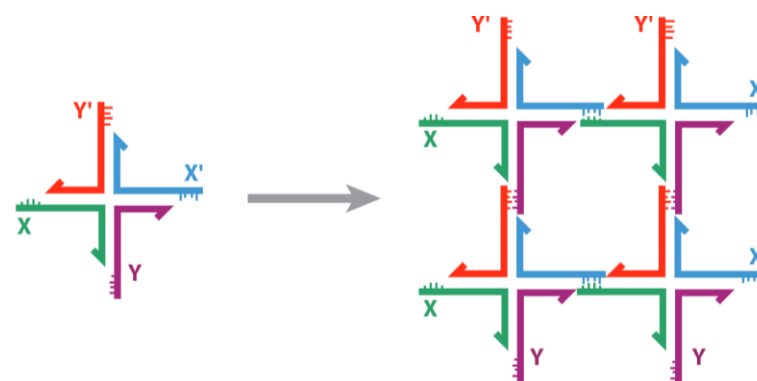
Figure 1.5. Self-assembly of branched DNA molecules to form larger arrangements.[39]

1.1.3 Procedures for DNA Self-Assembly

Over the last several decades, scientists have fabricated many DNA architectures. Meanwhile, a mature methodology has been established and many tools have been developed for designing, modeling, and assembling DNA nanostructures. The general protocol is (1) designing the DNA structures and sequences; (2) synthesizing and purifying (if needed) DNA strands; (3) mixing DNA strands at designated ratio and undergoing a slow thermal cooling process, known as slow annealing process. Several software tools are useful for the first step: Tiamat is to edit and display complex DNA structures in 3D;[40] SEQUIN is to design DNA sequence for minimizing sequence symmetry and mismatches; CADNano is to design complex DNA origami structures and sequences of staple strands. In the second step, short DNA strands (usually shorter than 100 bases) are commercially available. But these DNA strands usually need purification by either denaturing gel electrophoresis or HPLC (high-performance liquid chromatography). In the final step, DNA strands are usually mixed in tris base buffer at pH ~ 8, adding ~ 10 mM Mg^{2+}. The Mg^{2+} is used to eliminate electrostatic repulsion between DNA backbones. The characterization methods include native PAGE, AFM, and EM for different purposes.

1.1.4 DNA 2D Structures

The construction of 2D lattices had been discussed with the introduction of the concept of branched DNA molecules.[2] However, the first DNA 2D lattice was reported in 1998 assembled from double crossover (DX) molecules.[11] Out of five proposed DX molecules, only two stable DX molecules were fabricated.[41] They are called DAO (double crossover, antiparallel, odd spacing) and DAE (double crossover, antiparallel, even spacing), as shown in Figure 1.6. DAO has an odd number of half-turns between the crossover points, while DAE has an even number of half-turns.

The assembled DX 2D lattices were characterized by AFM and confirmed with expected periodicity (Figure 1.7).
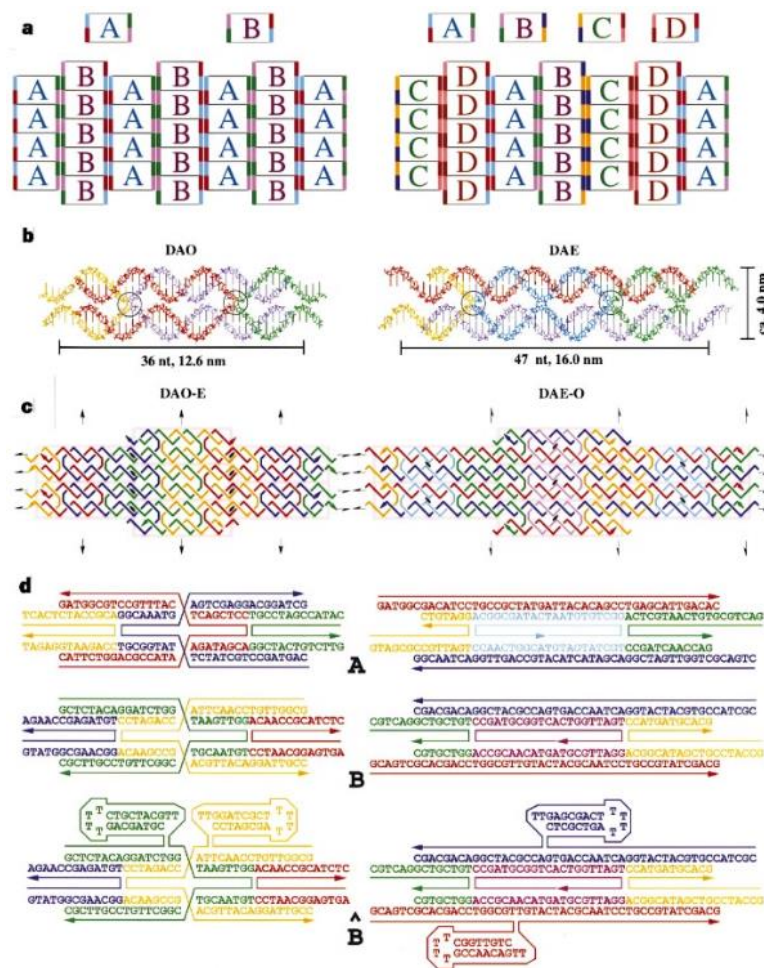
Figure 1.6. Design of DNA 2D lattices assembled from DX molecules.[11]
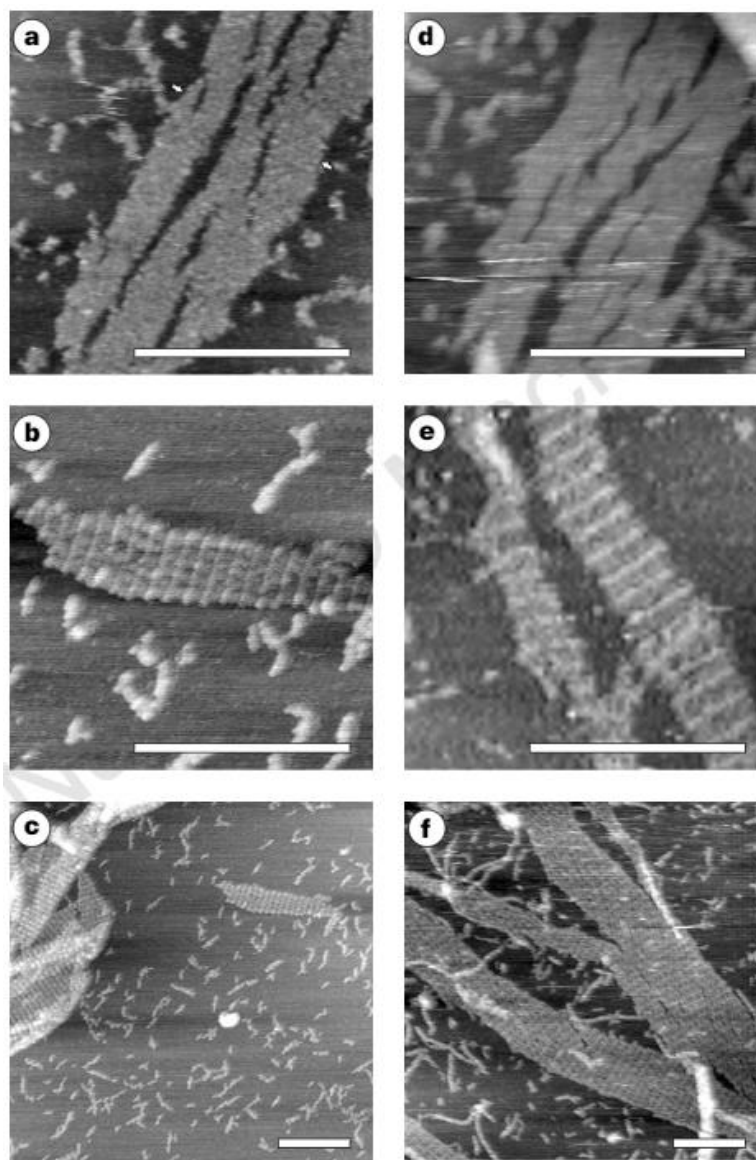
Figure 1.7. AFM images of DX 2D lattices assembled from (a-c) DAO molecules and (d-f) DAE molecules. Scale bar: 300 nm.[11]

Based on the DX structure, many DNA motifs have been designed and successfully assembled into 2D lattices.[42-51] Another series of DNA 2D lattices rely on symmetry of the point-star motifs (Figure 1.8).[52-55] In this design, all the branches of DNA motifs are identical. With this symmetry strategy, only three different DNA strands are needed to assemble designated 2D lattices. For example, in Figure 1.8 a, a three-point-star motif contains three identical branches assembled

from three different strands. Then the hexagonal arrays can be fabricated due to the motif's three-fold symmetry.
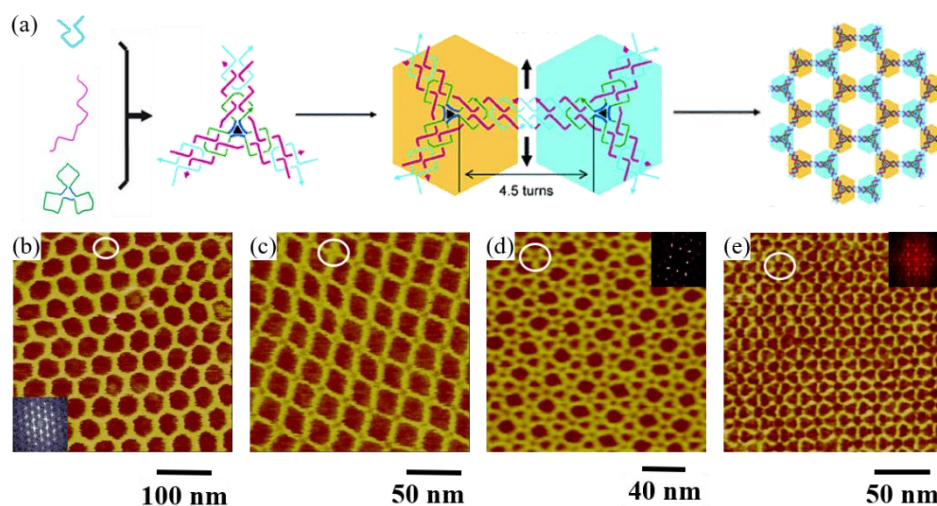
Figure 1.8. DNA 2D lattices assembled from point-star motifs. (a) Hexagonal arrays assembled from three-point-star motifs. AFM images of 2D lattices assembled from (b) 3, (c) 4, (d) 5, and (e) 6 -point-star motifs. Individual motifs are circled.[52-55]

Besides the tile-based assembly of DNA 2D structures, another strategy uses one long DNA strand (scaffold strand) and hundreds of short DNA strands with unique sequences (staple strands) to fabricate DNA origami. The first DNA origami was reported in 2006 by Dr. Rothemund.[13] In his method, a 7-kilobase, single-stranded virus DNA was used as the scaffold strand and hundreds of short single-stranded DNA served as staple strands (Figure 1.9). How scaffold strand folded depended on the sequence of short staple strands. Based on this approach, many DNA origami shapes were successfully fabricated (Figure 1.10). DNA origami is another landmark of DNA nanotechnology, which have been broadly in programmable nanomaterial fabrication.
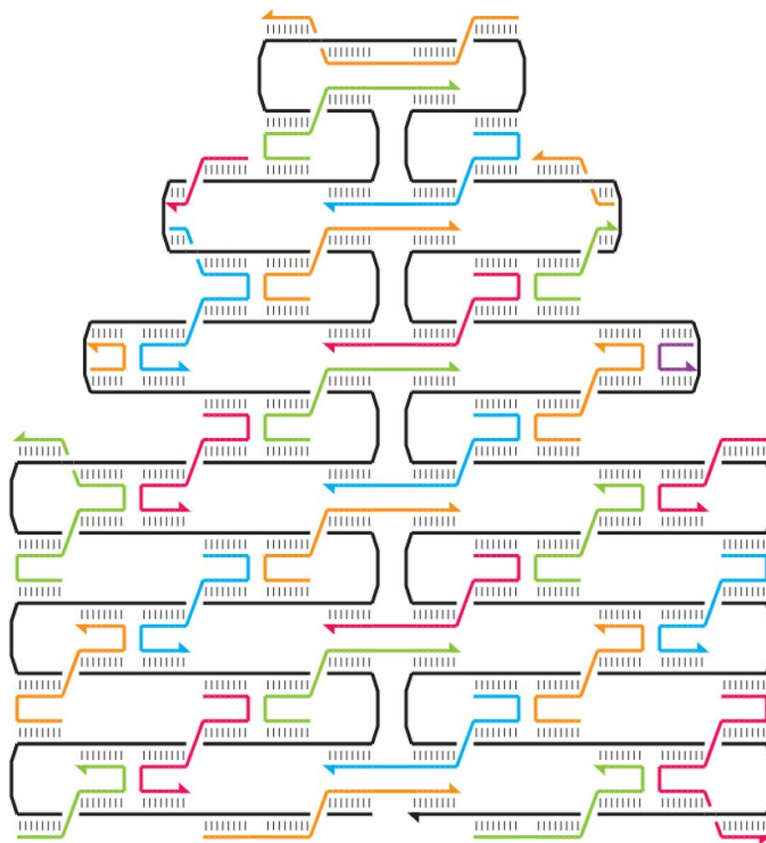
Figure 1.9. Scheme of a DNA origami design. The long, black strand is the scaffold strand. All the other short strands are staple strands.[13]
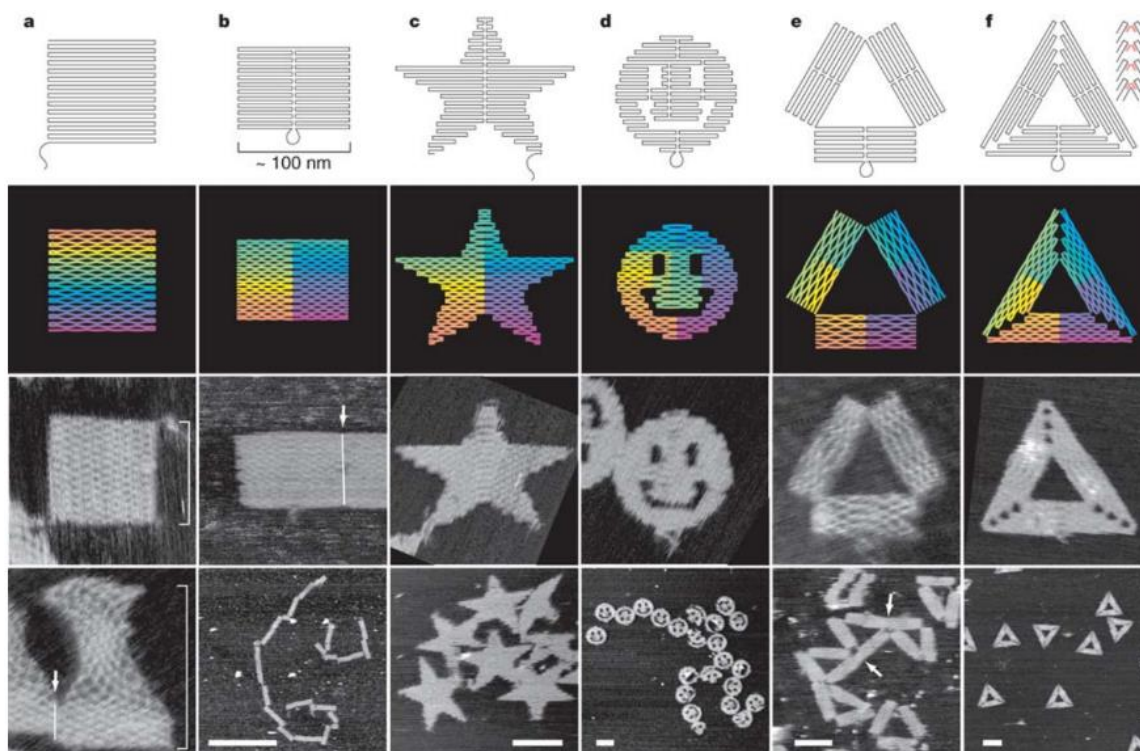
Figure 1.10. DNA origami shapes. (a) Square. (b) Rectangle. (c) Star. (d) Disk with three holes. (e) Triangle with rectangular domains. (f) Sharp triangle with trapezoidal domains and bridges between them. Top panel: folding path. Second row from top: diagrams showing the bend of helices at crossovers (where helices touch) and away from crossovers (where helices bend apart). Color indicates the base-pair index along the folding path; red is the 1st base, purple the 7,000th. Bottom two rows: AFM images. Scale bars for lower AFM images: b, 1 mm; c–f, 100 nm.[13]

1.1.5 DNA 3D Structures

3D structures have more versatile applications compared with 2D structures. DNA nanocages, 3D DNA origami, and 3D DNA crystals are three most important study directions. In the early 1990s, Dr. Seeman and coworkers reported a ligation-based approach to construct 3D DNA nanostructures: cube and truncated octahedron.[56,57] Later, one-pot assembly of DNA tetrahedron and bipyramid was by Dr. Turberfield and coworkers.[58,59] In 2007, Dr. Sleiman reported a discrete DNA assembly method to fabricate a series of nanocages.[60] Figure 1.11 showed some of the nanocages above.
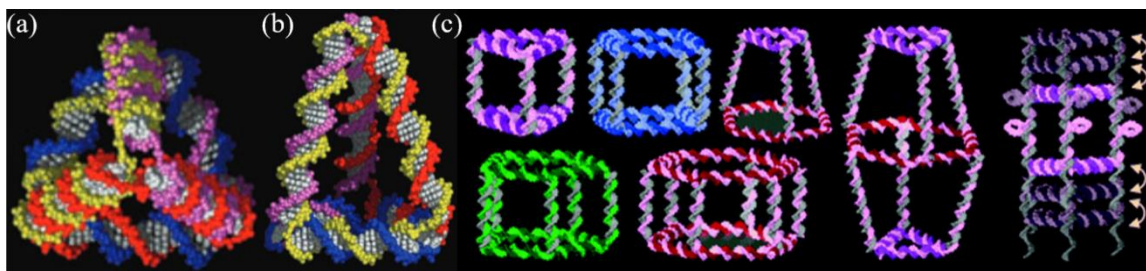
Figure 1.11. DNA nanocages. (a, b) Tetrahedra by Dr. Turberfield.[58] (c) A series of discrete DNA nanocages by Dr. Sleiman.[60]

Another approach to fabricate DNA nanocages is to use symmetric motifs with controlled flexibility, which successfully construct 2D lattices. In 2008, Dr. Mao and coworkers reported a series of DNA polyhedra assembled from symmetric point-star motifs, including tetrahedron, dodecahedron and buckyball (Figure 1.12).[61] Following this strategy, more polyhedral were constructed from other point-star motifs.[54,62-64]
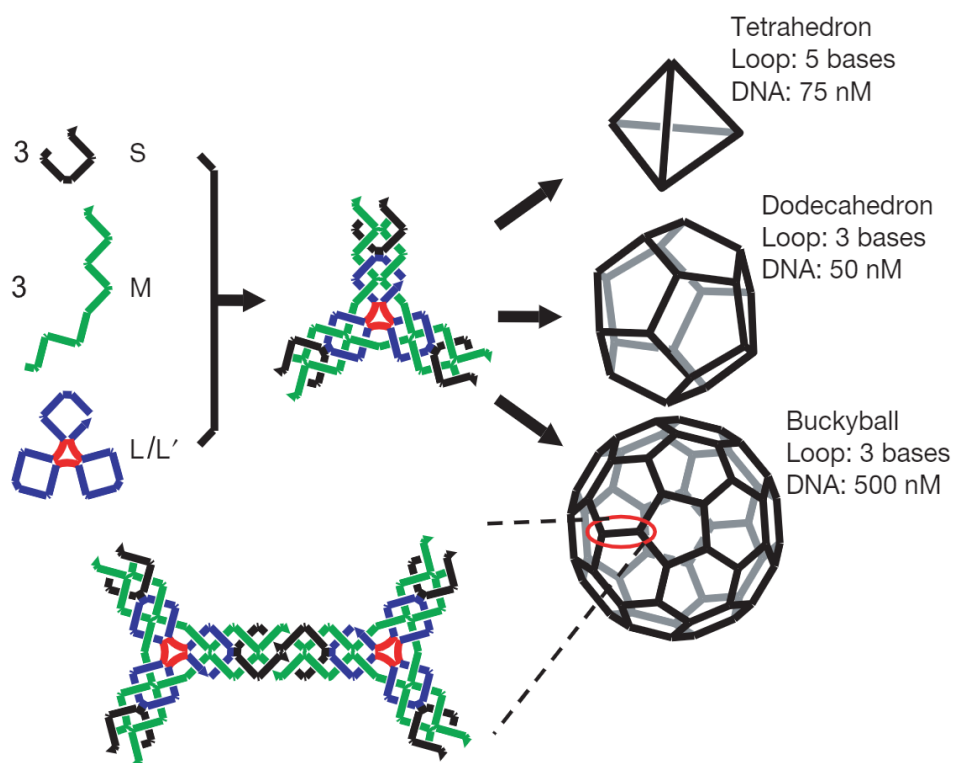
Figure 1.12. Self-assembly of DNA polyhedral assembled from three-point-star motifs. Three different types of DNA single strands stepwise assemble into symmetric three-point-star motifs(tiles) and then into polyhedra in a one-pot process. There are three single-stranded loops (colored red) in the center of the complex. The final structures (polyhedra) are determined by the loop length (3 or 5 bases long) and the DNA concentration.[61]

DNA origami strategy has been demonstrated to fold long, single-stranded strands into 2D shapes since 2006. Recently, complicated 3D nanostructures have also been well studied by this strategy. In 2009, Dr. Shih and coworkers developed DNA 3D origami by folding and twisting 2D helix bundles (Figure 1.13) .[65,66] In 2015, Dr. Högberg brought up a triangulated strategy to fabricate 3D meshes with optimized structural rigidity (Figure 1.14 and 1.15).[67]
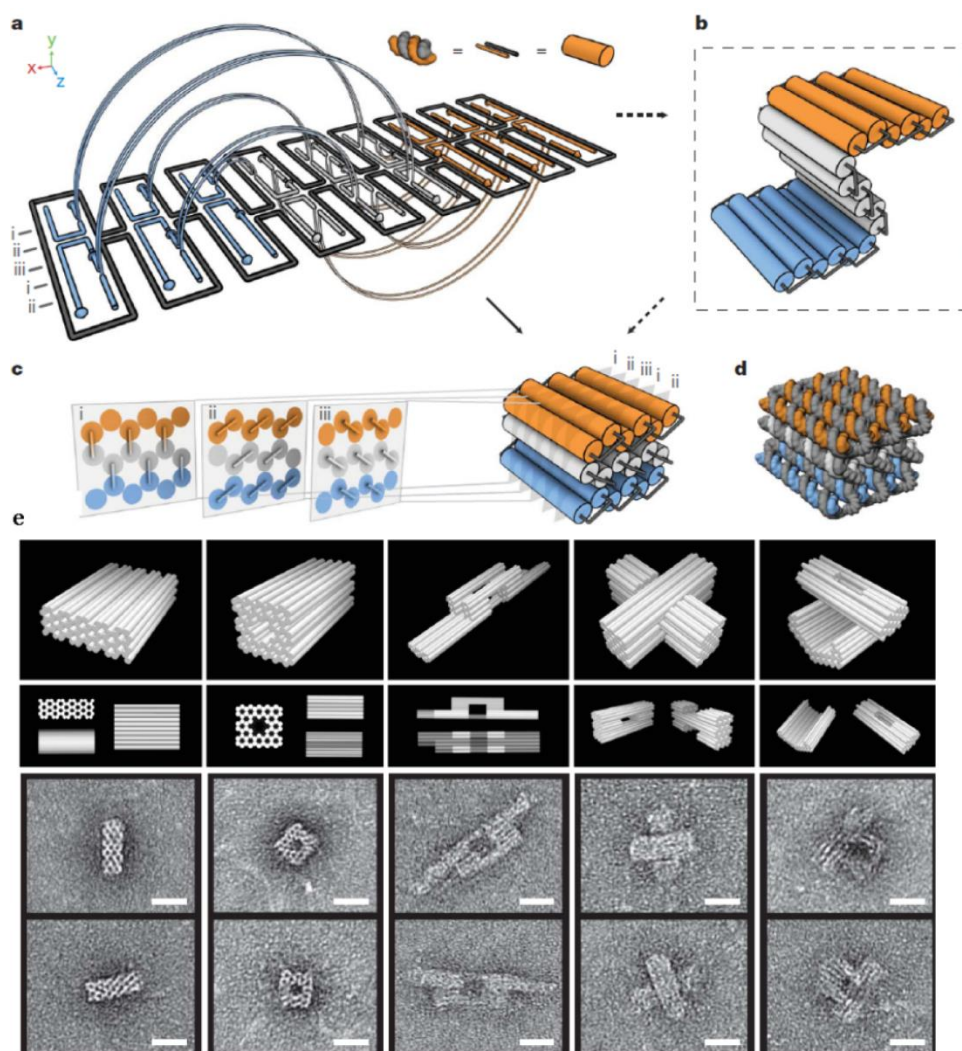
Figure 1.13. DNA 3D origami from folded and twisted helix bundles. (a-d) Design of 3D DNA origami. (e) TEM micrographs of designed 3D origami shapes. Scale bar: 20 nm.[65]
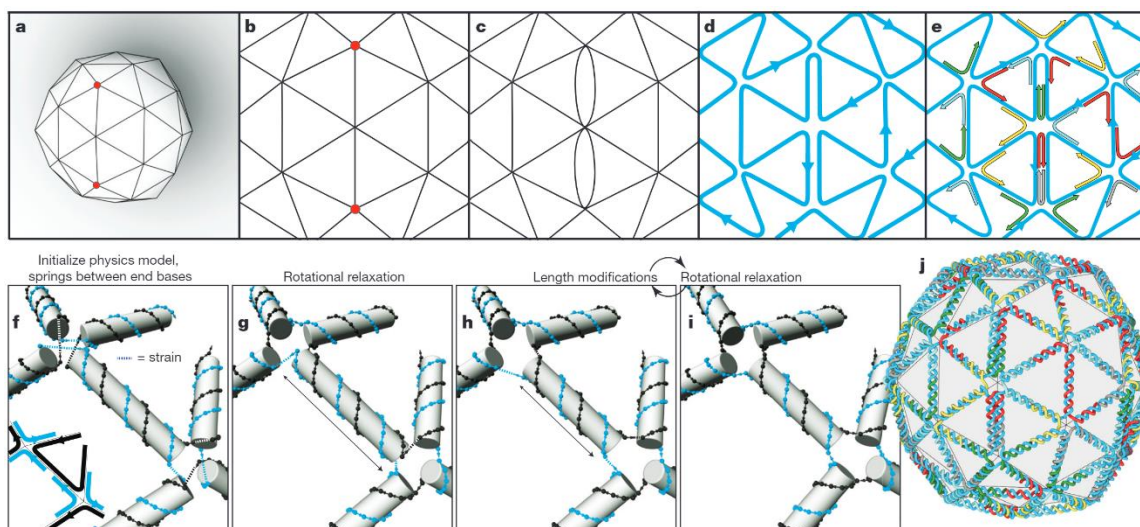
Figure 1.14. Design paradigm and automated workflow for scaffold-routing sequence design of origami 3D meshes. (a) Drawing of 3D meshes. (b-e) Design of scaffold route and staple strands. (f-i) Optimization of designed structures by relaxation and even distribution of strain. (j) Final design of 3D meshes.[67]
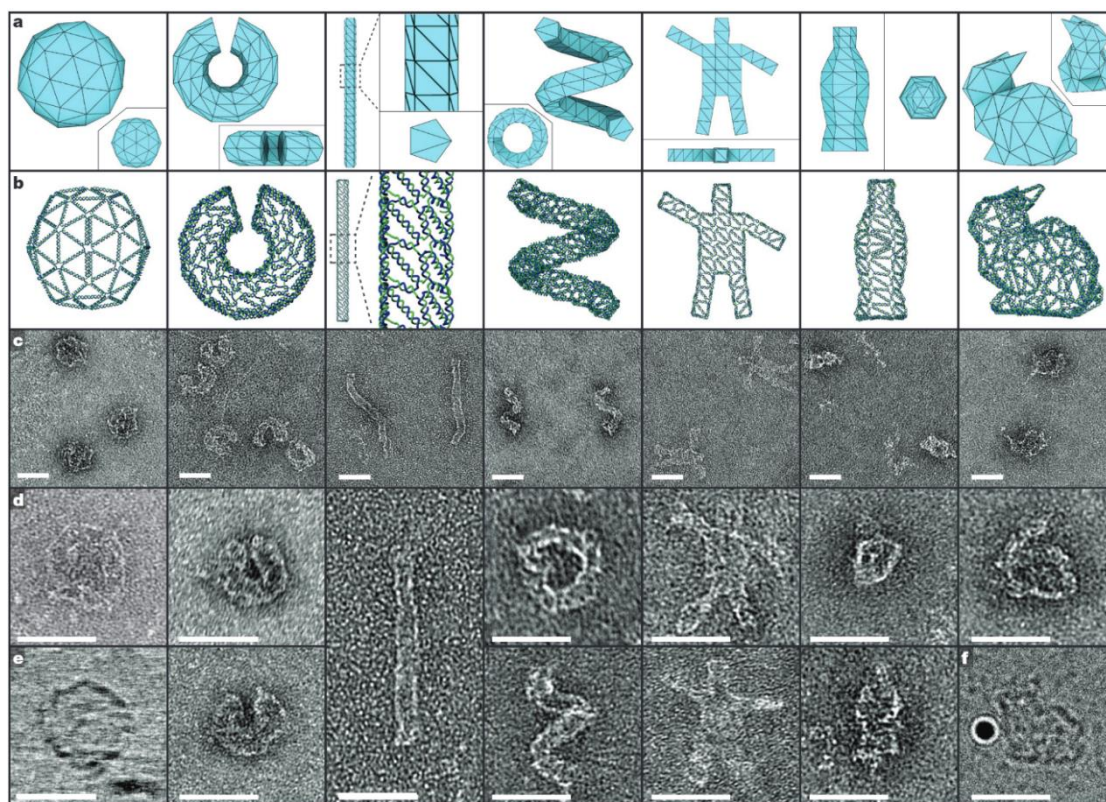
Figure 1.15. DNA 3D meshes. (a-b) 3D meshes and designed DNA structures. (c-e) TEM micrographs of designed 3D structures.[67]

DNA 3D crystals are another challenging but important structures in DNA nanotechnology. In 2009, Dr. Mao and Dr. Seeman rationally designed and successfully fabricated the first DNA 3D crystals (Figure 1.16).[68] This crystal was assembled by identical DNA triangle motifs. Crystallography agreed with designed crystal structures.
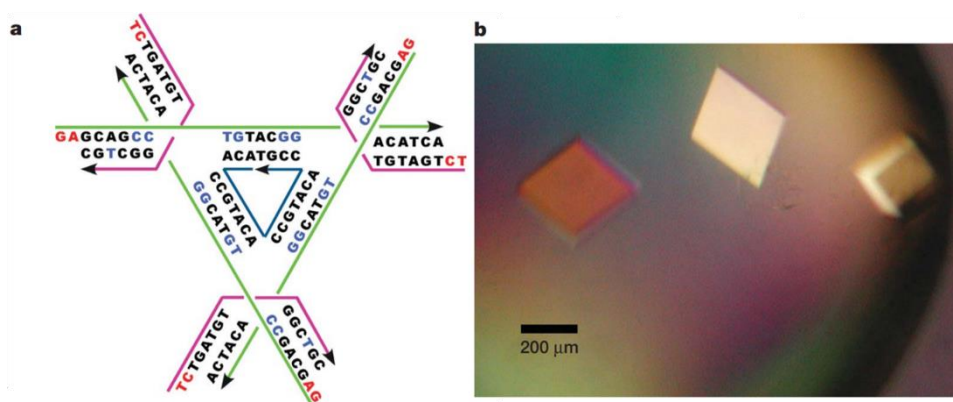
Figure 1.16. Schematic drawing, sequence, and optical image of crystal. (a) Schematic design. The sequences of the strands are shown in figure. (b) Optical image of crystal.[68]

1.2 DNA Self-Assembly Driven by Base Stacking

DNA self-assembly commonly relies on sticky-ended cohesion between individual motifs. The association between two complementary strands is strengthened by hydrogen bonding and stacking interaction. Contrary to popular belief, stabilization mainly relies on stacking interaction instead of hydrogen bonding.[37,69] In recent several years, DNA assembly based on base stacking interaction has been extensively studied. And new strategies have been developed to apply this "weak" force for DNA self-assembly.

1.2.1 Base Stacking

Base stacking is one of the most important factors to stabilize the DNA double helix. In 2016, Dr. Dietz and coworkers measured the strength of base-pair stacking on the level of single particles by two tethered DNA origami beams that feature parallel arrays of blunt-ended DNA double helices.[70] They also utilized the blunt-ended base stacking force to fabricate dynamic 3D DNA devices and reversibly control the shape changes by cation concentration and temperature.[71] In solution, DNA assembly mediated blunt-ended base stacking is still less efficient compared with sticky-ended cohesion. Cation concentration, temperature and the number of blunt ends can dramatically influence the stability of assembled DNA structures due to the bending force perpendicular to the stacking axis.

1.2.2 Surface-Assisted DNA Assembly

Although DNA assembly is less stable mediated by blunt-ended base stacking in solution, its behavior is quite different on solid surface. DNA-surface interaction helps to eliminate the bending force, which can further stabilize the DNA 2D structures. In 2006, Dr. Rothemund noticed that the blunt-ended base stacking associated DNA origami into continuous patterns.[13] Later, he applied the base stacking from multiple blunt ends into the fabrication of 2D DNA origami lattice.[72] In recent several years, this interaction was broadly used by other scientist.[73,74]

One question is what the minimum number of blunt ends is strong enough to associate DNA motifs on the surface. In 2010, Dr. Seeman and coworkers successful fabricated linear structures by using three blunt ends.[75] Later, Dr. Sleiman assembled 2D lattices from point-star motifs with only two blunt ends.[76] In her work, the DNA-surface interaction was based on lipid bilayers. What

happens if only one blunt end exists? How can DNA-surface interaction be controlled? These questions will be answered in this dissertation.

CHAPTER 2.   REGULATING DNA SELF-ASSEMBLY BY DNA–SURFACE INTERACTIONS

2.1   Introduction

DNA has been well studied to construct various nanostructures in the last several decades.[2-14] Most of structures have been fabricated in solution via sticky-ended cohesion. Weak interaction from one or two pairs of blunt-ended stacking cannot hold DNA motifs together. However, this weak interaction can be stabilized by DNA-surface interaction to allow DNA motifs to assemble into large nanostructures. Recent studies on DNA assembly on surface have revealed many potential advantages,[72-76,78-80] e.g. reduced conformational freedom and higher structural rigidity.[78,79] However, the effect of DNA-surface interaction has barely explored. Moreover, what happens if only one blunt end exists? How can DNA-surface interaction be controlled? These questions still need to be studied.

2.2   Scheme and Design

The scheme is shown in Figure 2.1. When DNA solution (light blue) contacts a mica surface (yellow), DNA molecules will loosely adsorb onto mica surface, then rearrange themselves on the surface to maximize base stacking (highlighted by dashed boxes) between blunt ends.
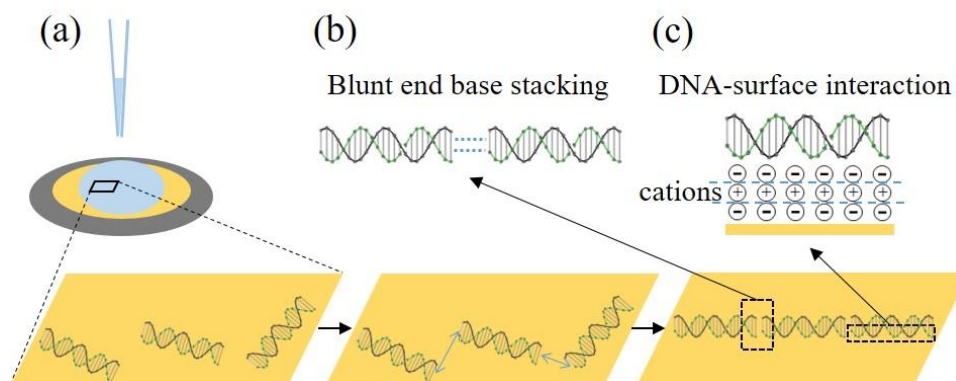
Figure 2.1. Process of blunt-end stacking-driven DNA self-assembly on mica surface. (a) Step-wise illustration of assembly process. (b) Close-up view of the blunt-end interaction. (c) DNA-surface attraction via salt bridge.

All DNA motifs used in this study are shown in Figure 2.2. All the branches of each motif are blunt-ended at peripheral site.

Figure 2.2. Scheme of DNA motifs with sequences.

2.3 Materials and Methods

2.3.1 DNA Oligonucleotides

All oligonucleotides were purchased from IDT, Inc. and purified by 10% - 20% denaturing PAGE. Oligonucleotides from all tiles are listed below with their designated ratio and concentration during *in situ* assembly:

(1) Short DNA duplex, ratio 1:1, 10 µM in TAE/Mg^{2+} solution:

D1: 5'-CGAAGTGTAATGTGACGCAACCTC-3'

D2: 5'-GAGGTTGCGTCACATTACACTTCG-3'

(2) DX tile, ratio 1:2:2, 1 μM in TAE/Mg^{2+} solution:

1: 5'-CCAGGCACCATCGTAGGCTTGCCAGGCACCATCGTAGGCTTG-3'

2: 5'-ACTATGCAACCTGCCTGGCAAGCCTACGATGGACACGGTAACG-3'

3: 5'-CGTTACCGTGTGGTTGCATAGT-3'

(3) 3-point-star tile, ratio 1:3:3, 1 μM in TAE/Mg^{2+} solution:

Y-1: 5'- AGGCACCATCGTAGGTTTCTTGCCAGGCACCATCGTAGGTTTCTTGCCAG

GCACCATCGTAGGTTTCTTGCC-3'

2: 5'-ACTATGCAACCTGCCTGGCAAGCCTACGATGGACACGGTAACG-3'

3: 5'-CGTTACCGTGTGGTTGCATAGT-3'

(4) 4-point-star tile, ratio 1:4:4, 1 μM in TAE/Mg^{2+} solution:

X-1: 5'-AGGCACCATCGTAGGTTTTCTTGCCAGGCACCATCGTAGGTTTTCTTGCCA

GGCACCATCGTAGGTTTTCTTGCCAGGCACCATCGTAGGTTTTCTTGCC-3'

2: 5'-ACTATGCAACCTGCCTGGCAAGCCTACGATGGACACGGTAACG-3'

3: 5'-CGTTACCGTGTGGTTGCATAGT-3'

(5) D6aJ tile, ratio 2:2, 400 nM in TAE/Mg^{2+} solution:

J1: 5'-CGACTTAGACTTCAGGCCTGAAGTGTTCAAGGCCTTGAACGGTTATCCGGA

TAACCTGATGCAC-3'

J2: 5'-GTGCATCACGCG<u>TTTT</u>CGCGCTAAGTCG-3'

(6) D6aJ* tile, ratio 2:2, 400 nM in TAE/Mg^{2+} solution:

J1: 5'-CGACTTAGACTTCAGGCCTGAAGTGTTCAAGGCCTTGAACGGTTATCCGGA

TAACCTGATGCAC-3'

J2*: 5'-GTGCATCACGCATGCCGTTTTCGGCATGCGCTAAGTCG-3'

2.3.2 Assembly of Individual DNA Motifs

Mix DNA single strands at designated ratio for each DNA tile in TAE/Mg^{2+} solution (containing 40 mM tris base, 20 mM acetic acid, 2 mM EDTA, and 12.5 mM magnesium acetate; pH is adjusted to 8.0) to give final 10 μM (for short duplex) 400 nM (for D6aJ and D6aJ*) or 1 μM (for all the other tiles) tile solution. Sequentially incubate the DNA solutions: 95 °C for 5 minutes, 65 °C for 30 minutes, 50 °C for 30 minutes, 37 °C for 30 minutes, 22 °C for 30 minutes to 4 °C for 60 minutes.

2.3.3 Native Polyacrylamide Gel Electrophoresis (PAGE)

Mix 2 mL 40% acrylamide/bisacrylamide solution (19:1, 5% crosslinker), 2 mL 10× TAE/Mg^{2+} buffer, and 16 mL distilled water to prepare 4% native PAGE gel. Mix 3 mL 40% acrylamide/bisacrylamide solution (19:1, 5% crosslinker), 2 mL 10× TAE/Mg^{2+} buffer, and 15 mL distilled water to prepare 6% PAGE gel. Mix 4 mL 40% acrylamide/bisacrylamide solution (19:1, 5% crosslinker), 2 mL 10× TAE/Mg^{2+} buffer, and 14 mL distilled water to prepare 8% PAGE gel. The running buffer was TAE/Mg^{2+} buffer. Gels were run on a FB-VE10-1 electrophoresis unit (FisherBiotech) at 4 °C (300V, constant voltage) for 2 or 3 hours. After electrophoresis, the gels were stained with Stains-all dye (Sigma) and scanned.

2.3.4   Surface Self-Assembly

Mix annealed DNA tile (in TAE/Mg^{2+}) solution with TAE/Mg^{2+} –Ni^{2+} (40 mM tris base, 20 mM acetic acid, 2 mM EDTA, 12.5 mM magnesium acetate, and designated concentration of nickel chloride) buffer to prepare final DNA tile in TAE/Mg^{2+} – Ni^{2+} solution. Drop 5 µL final DNA tile solution onto a freshly cleaved mica surface, incubate for 5 minutes (time may differ unless otherwise mentioned) at room temperature, then add 25 µL corresponding TAE/Mg^{2+} – Ni^{2+} buffer and followed by AFM image in fluid.

2.3.5   AFM Image

AFM images were captured by MultiMode 8 (Bruker) using ScanAsyst-fluid mode with ScanAsyst-fluid+ probes (Bruker). The tip-surface interaction was automatically adjusted to optimize the scan set-point.

2.4   Results and Discussion

2.4.1   3-Point-Star Motifs

3-point-star motif contains three identical branches. Each branch contains two parallel blunt-ended DNA duplexes. The interaction between two such motifs is only two pairs of blunt-ended stacking. This interaction is too weak to associate motif together in solution. Therefore, no large structure has been observed in native PAGE (Figure 2.3). However, on mica surface, this interaction is strong enough to associate 3-point-star motifs into designed, honeycomb-like 2D arrays (Figure 2.4).
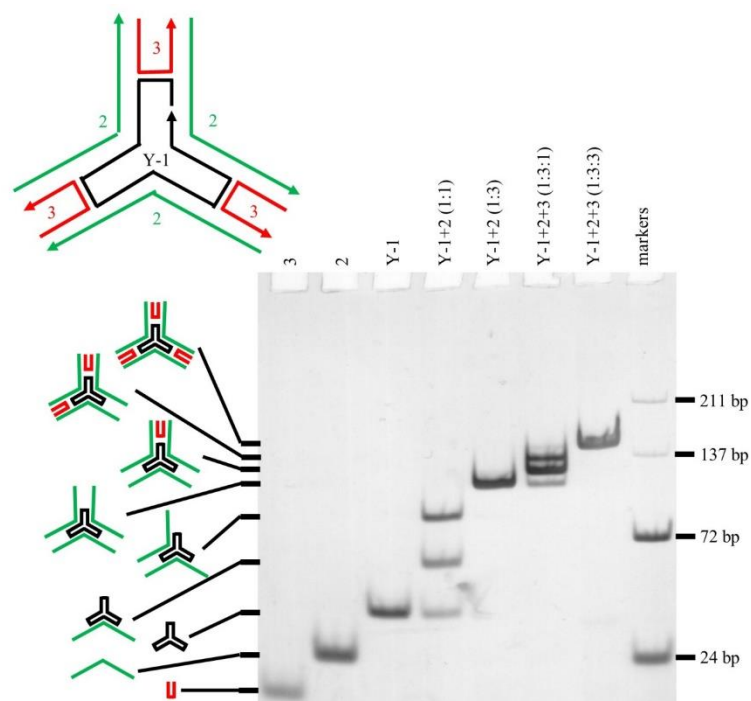
Figure 2.3. Native PAGE (6%) analysis of 3-point-star motif.
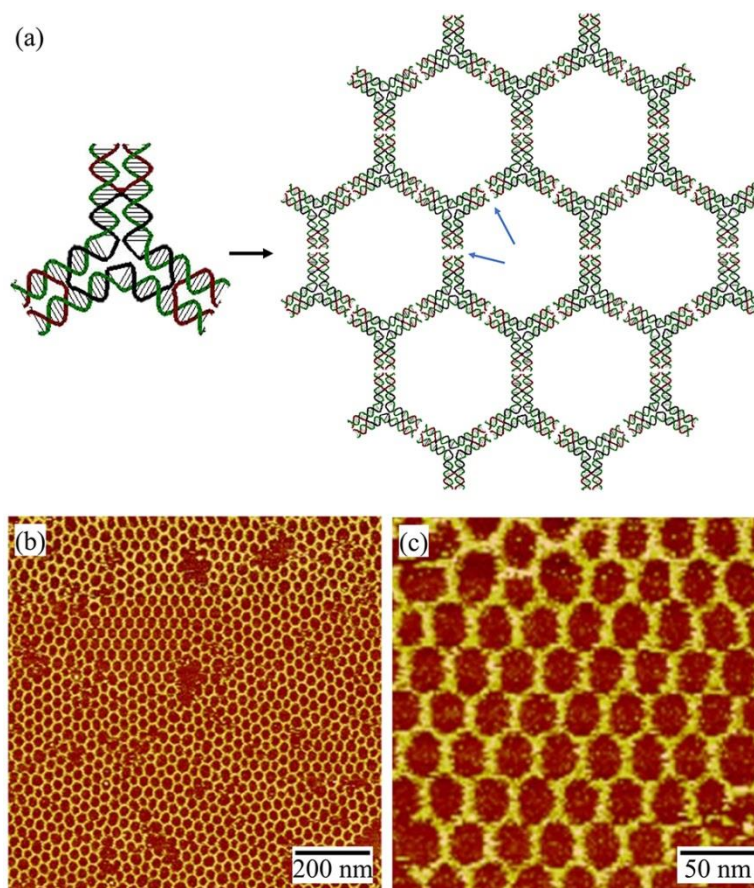
Figure 2.4. Hexagonal 2D arrays assembled from blunt-ended 3-point-star motif. (a) Scheme. Blue arrows point blunt-ended stacking sites. (b) and (c) A pair of atomic force microscopy (AFM) images of the DNA arrays at different magnifications.

Three main factors can influence DNA self-assembly on surface. Here, we use 3-point-star motif to study these three factors. *(1) DNA-surface interaction regulated by Ni^{2+} concentration ([Ni^{2+}]).* Ni^{2+} is an effective bridge between negatively charged DNA molecules and negatively charged mica surface, which can induce stronger interaction than commonly used Mg^{2+} can.[81] How strong DNA-surface interaction is depends on [Ni^{2+}]. Too low [Ni^{2+}] will not provide enough attractive force for DNA to absorb on surface; too high [Ni^{2+}] will result in too strong DNA-surface attraction and hinder DNA mobility and rearrangement on surface. Our experiments have confirmed this theoretical reasoning (Figure 2.5). In our experiment, 100 nM pre-assembled DNA

3-point-star motif in TAE/Mg^{2+} – Ni^{2+} buffer (containing 2 mM EDTA, 12.5 mM Mg^{2+}, and Ni^{2+}) is deposited onto mica surface and incubated for 3 min at room temperature, then followed by AFM imaging. Considering that the association constant of Ni^{2+}-EDTA is 10^{10} times stronger than that of Mg^{2+}-EDTA,[82] the added 2 mM Ni^{2+} is completely chelated by EDTA. So no array is detected at 2 mM Ni^{2+}. When 3 mM Ni^{2+} is added, 1 mM free Ni^{2+} exists and promotes the 2D array formation. When 4 mM Ni^{2+} is added, regular 2D arrays form with high coverage, and great durability. At even higher [Ni^{2+}] (5 mM), 2D arrays start to contain defects. Presumably, intense DNA-surface interaction hinders the DNA motifs to move on the surface for rearrangement. This result shows that moderate [Ni^{2+}] provide the optimal conditions for DNA assembly on mica surfaces.

(a) 2 mM

4 μm × 4 μm (insets with 500 nm × 500 nm)

(b) 3 mM

4 μm × 4 μm   1 μm × 1 μm   250 nm × 250 nm

(c) 4 mM

4 μm × 4 μm   1 μm × 1 μm   250 nm × 250 nm

(d) 5 mM

4 μm × 4 μm   1 μm × 1 μm   250 nm × 250 nm

Figure 2.5. Effect of Ni^{2+} concentration on 2D assembly of blunt-ended 3-point-star motif on mica as studied by AFM imaging. Experiment condition: in TAE/Mg^{2+} buffer plus indicated Ni^{2+} concentration, assembly: 3 minutes at 25 °C, 100 nM DNA 3-point-star motif.

Figure 2.5 continued

(e) 6 mM

4 μm × 4 μm   1 μm × 1 μm   250 nm × 250 nm

(f) 7 mM

4 μm × 4 μm   1 μm × 1 μm   250 nm × 250 nm

(g) 8 mM

4 μm × 4 μm   1 μm × 1 μm   250 nm × 250 nm

(h) 10 mM

4 μm × 4 μm   1 μm × 1 μm   250 nm × 250 nm

(2) DNA concentration (Figure 2.6). In TAE/Mg^{2+} - 4 mM Ni^{2+} solution, 100-600 nM DNA 3-point-star motifs form regular hexagonal 2D arrays with high surface coverage. Some defects are observed, e.g. small gaps and deformations (mainly pentagons and heptagons). When DNA

concentration is lower than 100 nM, surface coverage decreases as DNA concentration decreases though 2D arrays could be observed at low as 5 nM DNA. This result suggests that overall solution DNA concentration influences the DNA concentration near the surface; in contrast, [Ni^{2+}] affects DNA-surface interaction.
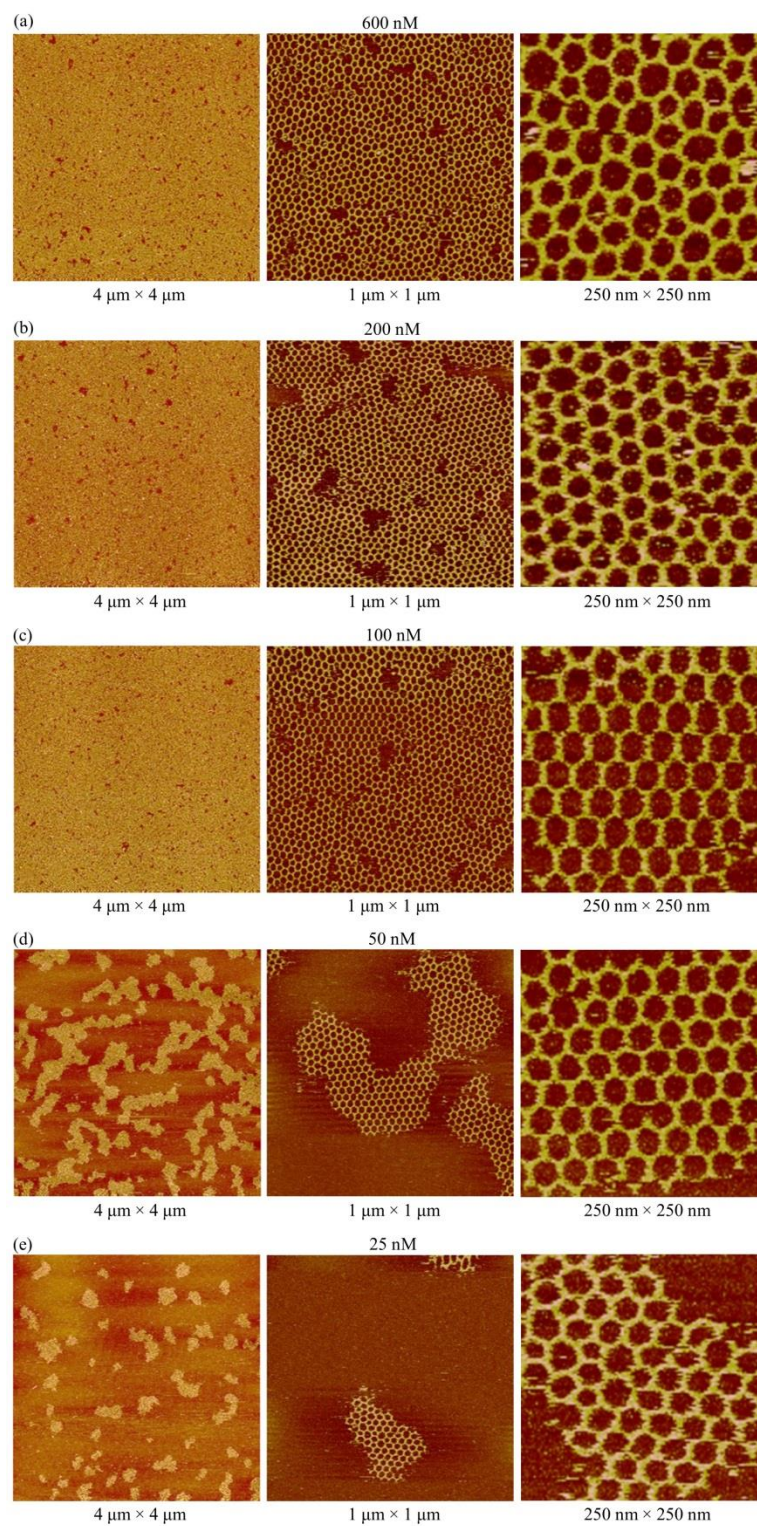
Figure 2.6. Effect of DNA concentration on 2D assembly of blunt-ended 3-point-star motif on mica as studied by AFM imaging. DNA concentrations are indicated on the figures. Experiment condition: in TAE/Mg^{2+} – 4 mM Ni^{2+}, assembly: 3 minutes at 25 °C.

(3) Assembly duration. We have also explored the assembly kinetics by varying the assembly duration in the range of 5 seconds to 10 minutes. As shown in Figure 2.7, in 5 seconds, 2D arrays start to form though the surface coverage is low. When assembly duration increases to 3 minutes, high coverage of 2D arrays is observed. These results reveal that the 2D assembly on surface via base stacking is a fast process when compared with previously reported 2D assembly dictated by sticky-end cohesion (often >12 hours).
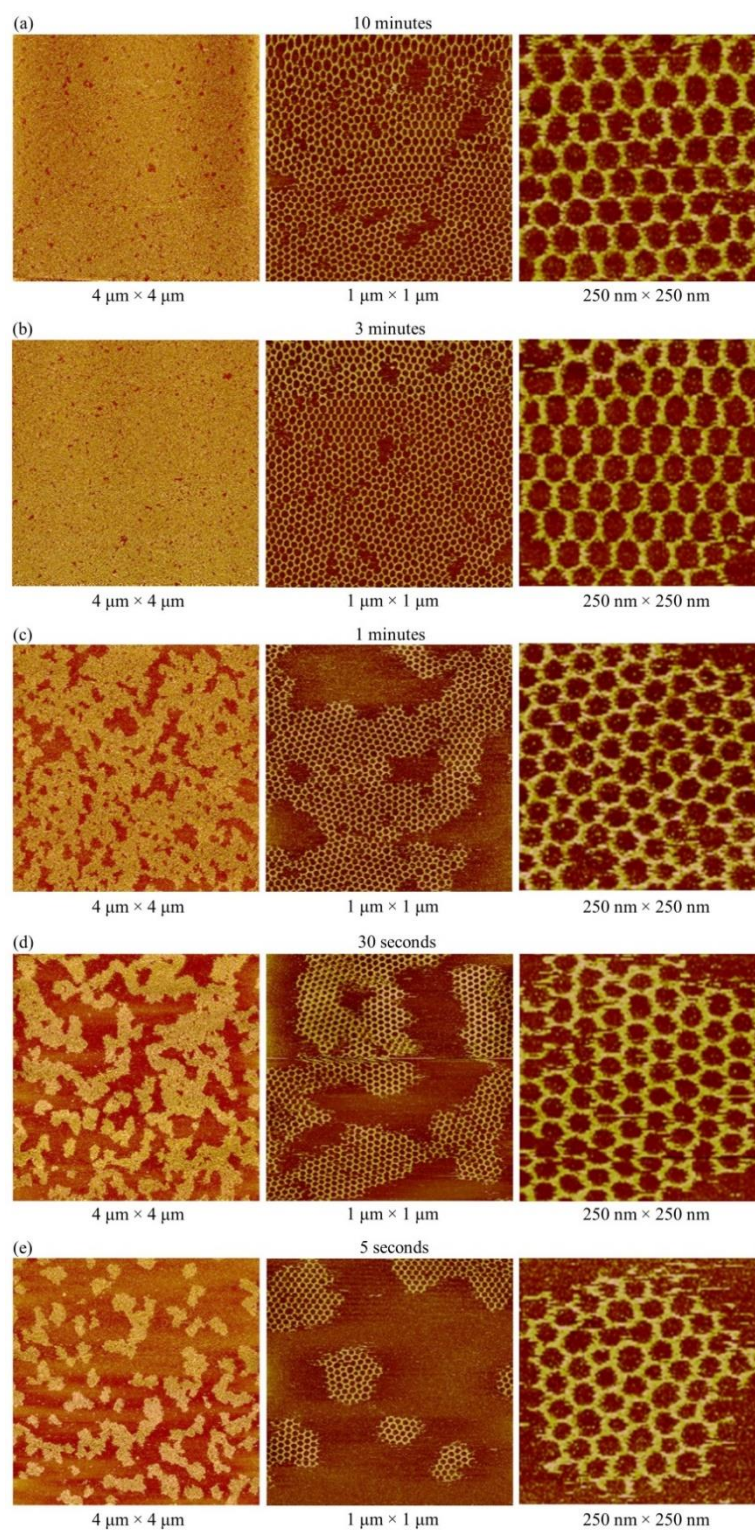
Figure 2.7. Effect of assembly duration on 2D assembly of blunt-ended 3-point-star motif on mica as studied by AFM imaging. Assembly durations are indicated on the figures. Experiment condition: in TAE/Mg^{2+} – 4 mM Ni^{2+}, 100 nM DNA 3-point-star motif.

2.4.2 4-Point-Star Motifs

When we extend our study to another similar, branched, DNA motif, 4-point-star motif,[43] an interesting phenomenon has been observed. This motif has been shown that it can assemble into tetragonal 2D arrays via sticky-end cohesion in solution.[43] However, when being subjected to the base stacking-driven surface assembly, it behaves dramatically differently. Not only tetragonal 2D arrays are observed, but trihexagonal and rhombic arrays also exist (Figure 2.8). Furthermore, by rationally varying the experimental conditions, we can partially control the distribution of these conformations.
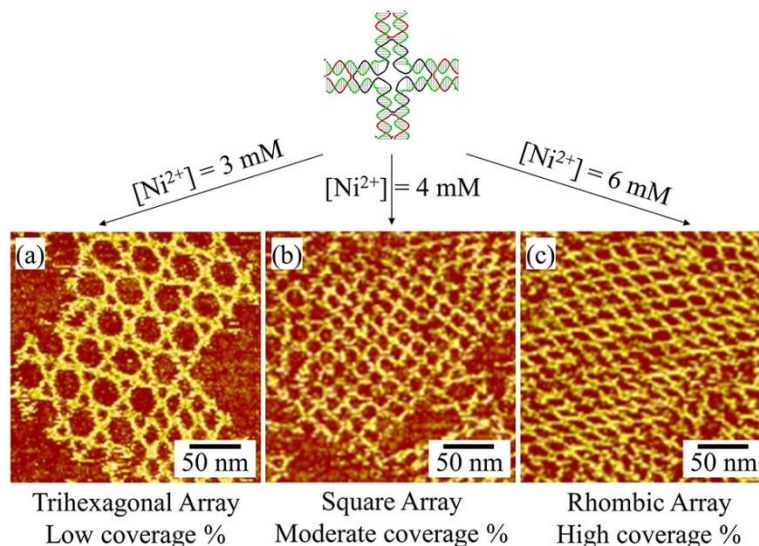
Figure 2.8. Three different 2D arrays assembled from 4-point-star motif under different Ni^{2+} concentration. (Experimental condition: 200 nM DNA in TAE/Mg^{2+} – Ni^{2+} buffer, 5 min incubation).

The primary controlling factor is the Ni^{2+} concentration (Figure 2.9). At 2 mM Ni^{2+}, no array is detected due to Ni^{2+}-EDTA chelation. When [Ni^{2+}] is increased to 3mM, DNA 2D arrays covers ~ 50% of mica surface and trihexagonal arrays dominate. With 4 mM Ni^{2+}, square arrays become dominating. With 6 mM Ni^{2+}, surface coverage reaches about 100% and dominating arrays

change from trihexagonal arrays and square arrays, to squeezed rhombic arrays. When $[Ni^{2+}]$ is higher than 7 mM, the surface becomes too densely packed and the DNA structures cannot maintain their intrinsic shapes (Figure 2.9 f-h).
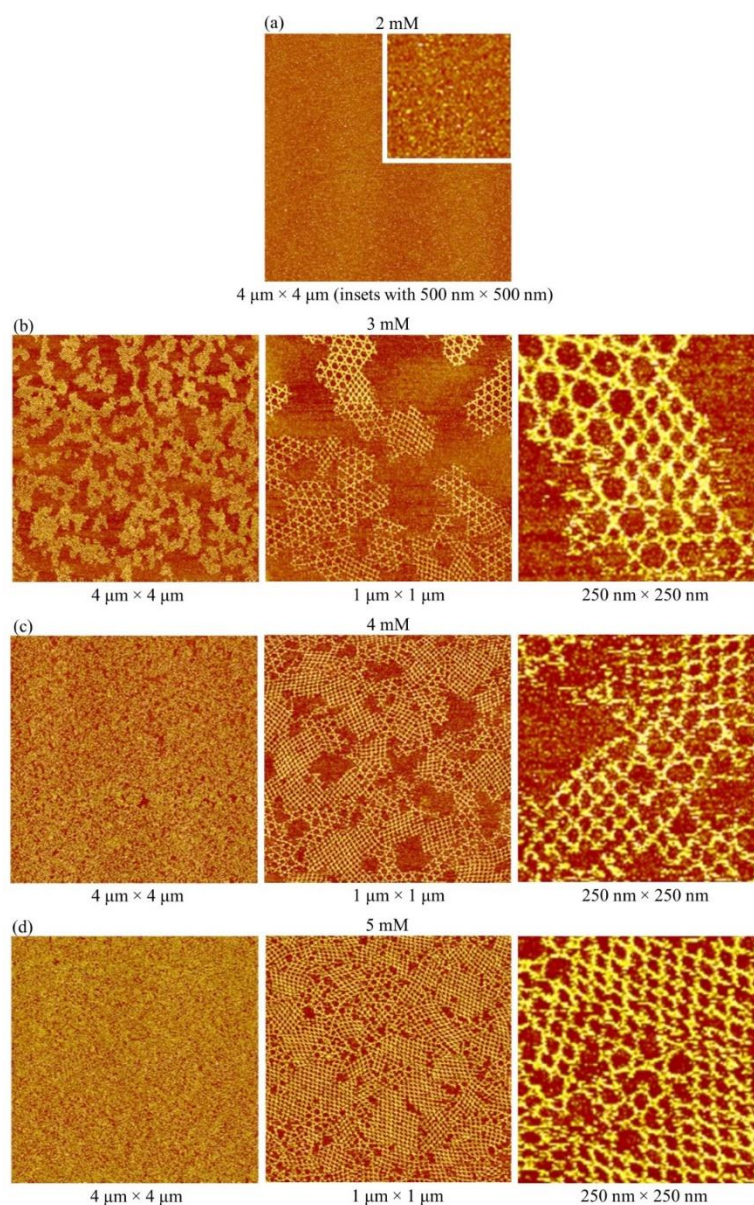
Figure 2.9. Effect of Ni^{2+} concentration on 2D assembly of blunt-ended 4-point-star motif on mica as studied by AFM imaging. Experiment condition: in TAE/Mg^{2+} buffer plus indicated Ni^{2+} concentration, assembly: 5 minutes at 25 °C, 200 nM DNA 4-point-star motif.

Figure 2.9 continued

(e) 6 mM

4 μm × 4 μm   1 μm × 1 μm   250 nm × 250 nm

(f) 7 mM

4 μm × 4 μm   1 μm × 1 μm   250 nm × 250 nm

(g) 8 mM

4 μm × 4 μm   1 μm × 1 μm   250 nm × 250 nm

(h) 10 mM

4 μm × 4 μm   1 μm × 1 μm   250 nm × 250 nm
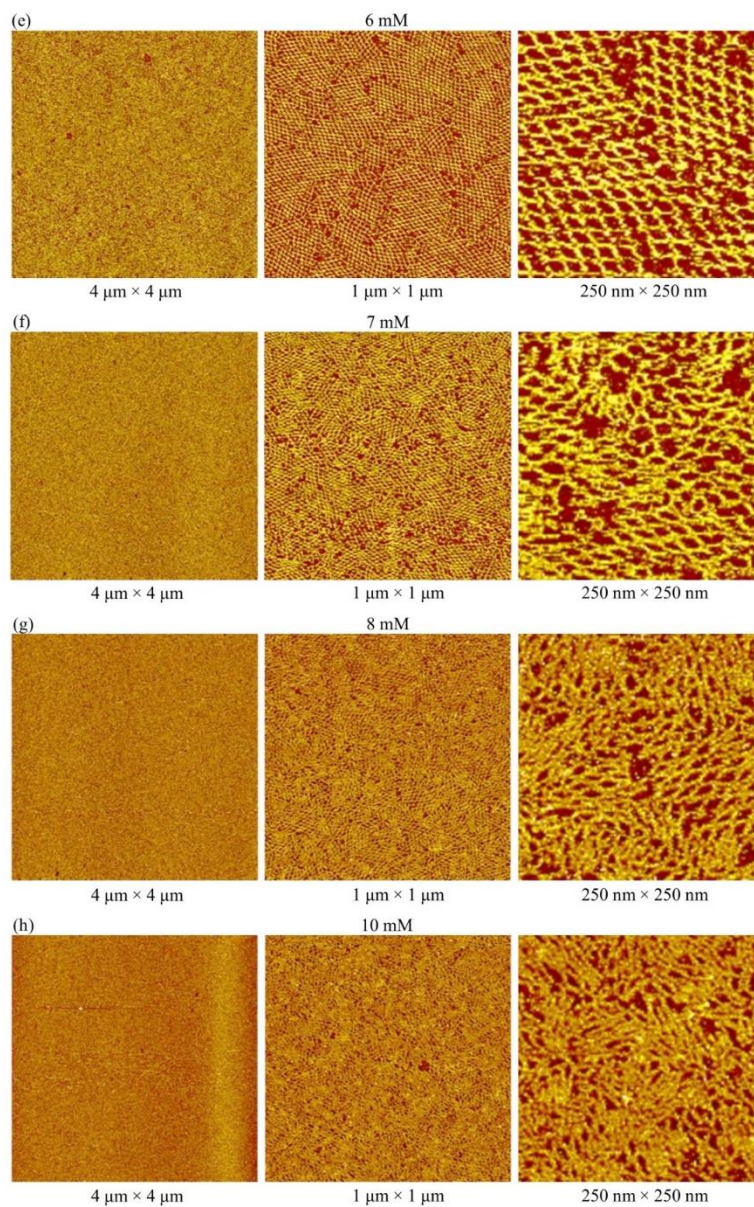
To understand the change of the array structure along the change of [Ni^{2+}], we have performed a statistical analysis on the DNA 2D arrays in the [Ni^{2+}] range of 3 – 6 mM (Figure 2.10). From trihexagonal arrays to tetragonal arrays to rhombic arrays, the DNA packing density increases, and the area occupied by each 4-point-star motif decreases. Our statistic data show that a linear relationship exists between the surface coverage and the percent of the DNA motif in

tetragonal conformation. At a low [Ni^{2+}], surface coverage of DNA is low. Each motif can occupy a large surface area so that the DNA arrays tend to adopt a low packing density conformation, trihexagonal arrays. At a high [Ni^{2+}], surface coverage of DNA is high. Each motif can only occupy a small surface area so that the DNA arrays tend to adopt a high packing density conformation, rhombic arrays.
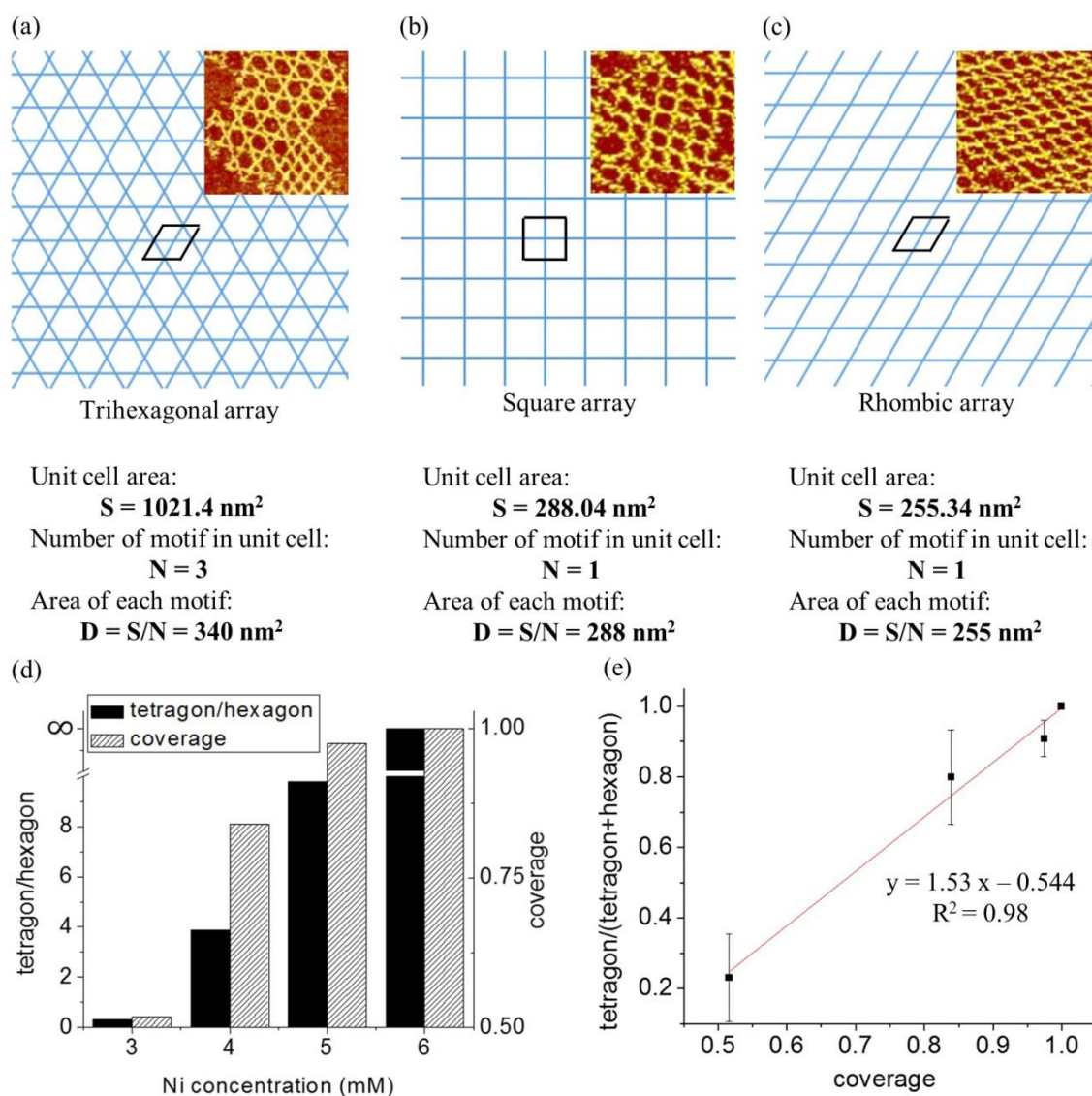
Figure 2.10. Statistical analysis of [Ni^{2+}]'s effect on 2D assembly of blunt-ended 4-point-star motif on mica as studied by AFM imaging.

2.4.3 DNA duplex

An important question in this approach is: what is the minimal number of base-stacking pairs of blunt ends that are needed to stably associate two building blocks together? Here we have examined the smallest possible number (one) of pairs of blunt ends. A 24-base pair (bp)-long, blunt-ended DNA duplex is used. The interaction between any two component DNA molecules is only base stacking between one pair of blunt ends. Under AFM imaging, some long chains have been observed. They are 1D chains assembled from the DNA duplexes and can be up to 250 nm long, corresponding to ~ 30 duplex molecules associated together (Figure 2.11). Such assembly also critically depends on both the bulk DNA concentration and Ni^{2+} concentration (Figure 2.12 and 2.13). When $[Ni^{2+}]$ is lower than 8 mM, no appreciable 1D chain is observed presumably because the small 24-bp-long DNA duplex could not adsorb onto the mica surface. When $[Ni^{2+}]$ is in the range of 8 – 10 mM, 1D DNA chains form. When $[Ni^{2+}]$ is higher than 12 mM, surface was so densely covered that no chain structure could be distinguished. This result shows that base stacking of only one pair of blunt-ends is strong enough to associate DNA building blocks together on surface.
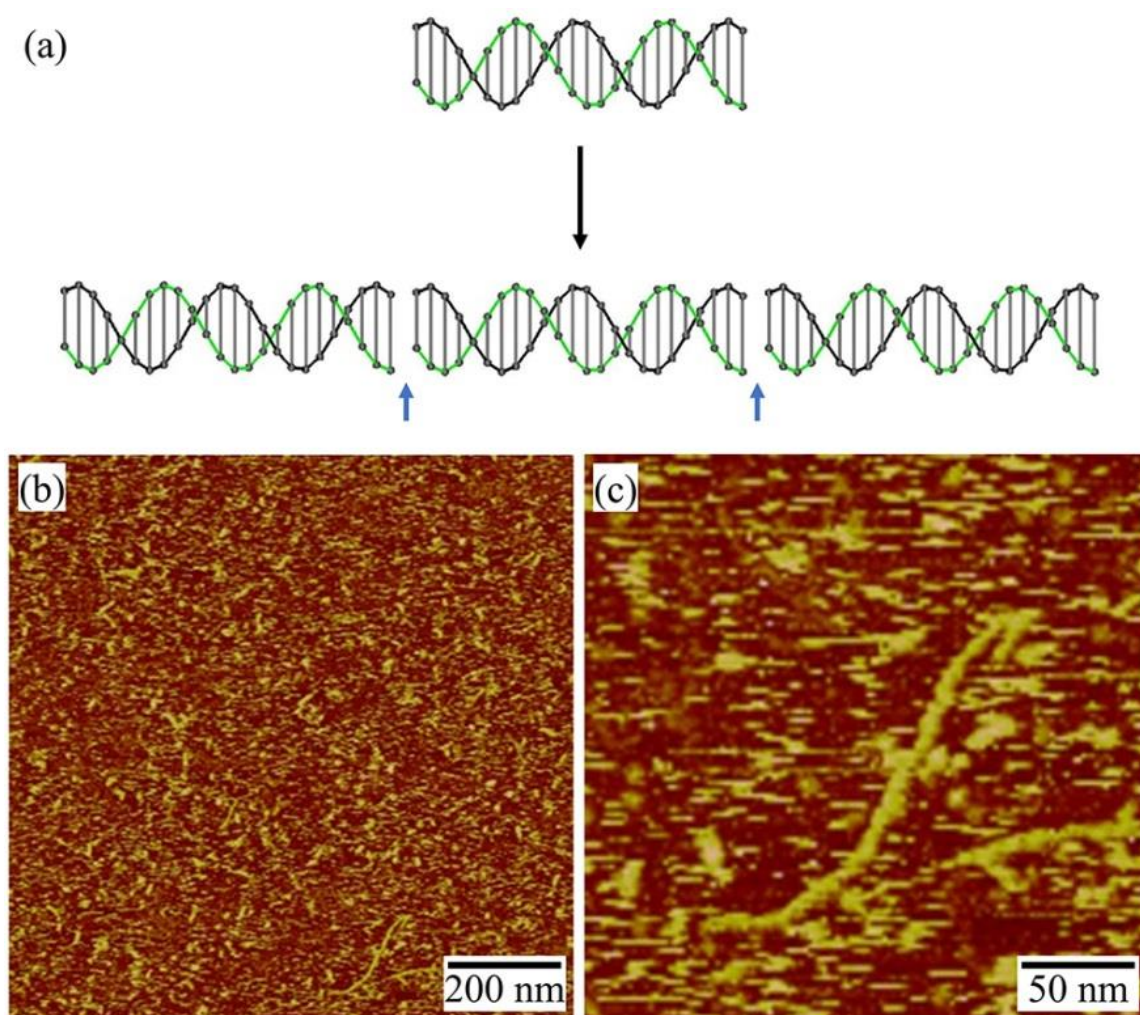
Figure 2.11. Short blunt-ended DNA duplexes assemble into long chains on surface. (a) Scheme. Blue arrows point blunt-end stacking sites. (b) and (c) A pair of atomic force microscopy (AFM) images of the DNA chains at different magnifications. (Experimental condition: 500 nM DNA in TAE/Mg^{2+} – 10 mM Ni^{2+} buffer, 5 min incubation).

(a) 7.5 µM (b) 5 µM (c) 3 µM

4 µm × 4 µm (insets: 500 nm × 500 nm)

(d) 1 µM

4 µm × 4 µm 1 µm × 1 µm 250 nm × 250 nm

(e) 0.5 µM

4 µm × 4 µm 1 µm × 1 µm 250 nm × 250 nm
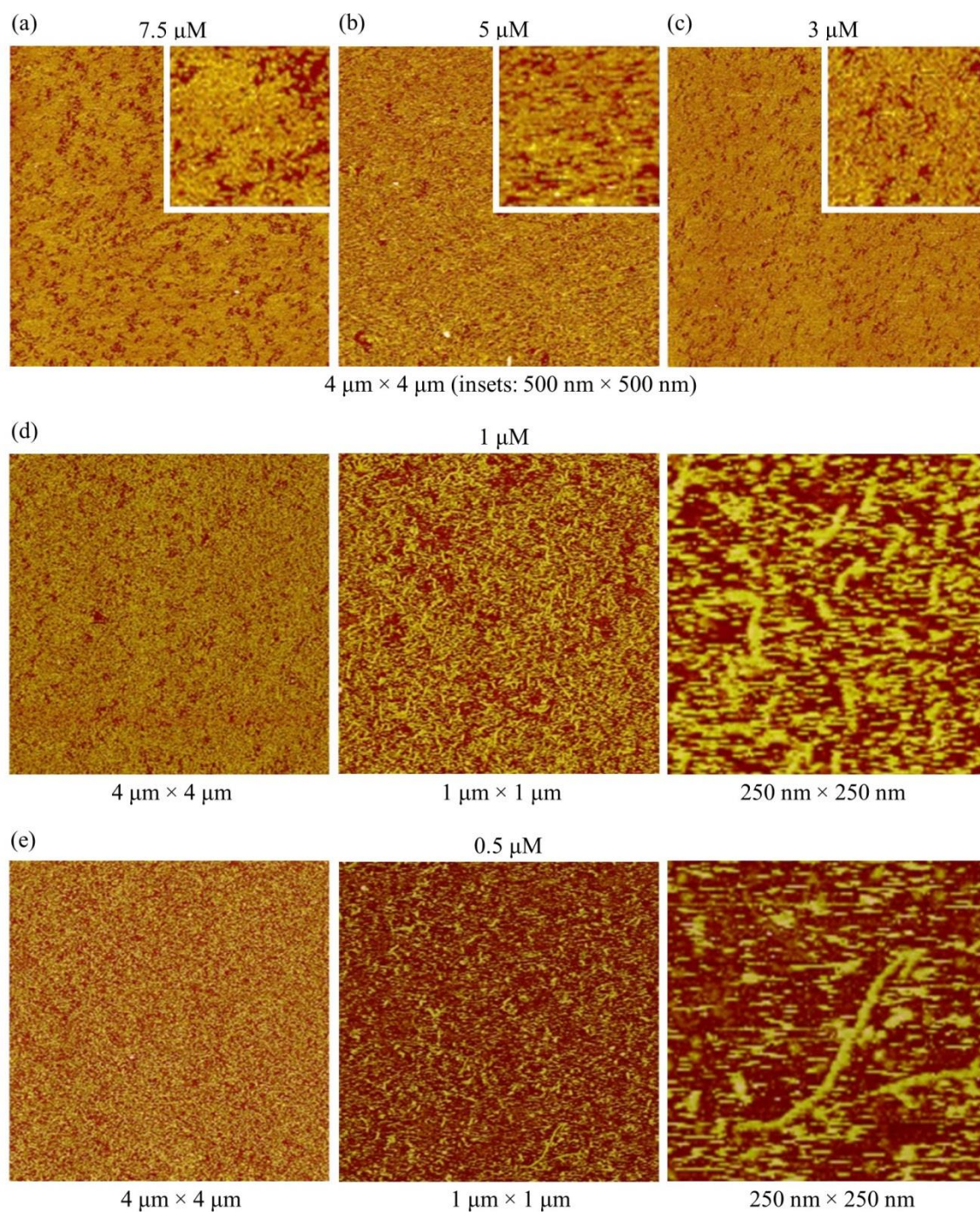
Figure 2.12. Effect of DNA concentration on 1D assembly of blunt-ended DNA duplexes on mica as studied by AFM imaging. DNA concentrations are indicated on the figures. Experiment condition: in TAE/Mg^{2+} – 10 mM Ni^{2+}.
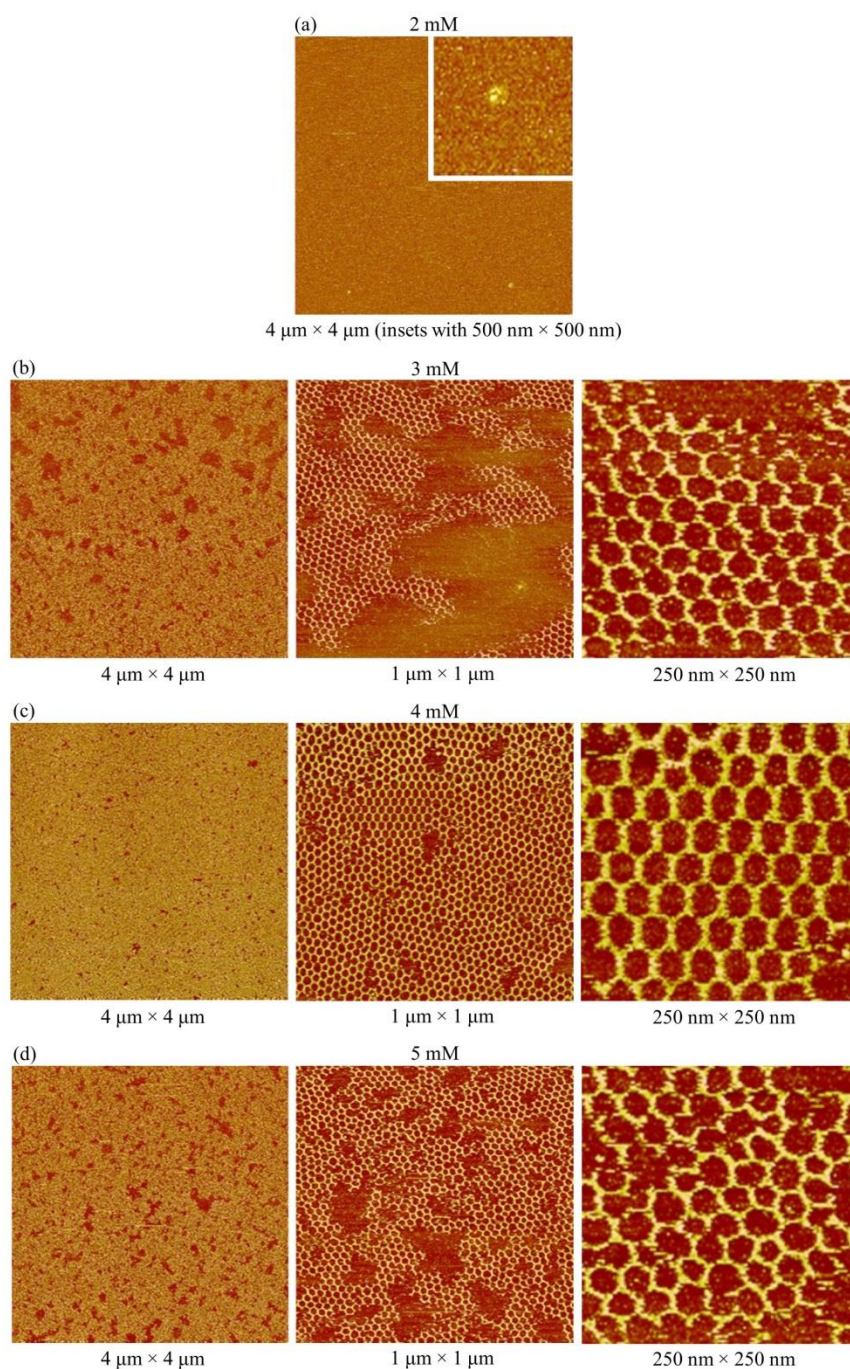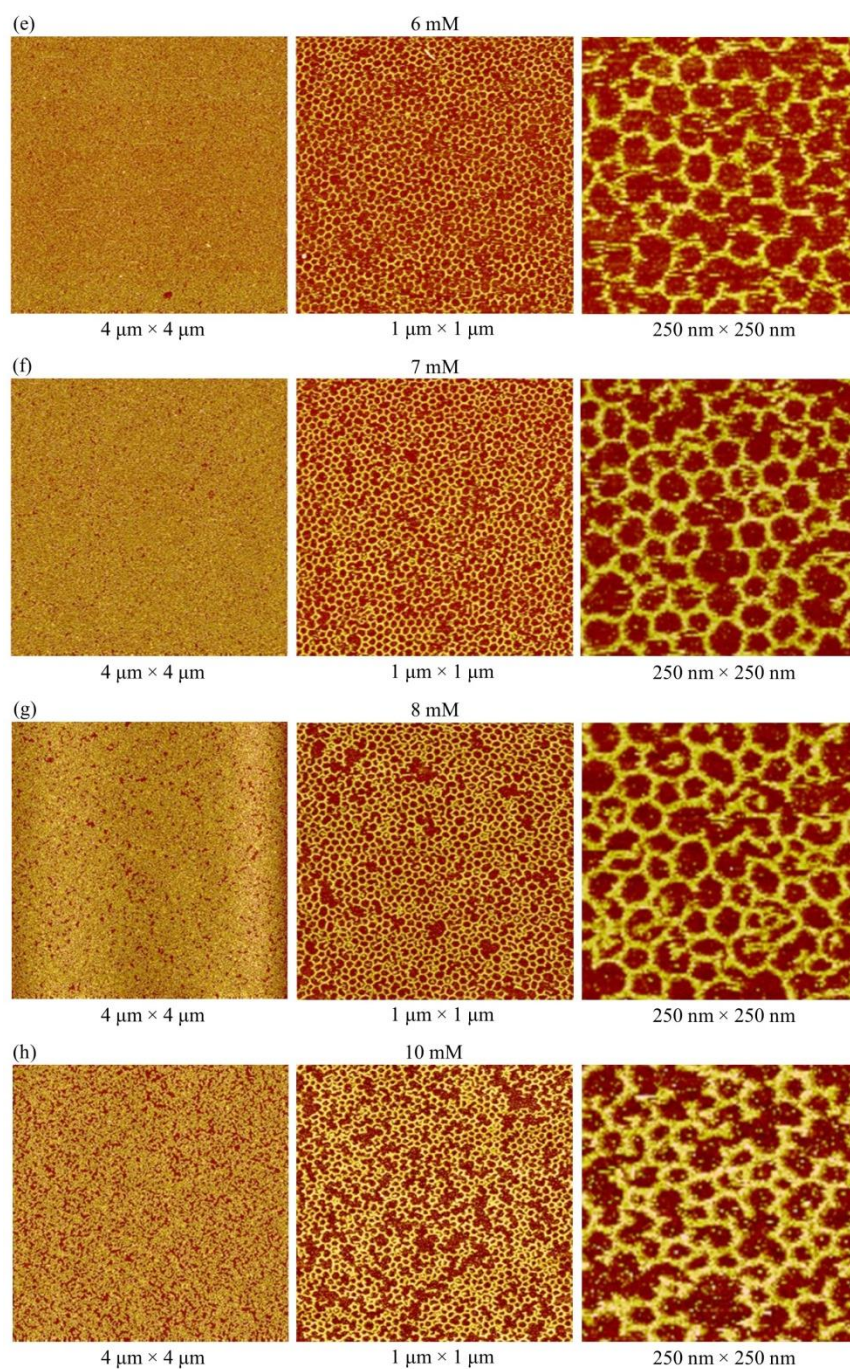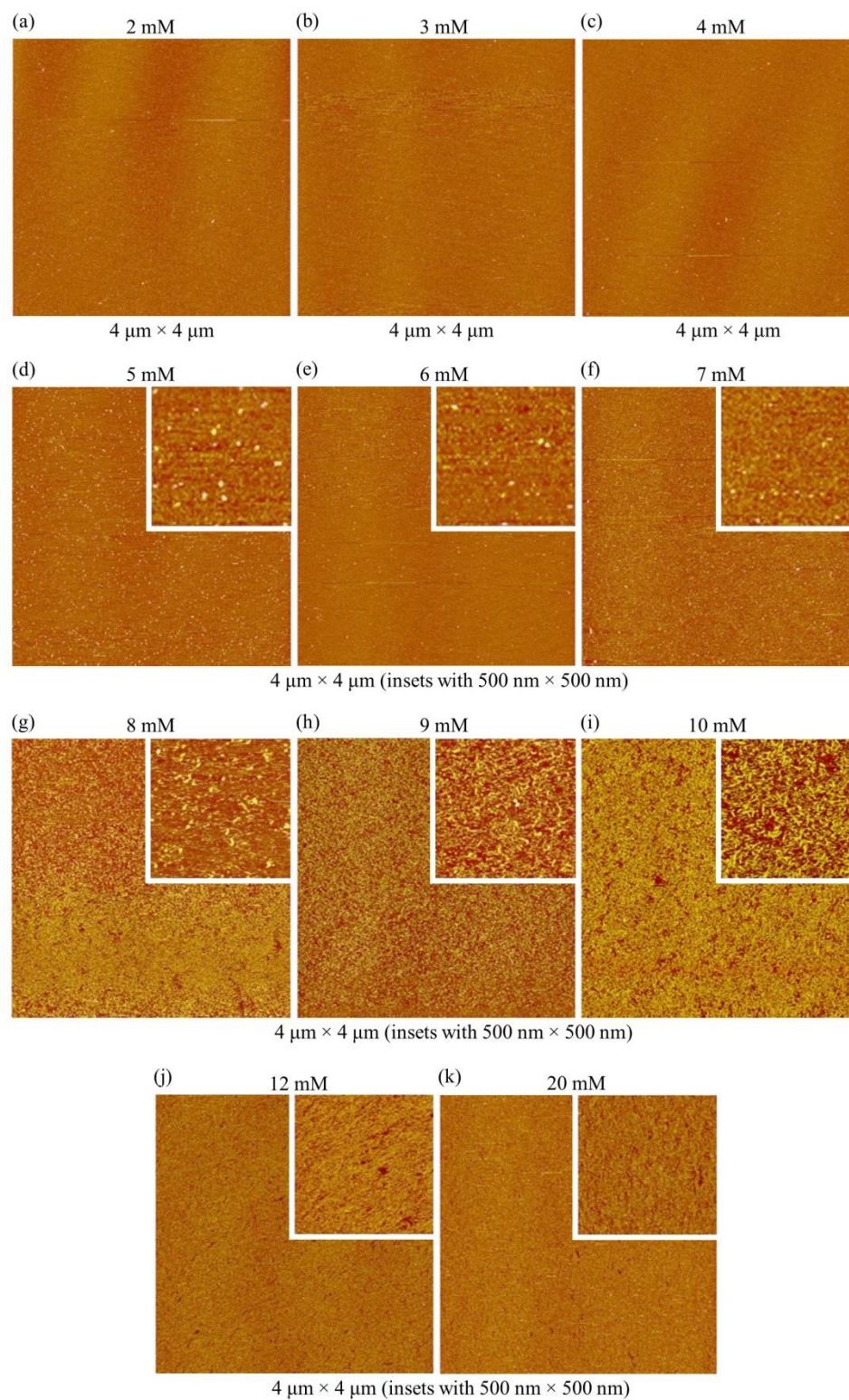
Figure 2.13. Effect of Ni²⁺ concentration on 1D assembly of blunt-ended DNA duplexes on mica as studied by AFM imaging. Experiment condition: 1 µM DNA duplexes with TAE/Mg²⁺ buffer plus indicated Ni²⁺ concentration.

2.4.4 Steric Effect – Double 6-Arm Junction Motifs

An interesting phenomenon, regulating DNA assembly via a steric effect, has been found when we study the assembly of a double 6-arm junction (D6aJ) motif.[83] It dramatically changes its final assembly patterns by a small structure change (Figure 2.14). A D6aJ motif contains four blunt ends and two short hairpins. Blunts ends can involve base stacking, leading to large structure formation. The two hairpins do not involve in inter-motif interaction, however, can regulate the assembly by steric effect. When the hairpins are short, any two D6aJ motifs can stack onto each other with two pairs of blunt ends, leading to formation of 1D D6aJ arrays (Figure 2.14a). When the hairpins are long, two D6aJ motifs can stack onto each other with one pair instead of two pairs of blunt ends because of the steric hindrance imposed by the long hairpins, leading to 2D array formation (Figure 2.14b).
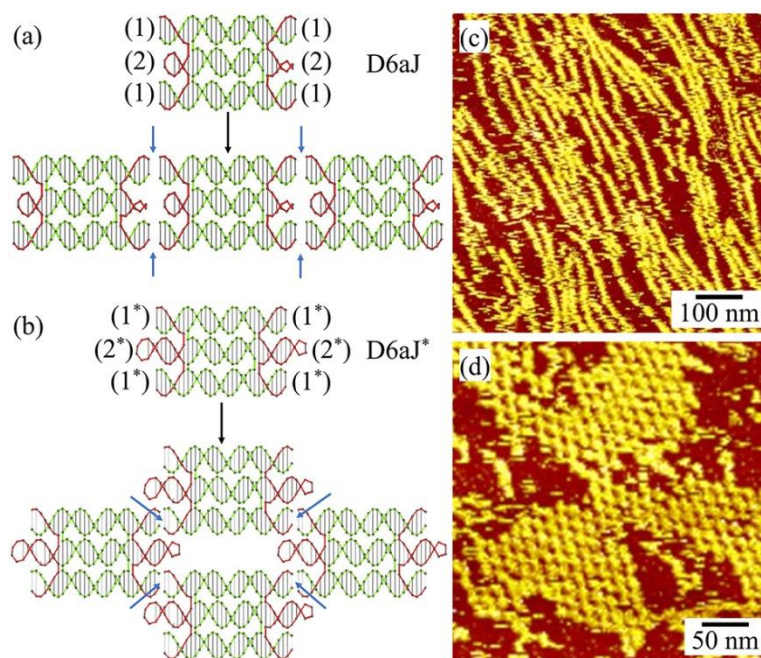
Figure 2.14. Sterically controlled DNA self-assembly of DNA double 6-arm junction (D6aJ) motif. (a) and (c) With short hairpins. (b) and (d) With long middle hairpins. In each panel, left shows scheme and right is the AFM image. (Experimental condition: 200 nM DNA in TAE/Mg^{2+} – Ni^{2+} buffer, 5 min incubation. for D6aJ, 6 mM Ni^{2+}; for D6aJ*: 7 mM Ni^{2+}.)

2.5   Conclusion

In summary, this study provides a new strategy to weak force-driven, DNA self-assembly by introduce an orthogonal interaction, DNA-surface interactions. It allows us to regulate DNA self-assembly via tuning the DNA-surface interaction. It is related to other studies, such as blunt-end stacking driven assembly and surface assembly. However, this study shows that we can regulate DNA-DNA interactions via weak interaction (base stacking between 1 or 2 pairs of blunt ends) by DNA-surface interaction. Long structures arise from assembly of short DNA duplexes as observed in this study might be relevant to prebiotic development of life. In addition, this study also demonstrates that large, complex DNA arrays can be assembled isothermally and quickly (~5 seconds), which is a very desirable when concerning introducing heat-sensitive guests, such as proteins. In addition, the resulting structures could potentially be useful for high-resolution molecular lithography.[84-86]

CHAPTER 3.   PATTERNING NANOPARTICLES WITH DNA MOLDS

3.1   Introduction

DNA is a promising material to construct programmable nanostructures with excellent precision and shape control. Recently, we reported a method to fabricate DNA 2D arrays on solid surfaces from blunt-ended DNA motifs.[77] This method provides large, continuous, and monocrystalline DNA templates. Ordered Nanoparticle (NP) arrays have many applications in physics, biosensing, etc. For example, AuNP arrays can serve as substrates for surface-enhanced Raman spectroscopy (SERS) detections.[87] Protein patterning is promising in studying biosensor systems and expanding knowledge in protein-protein and protein-cell interactions.[88-90] How can we use our developed DNA arrays as templates to pattern NPs? How can we regulate the patterning density? These problems will be solved in this chapter.

3.2   Scheme and Design

Figure 3.1 illustrates the process of patterning NPs by DNA 2D arrays. It is exemplified by a DNA tetragonal arrays from bridged 4-point-star (b4PS) motifs (Figure 3.2 a). Bridges are introduced to enhance the motif rigidity because unbridged 4-point-star motif could easily adapt different conformations.[77] Another type of DNA array is hexagonal array assembled from rhombus motif (Figure 3.2 b).[91] Between any two motifs, two pairs of blunt-end stacking will offer adequate interaction to associate motifs. The assembly of DNA motifs on surface results in 2D arrays (Figure 3.1 b and c). Then we modify the surface with positively-charged "glues" (Figure 3.1 d). These "glues" can be Ni^{2+} for DNA motifs and proteins patterning or PLL for AuNPs patterning. In the

last step, NPs are trapped by "glues" and patterned by DNA arrays (Figure 3.1 e). All DNA motifs

used in this study are shown in Figure 3.2.
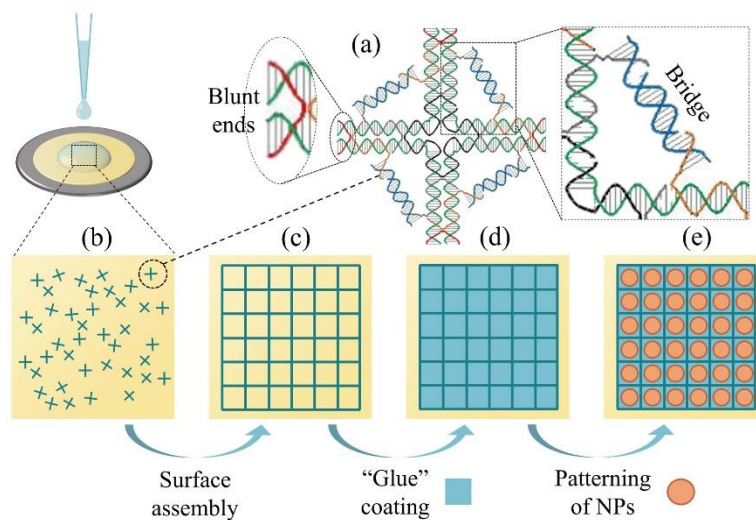
Figure 3.1. Process of nanoparticles (NPs) patterning directed by DNA arrays. (a) Molecular design of bridged 4-point-star (b4PS) motifs. (b) When DNA solution (light blue) contacts a mica surface (yellow), b4PS motifs (blue) will randomly adsorb onto mica surface. (c) Driven by base stacking between blunt ends, b4PS motifs rearrange themselves on the solid surface into 2D arrays. (d) The mica surface is then coated by "glues", which are positively charged materials (poly-L-lysine or Ni^{2+}). They are used to trap negatively-charged NPs. (e) Patterning NPs (red) by DNA arrays.
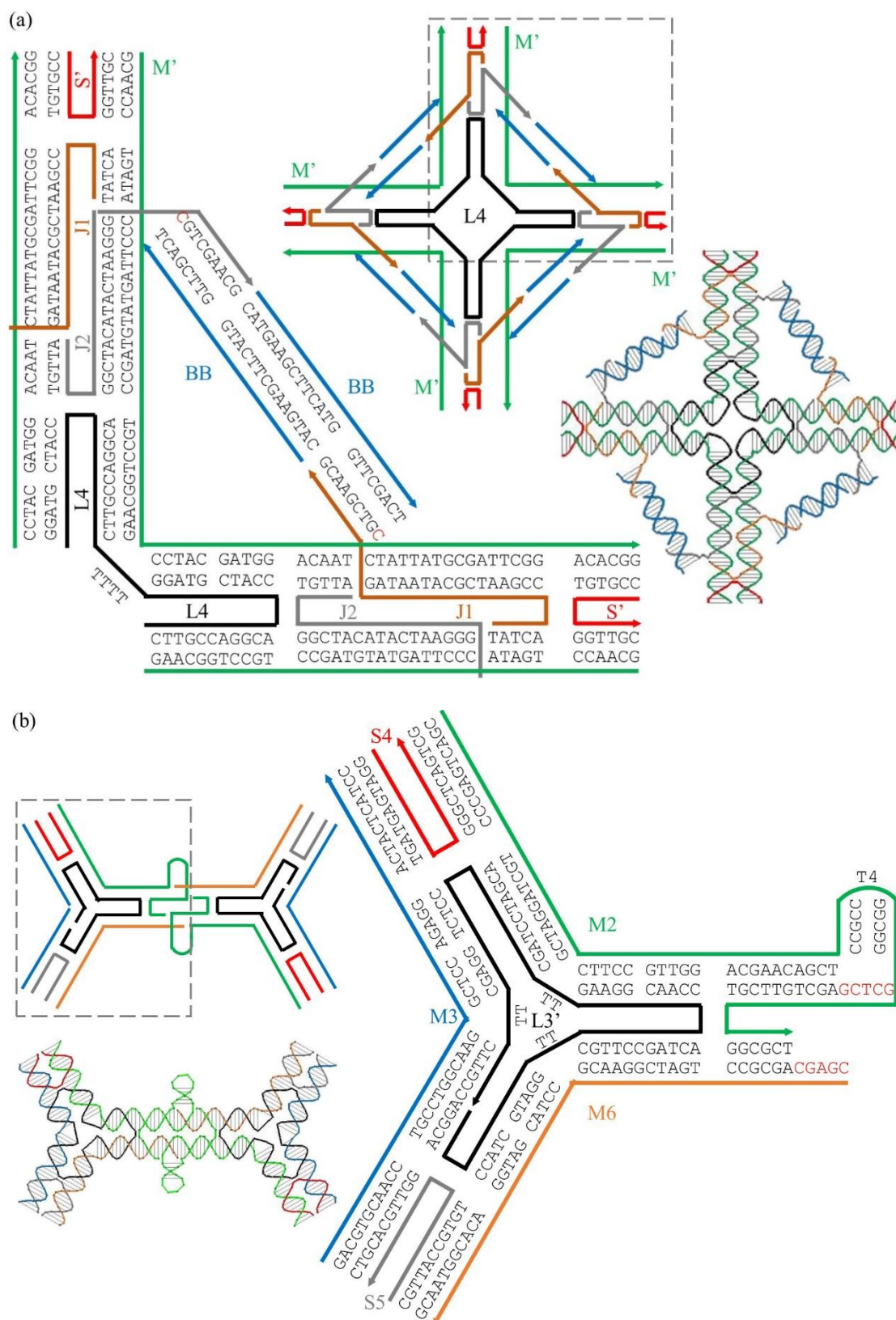
Figure 3.2. Scheme of DNA motifs with sequences.

Figure 3.2 continued

(c)

(d)

(e)
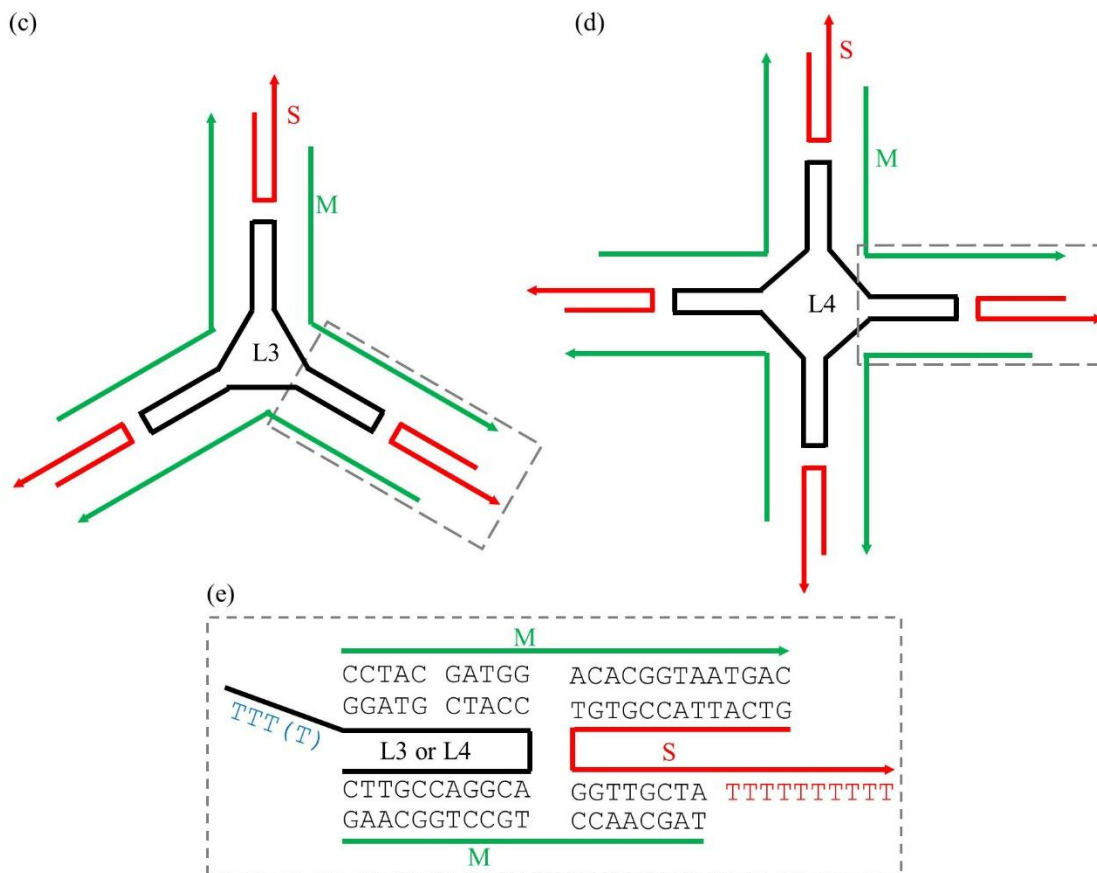
3.3   Materials and Methods

3.3.1   DNA Oligonucleotides

All oligonucleotides were purchased from IDT, Inc. and purified by 10% - 20% denaturing PAGE. Oligonucleotides from all motifs are listed below with their designated ratio and concentration during *in situ* assembly:

DNA Strands:

L4:   5'-AGGCACCATCGTAGGTTTTCTTGCCAGGCACCATCGTAGGTTTTCTTGC CAGGCACCATCGTAGGTTTTCTTGCCAGGCACCATCGTAGGTTTTCTTGCC-3'

M':   5'-GCAACCTGATACCCTTAGTATGTAGCCTGCCTGGCAAGCCTACGATGGA

CAATCTATTATGCGATTCGGACACGG-3'

J1:   5'-TATCACCGAATCGCATAATAGCGTCGAACG-3'

J2:   5'-ATTGTGGCTACATACTAAGGGCGTCGAACG-3'

S':   5'-CCGTGTGGTTGC-3'

BB: 5'-CATGAAGCTTCATGGTTCGACT-3'

L3':   5'-AGGCACCATCGTAGGTTCGTTCCGATCACCAACGGAAGTTCGATCCTAG

CACCTCTGGAGCTTCTTGCC-3'

M2:   5'-CGACTGAGCCCTGCTAGGATCGCTTCCGTTGGACGAACAGCTCCGCCTT

TTGGCGGGCTCGAGCTGTTCGTGGCGCT-3'

M3:   5'-GACGTGCAACCTGCCTGGCAAGGCTCCAGAGGACTACTCATCC-3'

S4:   5'-GGATGAGTAGTGGGCTCAGTCG-3'

S5:   5'-CGTTACCGTGTGGTTGCACGTC-3'

M6:   5'-CGAGCAGCGCCTGATCGGAACGCCTACGATGGACACGGTAACG-3'

L3:   5'-AGGCACCATCGTAGGTTTCTTGCCAGGCACCATCGTAGGTTTCTTGCCA

GGCACCATCGTAGGTTTCTTGCC-3'

M: 5'-TAGCAACCTGCCTGGCAAGCCTACGATGGACACGGTAATGAC-3'

S: 5'-GTCATTACCGTGTGGTTGCTATTTTTTTTTT-3'

T: 5'-thiol-TAACCGTGTGGAAGATAGTATG-3'

DNA Motifs:

b4PS: **L4**+**M**+**J1**+**J2**+**S**+**BB** (1:4:4:4:4:8). Motif concentration is 400 nM.

rhombus: **L3'**+**M2**+**M3**+**S4**+**S5**+**M6** (1:1:1:1:1:1). Motif concentration is 500 nM.

3PS: **L3**+**M**+**S** (1:3:3). Motif concentration is 1 μM.

4PS: **L4**+**M**+**S** (1:4:4). Motif concentration is 1 μM.

3.3.2 Buffers

TAE buffer: 40 mM tris base, 20 mM acetic acid, and 2 mM EDTA; pH is adjusted to 8.0;

TAE/Mg^{2+} buffer: 40 mM tris base, 20 mM acetic acid, 2 mM EDTA, and 12.5 mM magnesium acetate; pH is adjusted to 8.0;

TA buffer: 40 mM tris base, and 20 mM acetic acid; pH is adjusted to 8.0;

TA/Mg^{2+} buffer: 40 mM tris base, 20 mM acetic acid, and 10 mM magnesium acetate; pH is adjusted to 8.0;

TA/Na/$\underline{x}$ mM Mg^{2+} buffer: 40 mM tris base, 20 mM acetic acid, designated $\underline{x}$ mM magnesium acetate, and 500 mM sodium chloride; pH is adjusted to 8.0;

TA/Mg^{2+}/Ni^{2+} buffer: 40 mM tris base, 20 mM acetic acid, 10 mM magnesium acetate, and 2 mM nickel chloride; pH is adjusted to 8.0.

3.3.3 Preparation of Individual DNA Motifs

(1) For b4PS motif, mix all single-stranded DNAs (except bridge strands BB) at designated stoichiometric molar ratio in TA/Mg^{2+} solution [final 40 μL 500 nM motif solution (no bridges)]. Sequentially incubate above solutions: 95 °C for 5 min, 65 °C for 30 min, 50 °C for 30 min, 37 °C for 30 min, and 22 °C for 30 min. Then add 10 uL of bridge DNA, BB, into the annealed solution above and incubate for 1 hour at 22 °C [final 50 uL 400 nM b4PS motif solution (with bridges)]. (2) For rhombus motif, mix all single-stranded DNAs at designated stoichiometric molar ratio in TA/Mg^{2+} solution [final 40 μL 500 nM motif solution]. Sequentially incubate above solutions: 95 °C for 5 min, 65 °C for 30 min, 50 °C for 30 min, 37 °C for 30 min, and 22 °C for 30 min. (3) For 3PS and 4PS motif, mix all single-stranded DNAs at designated stoichiometric molar ratio in TA/Mg^{2+} solution [final 40 μL 1 μM motif solution]. Sequentially incubate above solutions: 95 °C for 5 min, 65 °C for 30 min, 50 °C for 30 min, 37 °C for 30 min, and 22 °C for 30 min.

3.3.4 Preparation of DNA-Conjugated AuNP Solution

AuNPs (diameter 5 and 10 nm) were purchased from BBI Solutions (EMGC5, and EMGC10). AuNPs were mixed with thiolated DNA (T) in TAE buffer at the molar ratio of 1:40 for 5 – nm AuNP or 1:160 for 10 – nm AuNP. NaCl concentration was gradually increased by steps of 0.1 M at 3 hours intervals to final concentration of 0.5 M. The formed AuNP-DNA conjugates were purified two times by centrifugation-redispersion process (Eppendorf Centrifuge 5415D) to remove excessive thiolated DNA. Centrifugation protocol is 16160 g for 1.5 hours for 5-nm AuNP or 9280 g for 1 hour for 10-nm AuNP. Re-dispersing buffer is TA buffer. DNA-conjugated AuNPs were finally re-dispersed in TA buffer at 4 µM for 5 – nm AuNP or 500 nM for 10 – nm AuNP. Their molar concentrations were determined by spectrometric absorption at 520 nm (LAMBDA 365 UV/Vis spectrophotometer, PerkinElmer, Inc.) with extinction coefficients of 1.10×10^7 and 1.01×10^8 $M^{-1} \cdot cm^{-1}$ for 5 – and 10 – nm AuNPs, respectively.

3.3.5 Native PAGE

4% or 6% polyacrylamide/bisacrylamide (19:1, 5% crosslinker) gels were run on a FB-VE10-1 electrophoresis unit (FisherBiotech) at 4 °C (300V, constant voltage) for approximately 2 hours with TAE/Mg^{2+} buffer as running buffer. After electrophoresis, the gels were stained with Stains-all dye (Sigma) and scanned.

3.3.6 Formation of DNA Arrays via Surface-Assisted Self-Assembly

(1) Preparation: Prepare a final 50 nM b4PS motif in TA/Na/10 mM Mg^{2+} solution or 100 nM rhombus motif in TA/Na/25 mM Mg^{2+} solution. (2) Surface assembly: Deposit 5 µL DNA solution onto a freshly cleaved mica surface and incubate for 24 hours at 22 °C for array formation. (3) Buffer wash: After surface assembly, 20 µL TA/Na/60 mM Mg^{2+} buffer is added onto mica

surface and then removed. Repeat this process for four times. (4) AFM image capture: 20 µL TA/Mg^{2+}/Ni^{2+} buffer is added onto mica surface. Then AFM images are captured in fluid. All experiments are carried out at 22 °C.

3.3.7 Formation of Ordered DNA Nanomotifs

(1) Preparation: Prepare 3PS or 4PS motif in TA/Mg^{2+}/Ni^{2+} solution at designated motif concentration (in the range of 20 – 75 nM). (2) Patterning: 5 µL DNA solution is deposited onto a mica surface with preformed DNA arrays, stands for 5 min, and then removed. (3) Buffer wash: After patterning, 20 µL TA/Mg^{2+}/Ni^{2+} buffer is added onto mica surface and then removed. (4) AFM image capture: 20 µL TA/Mg^{2+}/Ni^{2+} buffer is added onto mica surface. Then AFM images are captured in fluid. All experiments are carried out at 22 °C.

3.3.8 Formation of Ordered AuNPs

(1) Surface modification (PLL coating): Prepare PLL (0.1% w/v, molecular weight 150,000 – 300,000, Ted Pella, Inc.) in TA/Mg^{2+}/Ni^{2+} solution to give final 40 μg/mL PLL solution. 20 µL PLL solution is deposited onto a mica surface with preformed DNA arrays, incubated for 10 min, and then removed. Wash with 20 µL TA/Mg^{2+}/Ni^{2+} solution. (2) Patterning: 5 µL DNA-conjugated AuNP solution is added, incubated for 5 min, and then removed. (3) AFM image capture: AFM images are captured in air. All experiments are carried out at 22 °C.

3.3.9 Formation of Ordered Proteins

(1) Preparation: Prepare ovalbumin, or OVA (lyophilized powder, ≥ 98%, Sigma-Aldrich) or lysozyme, or LYZ (lyophilized powder, protein ≥ 90%, Sigma-Aldrich) in TA/Mg^{2+}/Ni^{2+} solution at designated protein concentration (in the range of 25 – 400 nM). (2) Patterning: 20 µL

protein solution is added and incubated for 5 min. (3) AFM image capture: AFM images are captured in fluid. All experiments are carried out at 22 °C.

3.3.10 Formation of DNA-Silica Hybrid Networks

(1) Preparation: 2% (v/v) of TMAPS (N-trimethoxysilylpropyl-N,N,N-trimethylammonium chloride, ca. 50% in methanol, Alfa Aesar) and 2% (v/v) TEOS (tetraethyl orthosilicate, Sigma-Aldrich) are slowly added into TA/Mg^{2+} buffer while vigorously stirring. After 30 min, transfer the solution into a glass petri dish. (2) Silica decoration: Mica surfaces with preformed DNA arrays are placed faced down and immersed in the solution. Incubate for designated time. (3) Surface washing: Remove the solution and wash with ethanol for three times and TA/Mg^{2+} buffer for twice. (4) AFM image capture: AFM images are captured in air. All experiments are carried out at 22 °C.

3.3.11 AFM images

(1) AFM images in fluid were captured by MultiMode 8 (Bruker) using ScanAsyst-fluid mode with ScanAsyst-fluid+ probes (Bruker). (2) AFM images in air were captured by MultiMode 8 (Bruker) using ScanAsyst-air mode with ScanAsyst-air probes (Bruker). The tip-surface interaction was automatically adjusted to optimize the scan set-point.

3.3.12 FFT and Inverse FFT Processing

Import the original AFM images into ImageJ software developed by the National Institutes of Health.[92] Use FFT operation to obtain FFT diffraction patterns then followed by brightness-and-contrast adjustment. Pick up the targeted intense diffraction spots and use inverse FFT operation to render reconstructed images.

3.4   Results and Discussion

3.4.1   Formation of DNA Arrays as Templates

DNA arrays were assembled in two steps according to our previous method.[77] (*i*) Assembly of individual DNA motifs in solution. All component strands were mixed at designated ratios in TA/Mg^{2+} buffer and the mixture solutions were thermal annealed. The formation of individual motifs was confirmed by native PAGE (Figure 3.3 and 3.4). One important design of b4PS motif is the introduction of bridges (blue-colored strand, BB), which can control the inter-branch angles and rigidity of DNA motif.
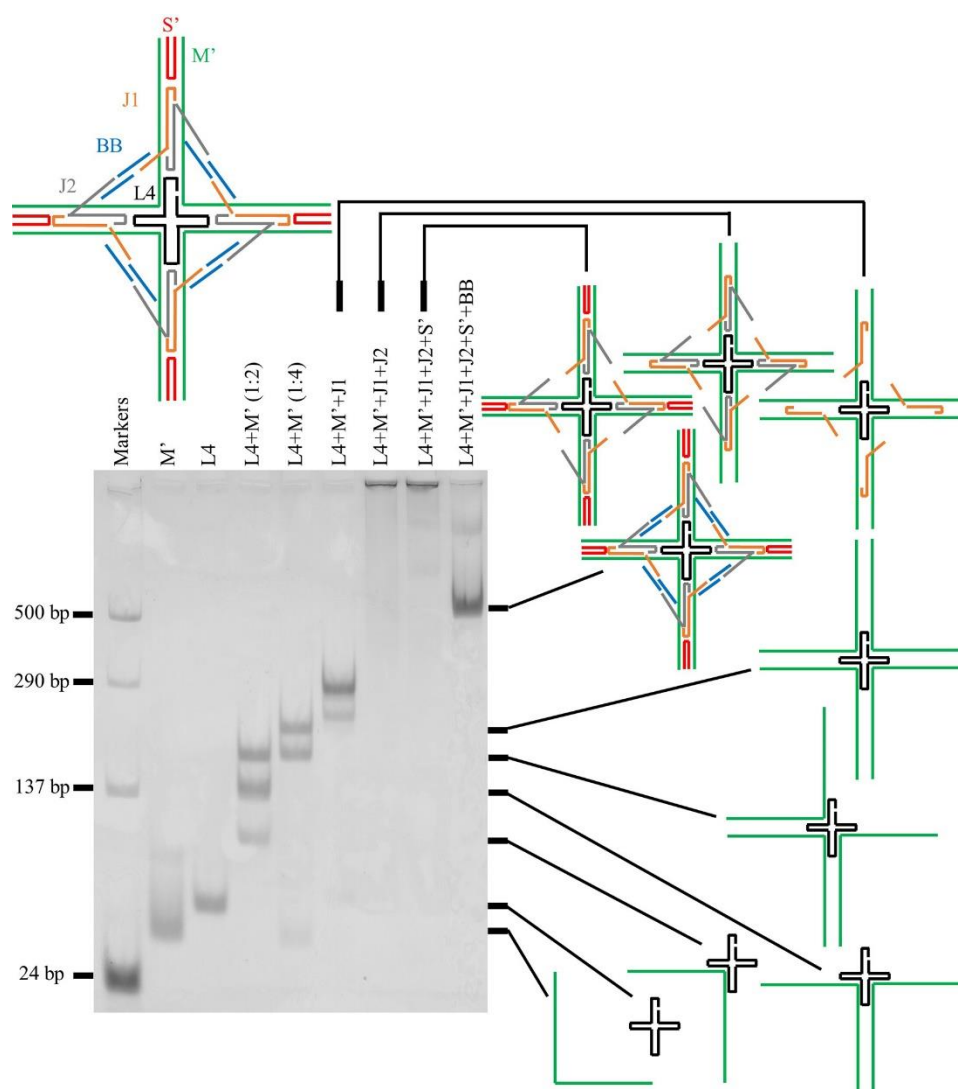
Figure 3.3. 4% native PAGE analysis of individual b4PS motif at 4 °C. After addition of bridges, the designed b4PS motif readily formed and appeared as a sharp, major band with an expected mobility.
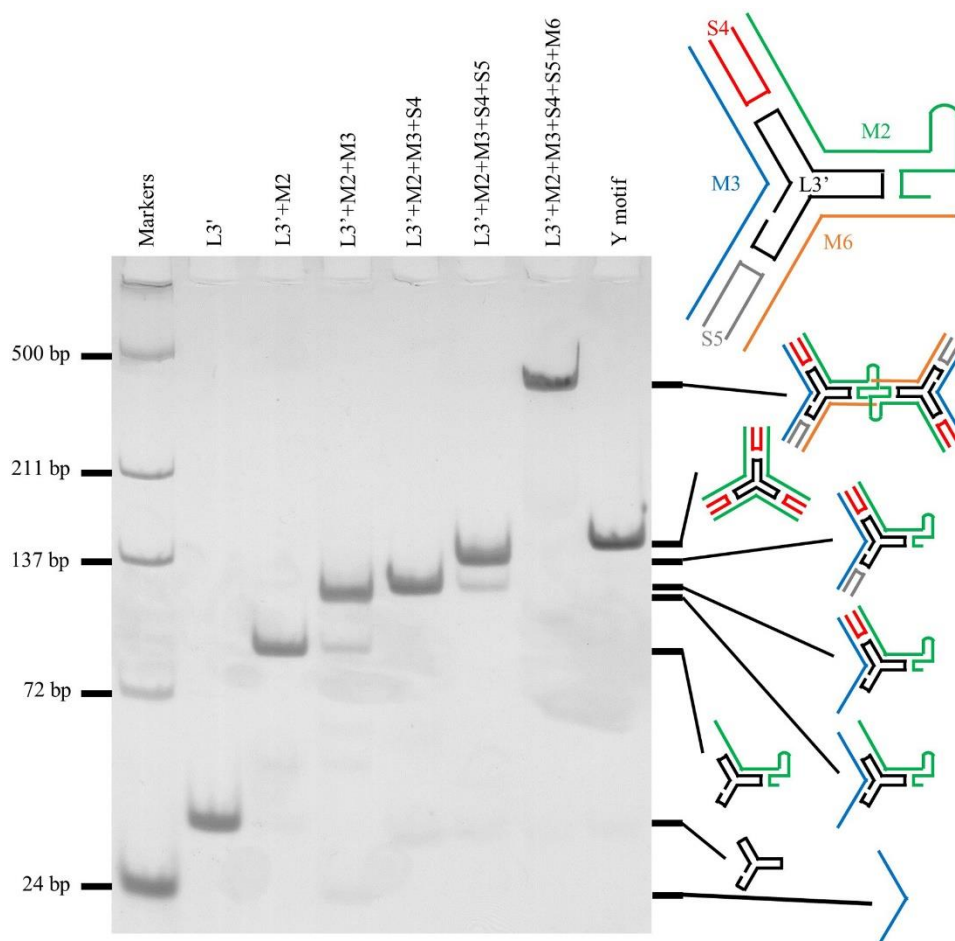
Figure 3.4. 6% native PAGE analysis of individual rhombus motif at 4 °C. After mixing all single-stranded DNAs, the designed rhombus motif readily formed and appeared as a sharp, major band with expected about twice the size as a blunt-ended three-point-star motif.

(*ii*) Surface-assisted self-assembly of DNA arrays from motifs. Pre-formed, individual DNA motifs were deposited onto a freshly cleaved mica surface. Isothermal incubation at 22 °C led to the assembly of large single-crystal arrays (Figure 3.1 b,c and Figure 3.5 b, e). One advantage of the surface-assisted self-assembly is that it allows readily optimizing integrity and global homogeneity of single-crystal arrays by tuning concentration of Mg^{2+}, $[Mg^{2+}]$. The strength of DNA-surface interaction positively correlates with $[Mg^{2+}]$. Too low $[Mg^{2+}]$ leads to insufficient DNA-surface interaction, resulting in small pieces of DNA arrays (Figure 3.5 a and d); too high $[Mg^{2+}]$ leads to too strong DNA-surface interaction, resulting in poly-crystals (Figure 3.5 c and f).

Only at proper [Mg^{2+}], DNA-surface interaction is moderate and large-scale arrays can form with global homogeneity. The arrays are over 4 μm × 4 μm in area and contain more than 20,000 and 34,000 wells for tetragonal and hexagonal arrays, respectively, as observed by AFM (Figure 3.5 b and e). Global homogeneity is important for formation of uniform NP lattices.
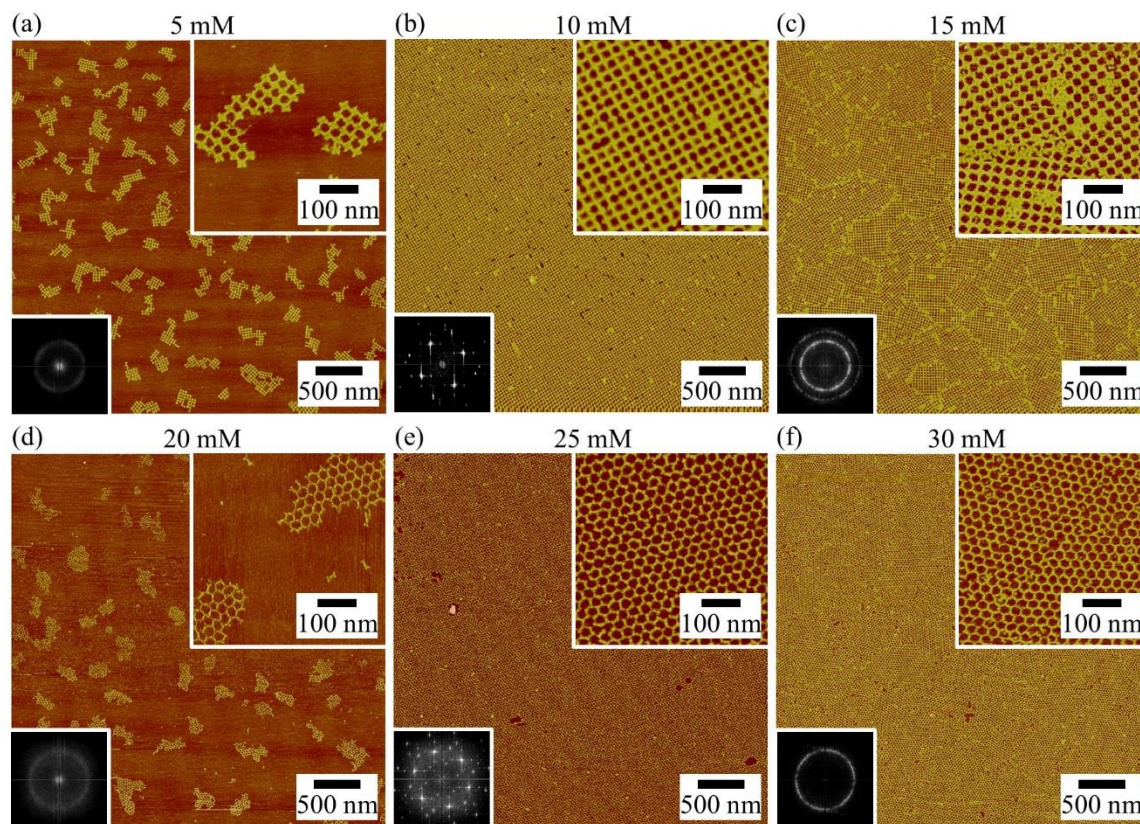
Figure 3.5. Optimization of the self-assembly of defect-free, large, single-crystal DNA arrays by [Mg^{2+}]. (a-c) Regulation of tetragonal arrays by [Mg^{2+}]: 5 mM (low surface coverage), 10 mM (optimal single crystal), 15 mM (poly-crystals). (d-f) Regulation of hexagonal arrays by [Mg^{2+}]: 20 mM (low surface coverage), 25 mM (optimal single crystal), 30 mM (poly-crystals). Buffers: TA/500 mM Na$^+$ plus Mg^{2+} at designated concentration (shown at top of each image). For each large-scale image (4 μm × 4 μm), an FFT pattern and a close-up view are shown at lower left and upper right, respectively.

3.4.2 Testing Integrity of DNA Arrays during "Glue" Coating

Before patterning NPs, one question is whether the formed DNA arrays can be preserved during "glue" coating process. To test the integrity of DNA arrays, we imaged the samples after each step of the process (Figure 3.6). Before coating, DNA arrays were checked to ensure intactness (Figure 3.6 a). For patterning of AuNPs, poly-L-lysine (PLL), a type of strong "glues", was required. To enhance DNA-surface interaction, 2 mM Ni^{2+} was added to PLL solution. After coating with PLL, DNA arrays remained intact (Figure 3.6 b). Next step was to remove excessive, unbound or loosely bound PLL by washing with $TA/Mg^{2+}/Ni^{2+}$ solution, containing 10 mM Mg^{2+} and 2 mM Ni^{2+}. Mg^{2+} was for stabilizing DNA nanostructures and Ni^{2+} was for enhancing DNA-surface interaction. AFM images also confirmed the integrity of DNA arrays after washes (Figure 3.6 c). For patterning of DNA motifs and proteins, PLL coating process was removed because Ni^{2+} is strong enough as "glues". So washing with $TA/Mg^{2+}/Ni^{2+}$ solution would also function as "glue" coating process.
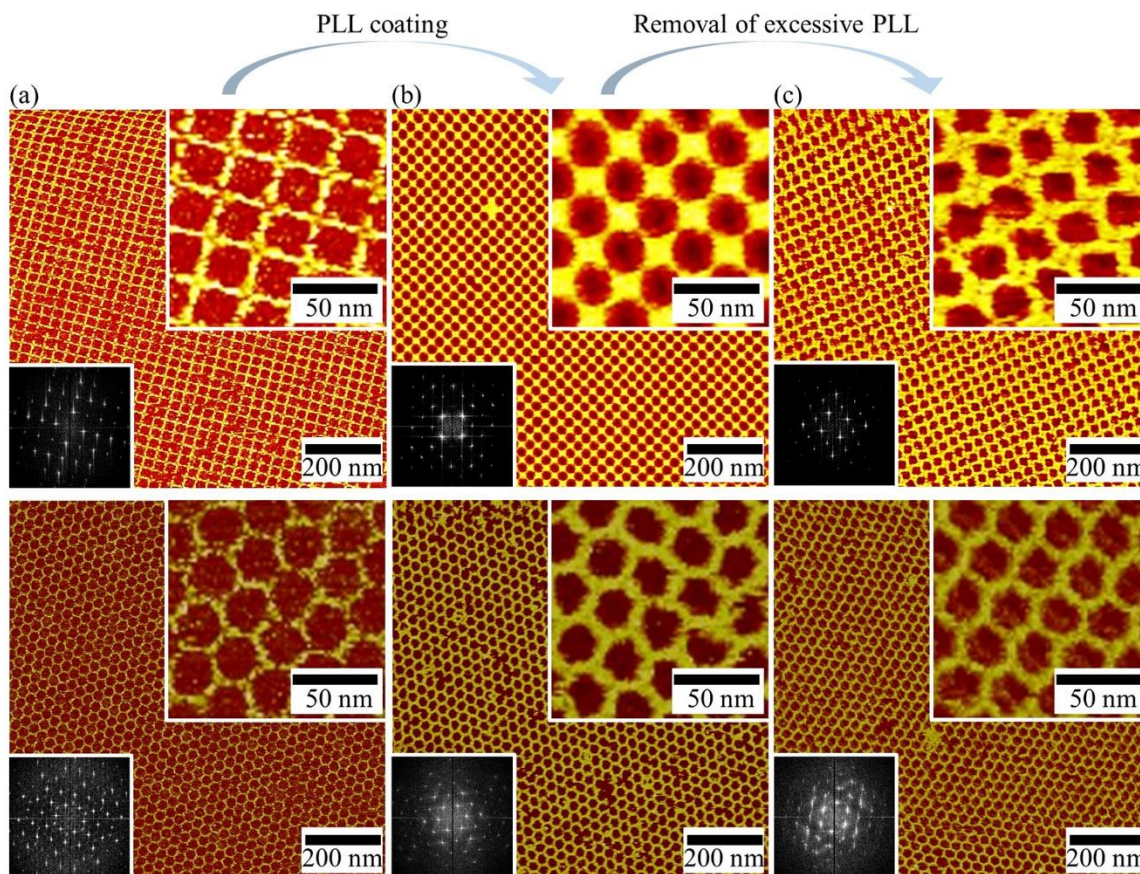
Figure 3.6. Integrity test of DNA arrays during "glue" coating process. AFM images of (a) DNA arrays; (b) followed by poly-L-lysine (PLL) coating; (c) and followed by removing excessive PLL. Note that PLL coating in (b) is only required in AuNP patterning. PLL coating in step (b) is only applied in AuNPs patterning. In all the other NPs patterning, step (b) is removed. For each large-scale image (1 μm × 1 μm), FFT patterns and close-up views are shown at lower left and upper right, respectively. Top layer: tetragonal arrays; bottom layer: hexagonal arrays.

3.4.3   Patterning DNA Nanomotifs

We started our study with patterning of DNA 3-point-star (3PS) motifs (Figure 3.7). This motif contains three identical branches, and each branch contains two parallel DNA duplexes (Figure 3.2 c). One duplex is blunt-ended while the other has a 10T single-stranded overhang at the peripheral end to prevent inter-motif association via blunt-end stacking (Figure 3.2 e). After forming tetragonal or hexagonal arrays, exposure of the mica surfaces to 3PS motifs resulted in cavity-occupied patterning of 3PS motifs (Figure 3.7 a-d). By increasing the concentration of 3PS

motif, [3PS], the cavity occupancy increased from low to high level (Figure 3.8). Our statistical analysis indicated that the cavity occupancy rate could reach almost 100% when [3PS] was 75 nM (Figure 3.7 e).

[3PS] / nM	25	50	75
Tetragonal array	55.9 ± 1.0 %	96.2 ± 0.5 %	99.9 ± 0.1 %
Hexagonal array	38.6 ± 1.9 %	63.6 ± 2.0 %	99.8 ± 0.1 %
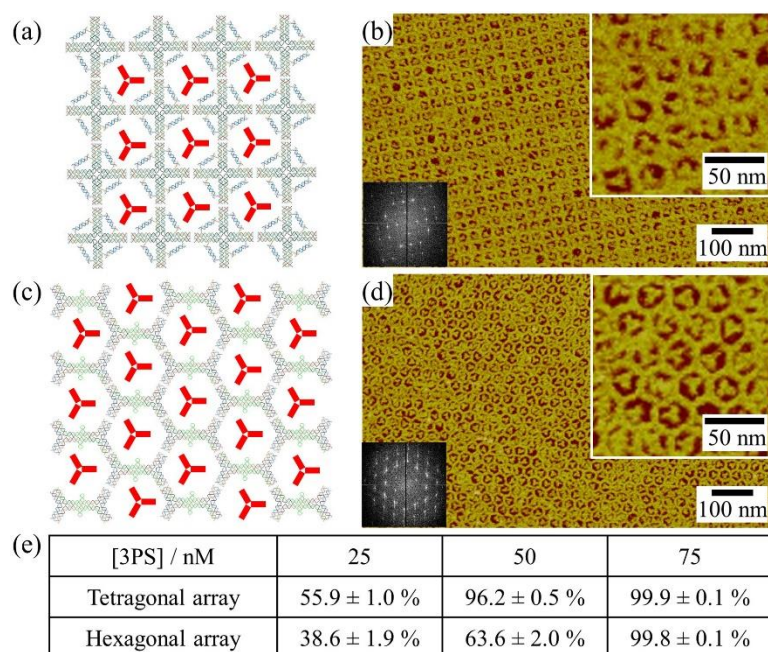
Figure 3.7. Patterning of DNA three-point-star nanomotifs (3PS motifs) by DNA arrays. Schematic presentation of patterning by (a) tetragonal arrays and (c) hexagonal arrays. 3PS motifs are colored red. (b, d) AFM images of (a) and (c). FFT patterns and close-up views are shown at lower left and upper right, respectively. (e) Statistics of cavity occupancy against [3PS].
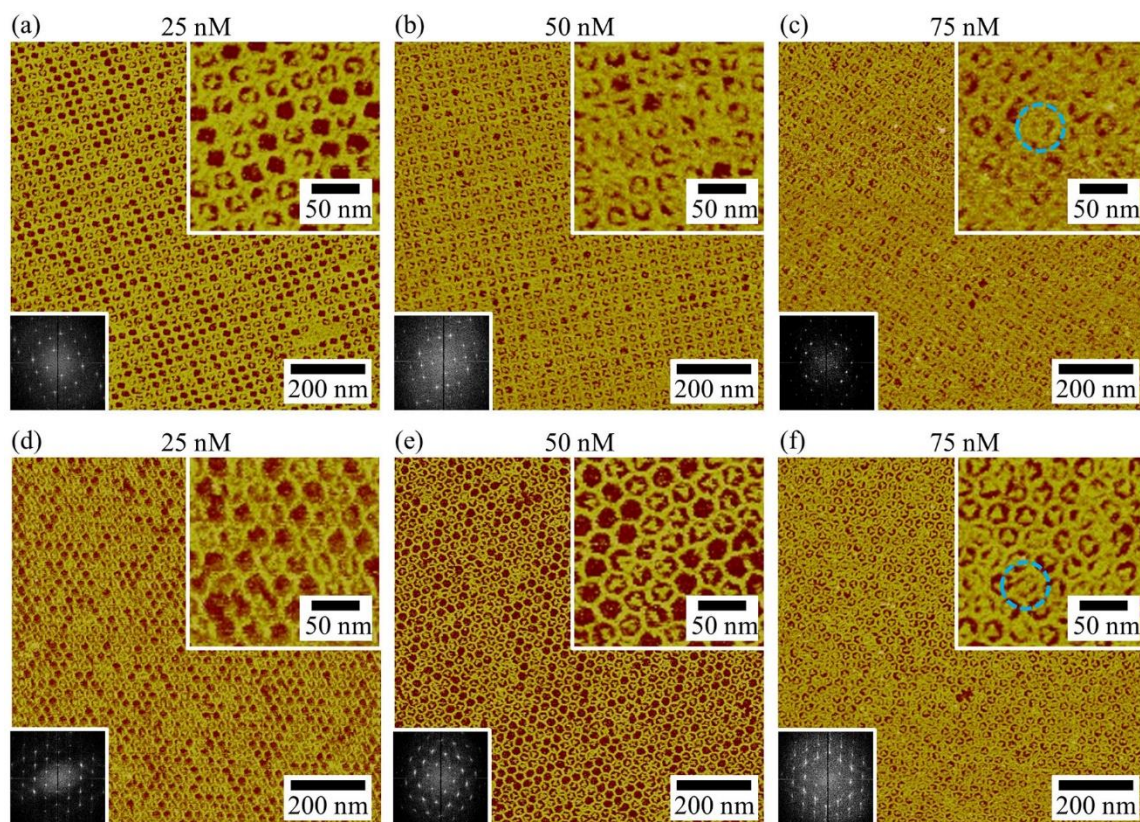
Figure 3.8. Patterning of 3PS motifs by DNA arrays. AFM images of patterning by (a-c) tetragonal arrays and (d-f) hexagonal arrays at designated [3PS] (shown at top of each image). FFT patterns and close-up views are shown at lower left and upper right, respectively. Blue circles indicate dual motifs in a single cavity.

Then we extended our study to another DNA motif, 4-point-star (4PS) motif. 4PS motif has

the same design as 3PS motif except that it contains 4 branches (Figure 3.2 d and e). Similar tunable

patterning results were obtained (Figure 3.9 and 3.10). Almost 100% cavity occupancy was

obtained at [4PS] of 50 nM for tetragonal arrays and 60 nM for hexagonal arrays. Due to the space

limit of the cavity, most DNA motif patterns followed the single-motif-per-cavity rule. However,

when the concentration of DNA motifs was high enough, one cavity could trap two motifs,

highlighted by circles in Figure 3.8 c,f and 3.10 c,f. This was probably because the DNA motifs

contained certain flexibility to adapt themselves to a more compact space.
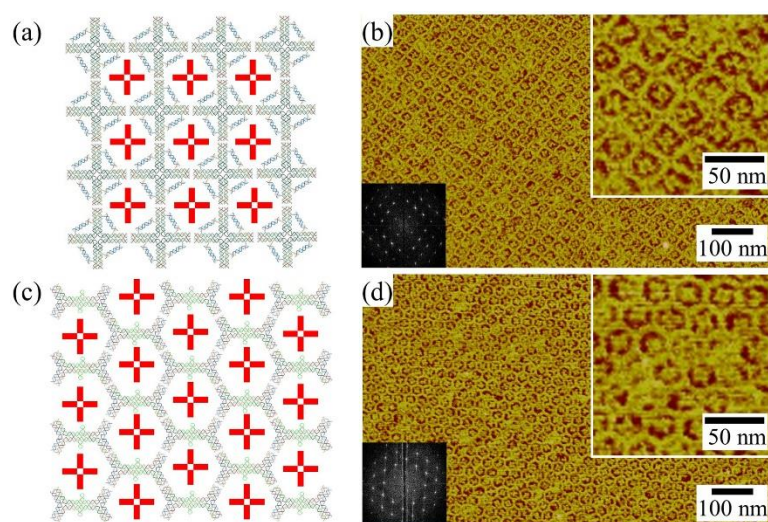
Figure 3.9. Patterning of DNA four-point-star nanomotifs (4PS motifs) by DNA arrays. Schematic presentation of patterning by (a) tetragonal arrays and (c) hexagonal arrays. 4PS motifs are colored red. (b, d) AFM images of (a) and (c). FFT patterns and close-up views are shown at lower left and upper right, respectively.

	Cavity occupancy ([4PS])		
	Low	Moderate	High
Tetragonal array	58.5 ± 2.2 % (20 nM)	75.0 ± 2.0 % (35 nM)	99.7 ± 0.2 % (50 nM)
Hexagonal array	27.2 ± 0.3 % (20 nM)	50.4 ± 0.2 % (40 nM)	98.5 ± 0.2 % (60 nM)
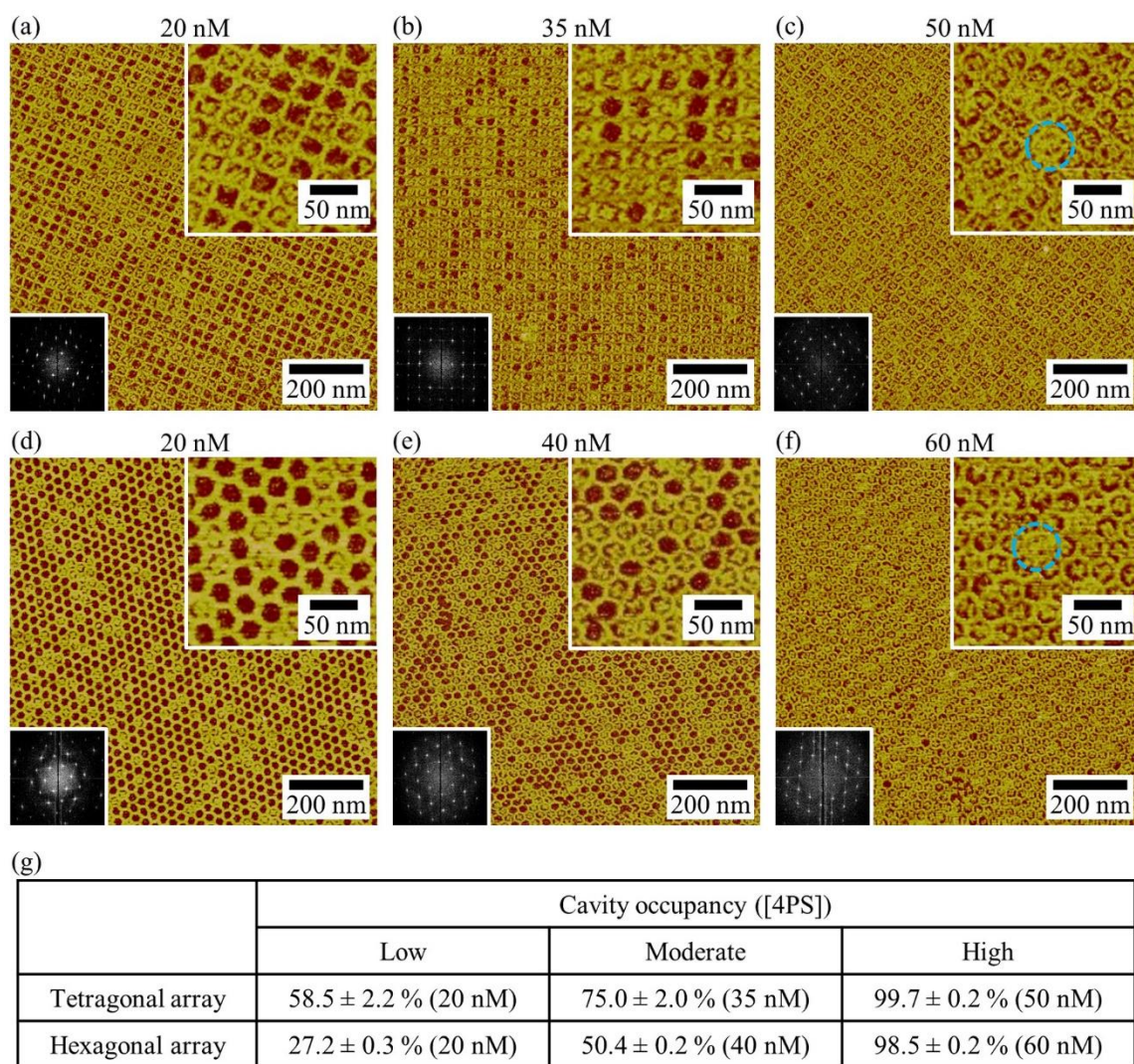
Figure 3.10. Patterning of 4PS motifs by DNA arrays. AFM images of patterning by (a-c) tetragonal arrays and (d-f) hexagonal arrays at designated [4PS] (shown at top of each image). FFT patterns and close-up views are shown at lower left and upper right, respectively. Blue circles indicate dual motifs in a single cavity. (g) Statistical analysis of cavity occupancy against [4PS].

3.4.4   Patterning AuNPs

AuNPs are one of the most important metal colloids for their unique physical properties and wide applications in electronics, plasmonics, biomaterials, etc.[93-96] Since Mirkin *et al.* firstly reported modification of AuNPs with DNA oligonucleotides,[17] this method has been broadly applied to organize AuNPs in various 1D,[97] 2D,[97] and 3D lattices,[98,99] and satellite shapes.[100-102]

An alternative strategy to order AuNPs is self-assembly of AuNPs templated by DNA nanostructures.[18,103,104] Both methods require strict DNA sequence design to enable specific DNA-DNA hybridization. To achieve patterning AuNPs in a non-specific way, Cheng and coworkers reported a free-standing NP superlattice by using DNA-modified AuNPs.[105] In their work, DNA was used as a "dry ligand" instead of a recognizable tool. However, their nanopatterning was limited to close-packed hexagonal shape due to lack of templating guidance. Our previous work showed a DNA-templated fabrication of AuNPs by thermal evaporation coating.[106] But it suffered from discrete distribution of AuNPs on DNA templates and difficult control of uniform size of AuNPs. Herein, we used our current method to pattern AuNPs by DNA arrays. AuNPs of 5 and 10 nm were used after modification with 22-nt, single-stranded, random-sequenced DNA. To ensure efficient absorption, mica surfaces were coated with PLL, a strong positively-charged "glue" (Figure 3.6). Figure 3.11 demonstrated the necessity of PPL coating. Note that the overall diameters of DNA-modified AuNPs at dry conditions are ~ 5.8 nm (for 5 nm AuNP) and ~ 10.5 nm (for 10 nm AuNP). Both are much smaller than the cavities of the DNA 2D arrays (~ 27.4 nm for square wells and ~ 30.3 nm for hexagonal wells).
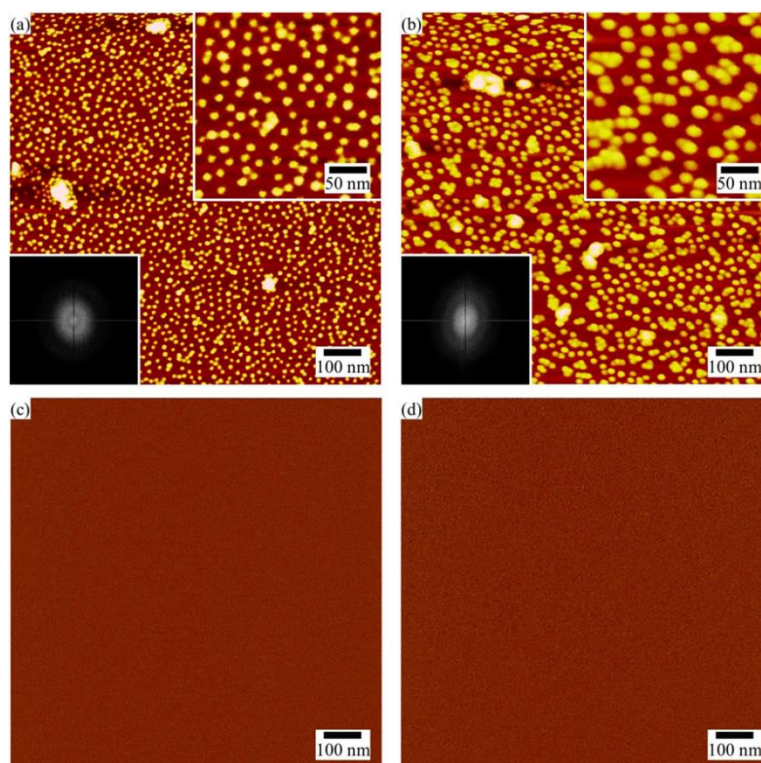
Figure 3.11. AFM images at different magnifications of random absorption of (a) 5-nm and (b) 10-nm AuNPs on PLL-modified mica surfaces. FFT patterns and close-up views are shown at lower left and upper right, respectively. AFM images of (c) 5-nm and (d) 10-nm AuNPs on unmodified mica surfaces.

Figure 3.12 illustrated AuNPs patterned by tetragonal DNA arrays. AuNPs (red spheres) stood in the cavities formed by tetragonal arrays as shown in Figure 3.12 a. After formation of tetragonal arrays from b4PS motifs (Figure 3.12 b) and PLL coating, 5 – or 10 – nm AuNPs were deposited onto mica surfaces and visualized by AFM. AFM images of both 5- and 10 – nm AuNP patterns indicated tetragonal ordering directed by DNA arrays, and their FFT patterns showed clear tetragonal symmetry (Figure 3.12 c-d), which was obviously different from template-free, random absorption (Figure 3.11 a and b). White lines in Figure 3.12 c and d indicated the orientations of patterned AuNPs, which agreed with the corresponding FFT patterns. Due to different sizes of two

AuNPs, one cavity of tetragonal DNA arrays preferred to hold multiple 5-nm AuNPs (Figure 3.12

c) but single 10-nm AuNP (Figure 3.12 d).
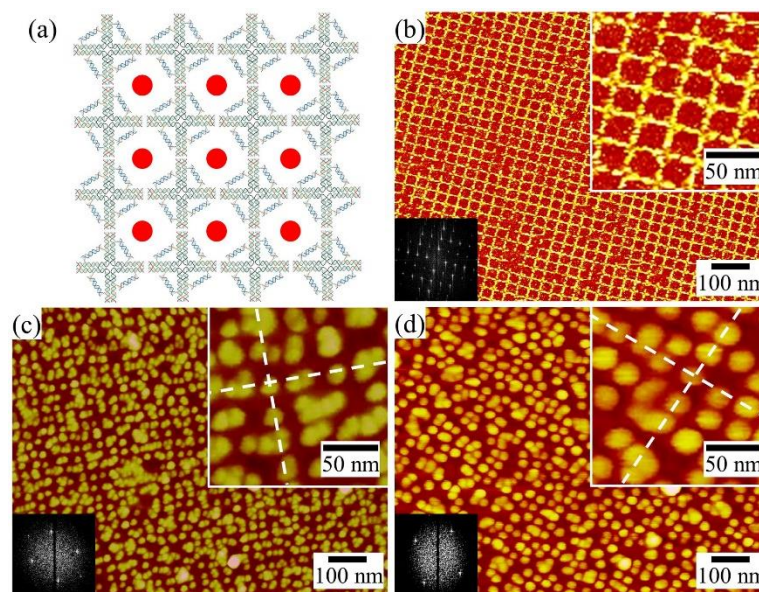
Figure 3.12. (a) Schematic presentation of AuNPs patterning by tetragonal DNA arrays. AuNPs
are colored red. (b) AFM image of tetragonal arrays. (c, d) AFM image of patterned 5 – and 10 –
nm AuNPs, respectively. A set of white dashed lines indicate the orientation of patterned AuNPs.
In (b-d), FFT patterns and close-up views are shown at lower left and upper right, respectively.

Due to the height difference contrast between AuNP and DNA (AuNP at ~ 5.8 nm and ~

10.5 nm against DNA at ~ 2 nm), AFM images only displayed higher AuNP patterns when AuNPs

were compactly packed. How can we determine the DNA arrays' templating effect on AuNPs?

One method was to reduce the density of AuNPs. A map of sparse AuNPs was obtained, which

allowed observation of AuNPs and DNA arrays at the same time (Figure 3.13). A close-up view

indicated most AuNPs stood in the cavities formed by DNA arrays, which confirmed our

hypothesis (Figure 3.13 b). Furthermore, Figure 3.14 showed measured repeating distances of 5-

and 10- nm AuNP lattices, which were close to that of DNA arrays. This also confirmed DNA

arrays' templating effect on AuNPs regardless of their sizes.
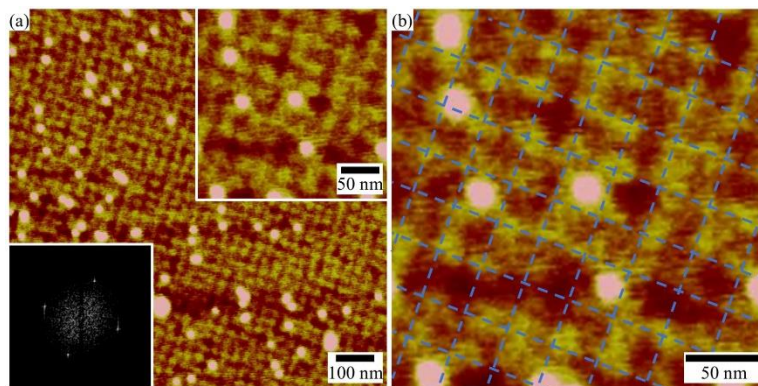
Figure 3.13. Spatial relationship between AuNPs and DNA arrays. (a) AFM image of 5-nm AuNPs (white spheres) at low concentration (50 nM) on tetragonal arrays (yellow networks). FFT pattern and close-up view are shown at lower left and upper right, respectively. (b) Close-up view of (a). Blue dashed networks are drawn to highlight DNA array.
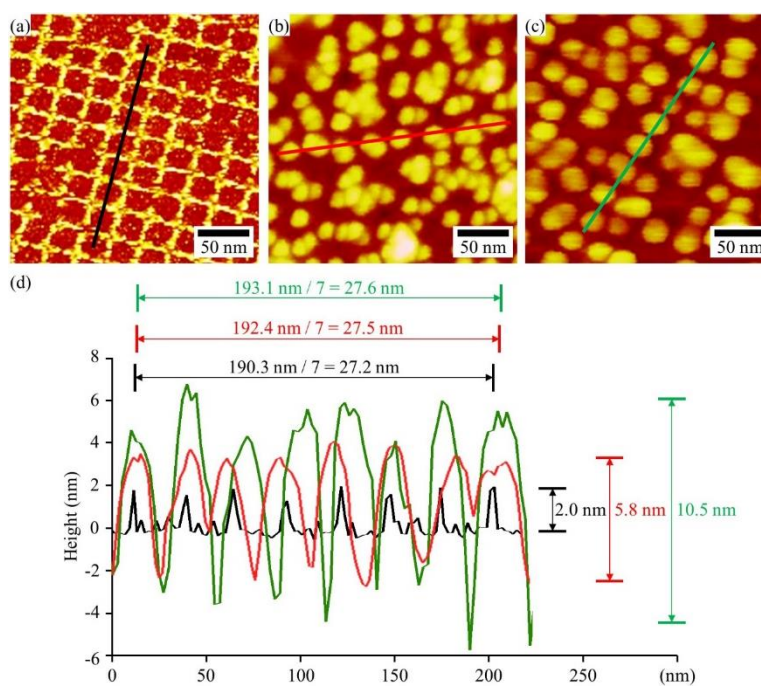
Figure 3.14. Height and repeating distance analysis of DNA arrays and patterned AuNPs. (a) AFM images of tetragonal arrays. (b, c) AFM images of patterned 5 – and 10 – nm AuNPs by tetragonal DNA arrays. (d) Height analysis of (a-c) along corresponding colored lines. Averaged heights and repeating distances are labeled beside and above the figure with corresponding colors in (a-c).

To study the percentage of cavities occupied by AuNPs, we performed an FFT analysis

(Figure 3.15). Briefly, FFT patterns were generated from the AFM images. Then diffraction spots

of tetragonal symmetry, highlighted by green circles, were selected (Figure 3.15 a and c) and were used to generate inverse FFT images via inverse FFT operation (Figure 3.15 b and d). In the inverse FFT images, dot patterns of tetragonal symmetry were shown in three different colors: (*i*) Yellow dots represented AuNP-occupied cavities, highlighted by circles; (*ii*) Red dots represented AuNP-unoccupied cavities, highlighted by squares; (*iii*) White dots represented AuNP aggregates, highlighted by hexagons. Their positions in original AFM images were also matched, highlighted by corresponding shapes. Statistical analysis indicated cavity occupancy of 94.9 ± 0.3 % for 5 – nm AuNPs and 80.8 ± 1.2 % for 10 – nm AuNPs. The higher occupancy for 5 – nm AuNPs is probably due to their higher concentration in bulk solution.
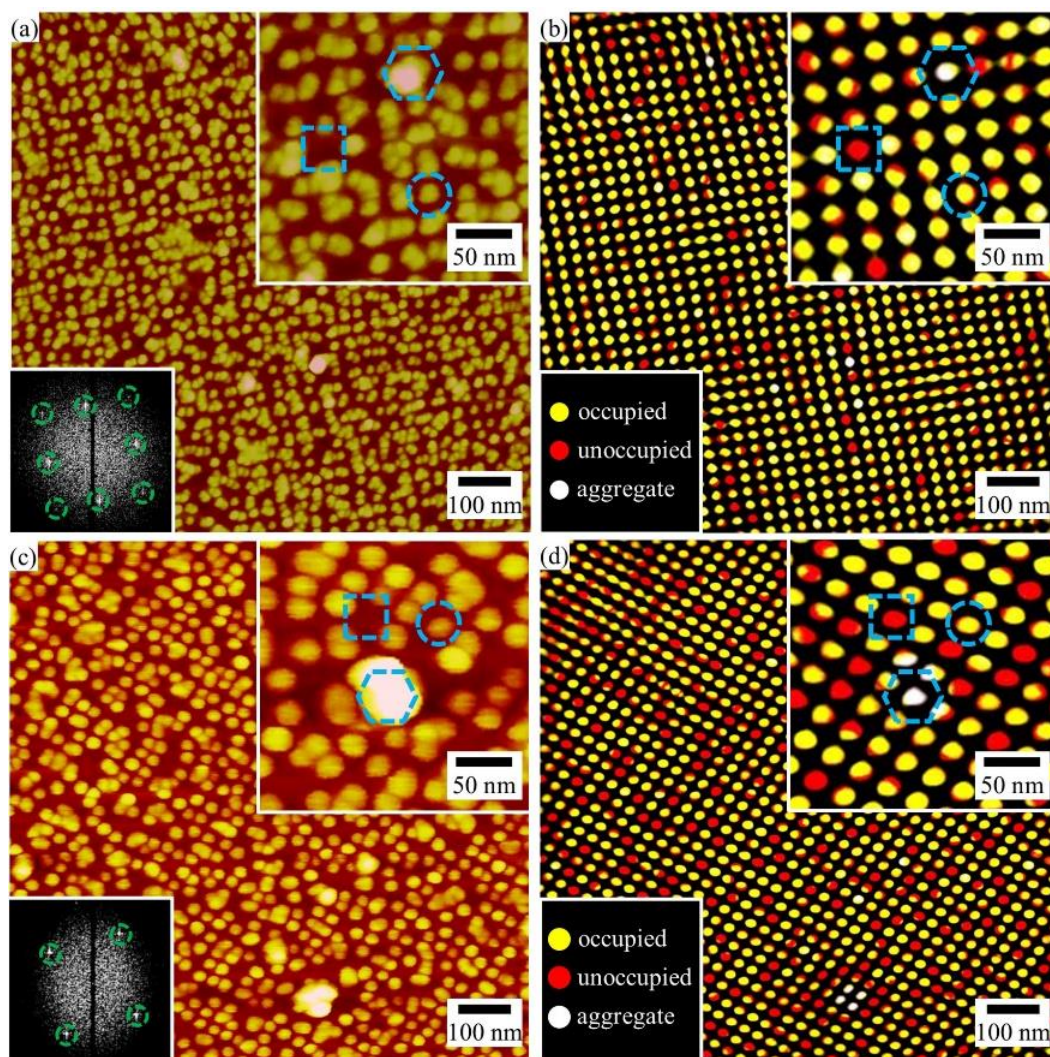
Figure 3.15. (a, c) 5- and 10- nm patterned AuNPs by tetragonal arrays. FFT patterns and close-up views are shown at lower left and upper right, respectively. (b, d) Inverse FFT images of (a) and (c) from diffraction spots in green dashed circles. Yellow dots stand for AuNP-occupied cavities, highlighted by blue dashed circles; red dots stand for AuNP-unoccupied cavities, highlighted by blue dashed squares; and white dots stand for AuNP aggregates, highlighted by blue dashed hexagons. In close-up views at upper right, three types of dots are highlighted, corresponding with those in (a) and (c).

We also examined 5 – nm AuNPs patterned by the hexagonal arrays (Figure 3.16). Similarly, white dashed lines showed three organizing orientations, which agreed with the FFT diffraction patterns of hexagonal symmetry (Figure 3.16 c). In the inverse FFT images, colored dot patterns

revealed the ordering of AuNPs and the cavity occupancy (Figure 3.16 d). This also demonstrated the versatility of DNA templates.
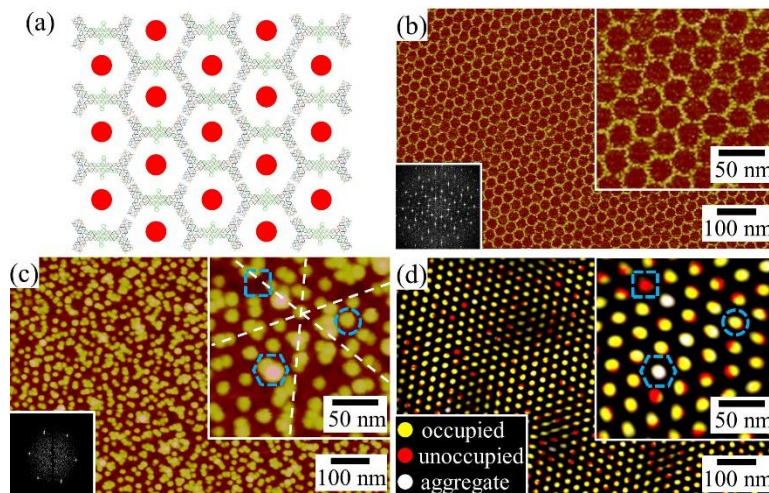
Figure 3.16. Patterning of AuNPs by hexagonal DNA arrays. (a) Schematic presentation of AuNPs patterning by hexagonal arrays. AuNPs are colored red. (b) AFM image of hexagonal arrays. (c) AFM image of patterned 5-nm AuNPs. A set of white dashed lines indicate the orientation of patterned AuNPs. In (b-c), FFT patterns and close-up views are shown at lower left and upper right, respectively. (d) Inverse FFT image of (c) is generated from diffraction spots. Yellow dots stand for AuNP-occupied cavities, highlighted by blue dashed circles; red dots stand for AuNP-unoccupied cavities, highlighted by blue dashed squares; and white dots stand for AuNP aggregates, highlighted by blue dashed hexagons. In close-up views at upper right, three types of dots are highlighted, corresponding to those in (c).

3.4.5   Patterning Proteins

Patterning proteins directed by DNA arrays has been broadly reported. Specific binding was the most commonly used technique, e.g. streptavidin-biotin binding[11,43,107,108] and antigen-antibody interaction.[109] Recently, Ramakrishnan *et al.* reported non-specific absorption of various negatively-charged proteins directed by surface-assembled DNA origami nanostructures.[110] Herein, we used our system to pattern proteins, both negatively and positively-charged. Moreover, our DNA arrays contained denser cavities (~ 1,200 or 2,000 cavities per μm^2) compared with those in the origami arrays (~ 100 cavities per μm^2).[110]

We firstly studied the negatively-charged ovalbumin (OVA, pI ~ 4.52).[111] OVA is a main protein in egg white, consisting of 385 residues with a molecular weight of ~ 42.7 kDa.[112] OVA adsorption on mica surface was controlled by [OVA] in bulk solution. Figure 3.17 showed AFM images of patterned OVAs by tetragonal and hexagonal arrays at [OVA] of 25 and 75 nM. At 25 nM, cavities were partially occupied and preferred to load single OVA per cavity (Figure 3.17 c and e). Increasing [OVA] resulted in higher cavity occupancy (Figure 3.18 and 3.19). When [OVA] reached 75 nM, almost all cavities were occupied, and each cavity preferred to load multiple OVAs (Figure 3.17 d and f). When we further investigated OVA patterning directed by tetragonal arrays by increasing [OVA] up to 400 nM, almost all cavities were occupied with crowded OVAs (Figure 3.18).
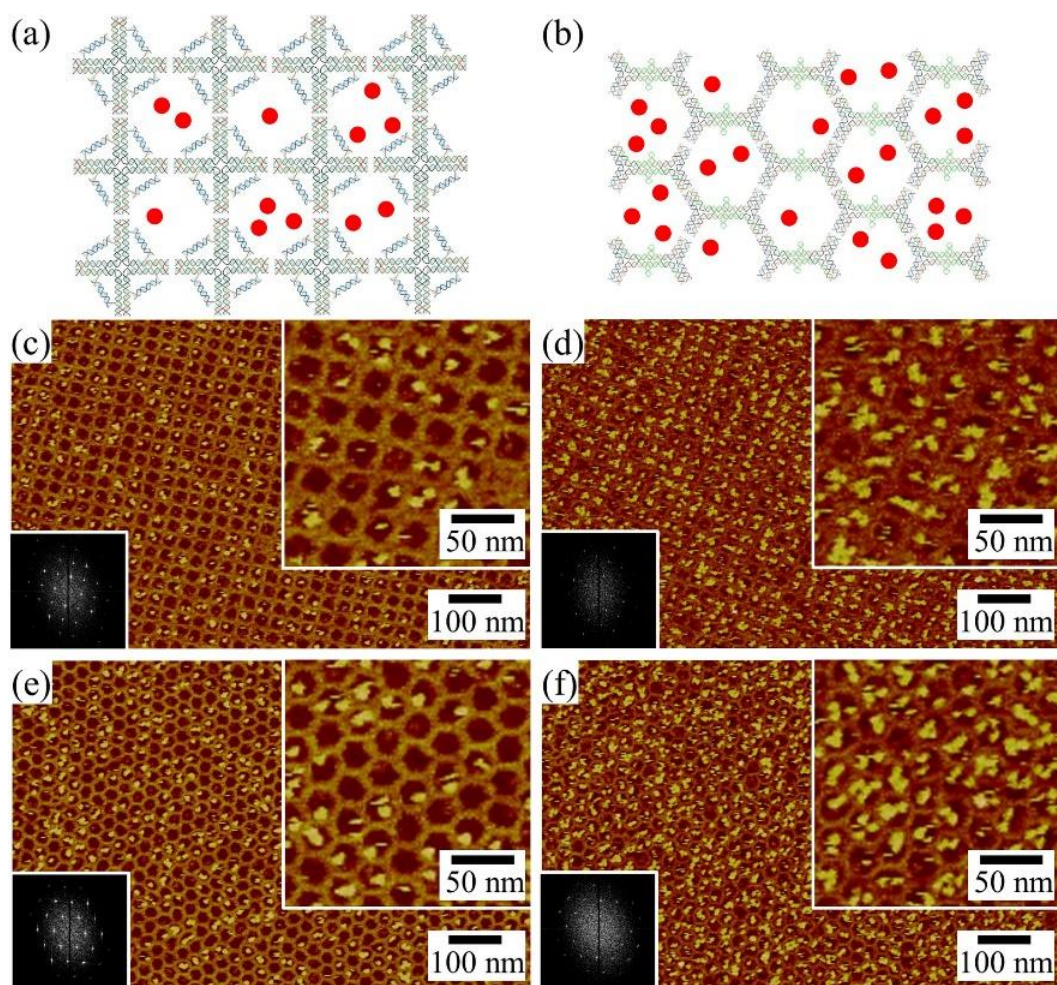
Figure 3.17. (a, b) Schematic presentations of ovalbumin (OVA) patterning by DNA arrays. OVAs are colored red. (c, d) AFM images of patterned OVAs by tetragonal arrays at different concentration of OVA ([OVA]). (e, f) AFM images of patterned OVAs by hexagonal arrays at different [OVA]. In (c-f), FFT patterns and close-up views are shown at lower left and upper right, respectively. [OVA] is 25 nM for (c, e) and 75 nM for (d, f).
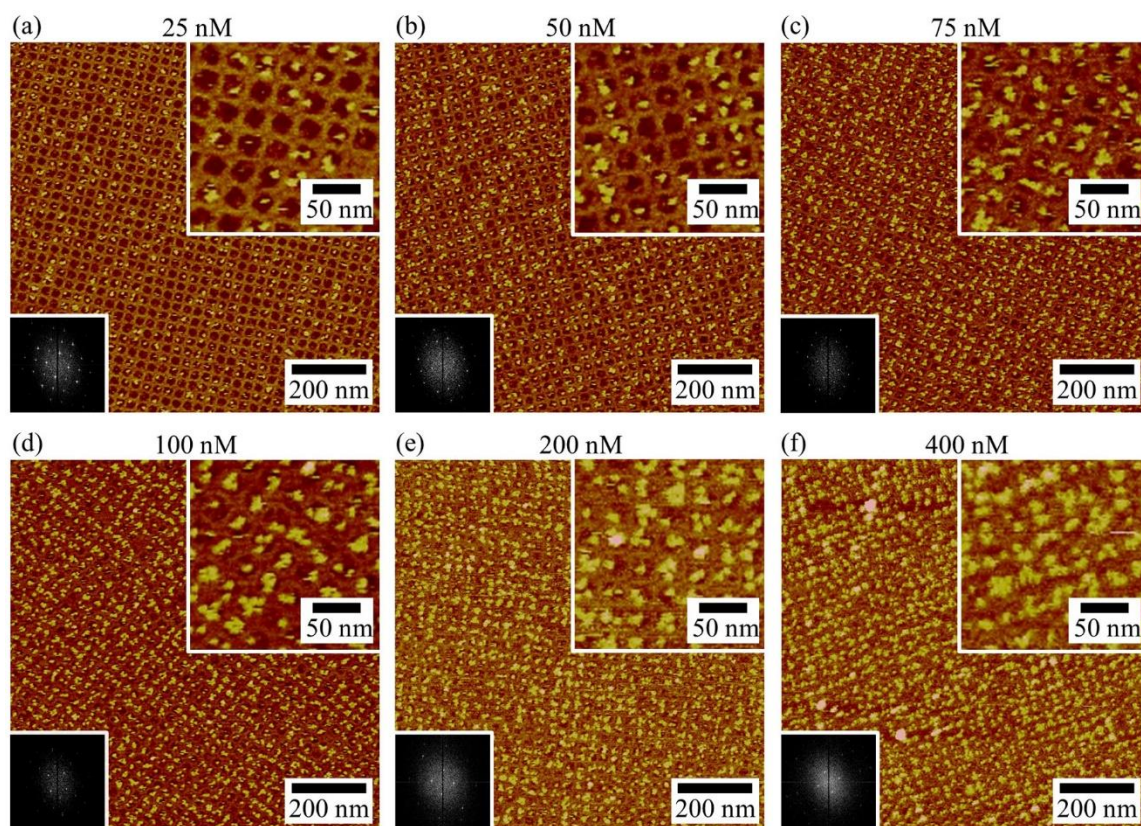
Figure 3.18. AFM images of patterned OVAs by tetragonal arrays at (a-f) designated [OVA] (shown at top of each image). FFT patterns and close-up views are shown at lower left and upper right, respectively.
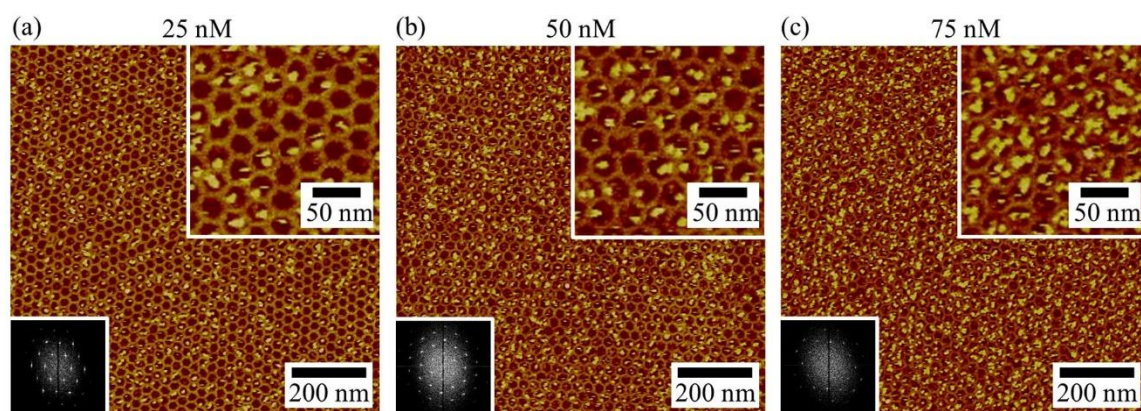
Figure 3.19. AFM images of patterned OVAs by hexagonal arrays at (a-c) designated [OVA] (shown at top of each image). FFT patterns and close-up views are shown at lower left and upper right, respectively.

Then, we studied the positively-charged lysozyme (LYZ, pI ~ 11.35).[113] LYZ is also abundant in egg white, consisting of 129 residues with a molecular weight of ~ 14.3 kDa.[114] Different from OVA, LYZ could directly absorb on either mica surfaces or DNA backbones. Figure 3.20 showed AFM images of patterned LYZs by tetragonal and hexagonal arrays at [LYZ] of 100, 150, and 200 nM. LYZs could easily be identified in the cavities but LYZ concentration had relatively less influence on the cavity occupancy. Interestingly, at high [LYZ] of 200 nM, the DNA arrays blurred possibly due to massive accumulation of LYZ on DNA backbones (Figure 3.20 17 c and f).
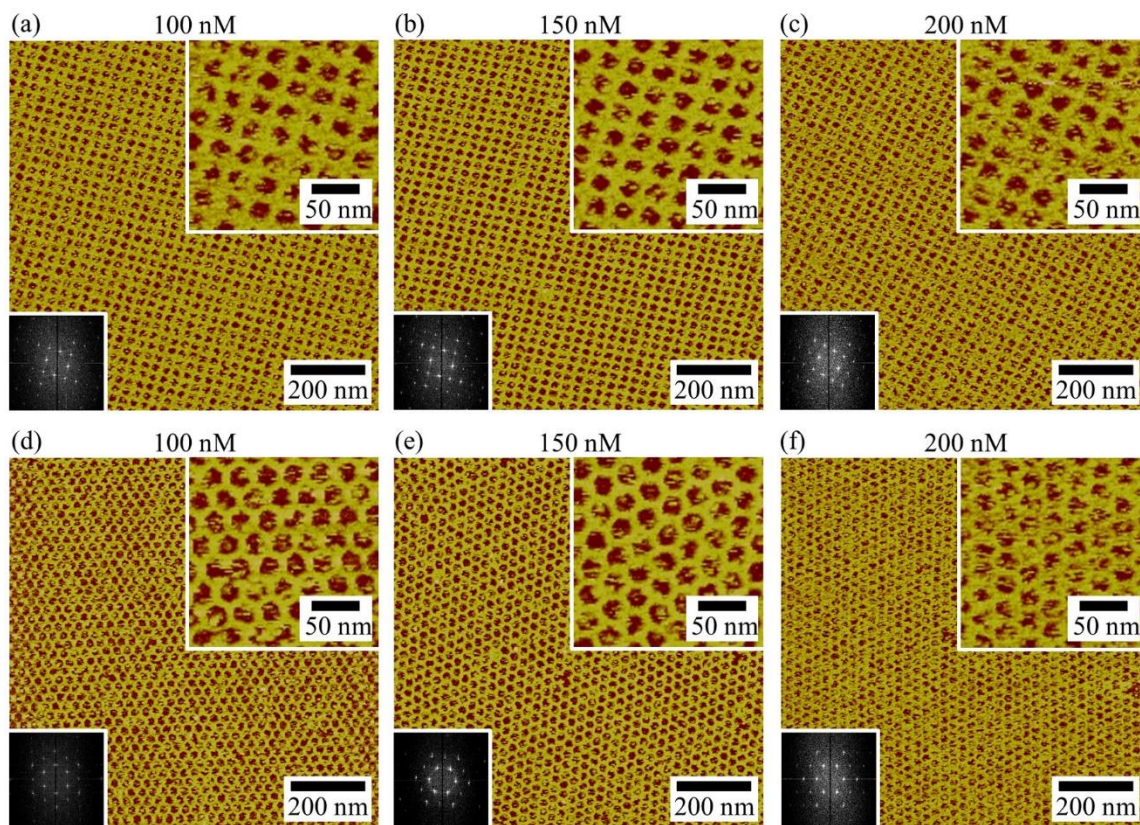
Figure 3.20. AFM images of patterned lysozyme (LYZ) by (a-c) tetragonal arrays and (d-f) hexagonal arrays at designated [LYZ] (shown at top of each image). FFT patterns and close-up views are shown at lower left and upper right, respectively.

3.4.6 DNA-Silica Hybrid Networks

In a recent milestone works, a general method was introduced by Yan, Fan et al. to grow silica nanostructures with DNA nanostructures as templates.[115,116] Herein, we applied this method to construct DNA-silica hybrid networks, in other words, organizing in-situ synthesized, tiny silica particles along DNA backbones. Figure 3.21 a and b showed a pair of AFM images of tetragonal and hexagonal arrays with 48-hour silica growth. Height analysis indicated that the height of network backbones increased to ~ 4 nm, which was twice the height of DNA duplexes (Figure 3.21 c and d). To investigate the process of the silica growth, we captured AFM images at different incubation time points (Figure 3.22). At 1 hour, silica complex was rarely observed on DNA backbones. At 2 hours, silica complex started to partially covered DNA backbones. Both bared DNA backbones and silica-decorated backbones were observed (Figure 3.22 b). At 4 hours, silica complex continued to cover more area of DNA arrays. Starting from 24 hours, the silica-covered DNA arrays reached about ~ 100%. Statistical analysis revealed an increasing height between 0 hour to 24 hours and a stable, maximum height of ~ 4 nm after 24 hours (Figure 3.21 e).
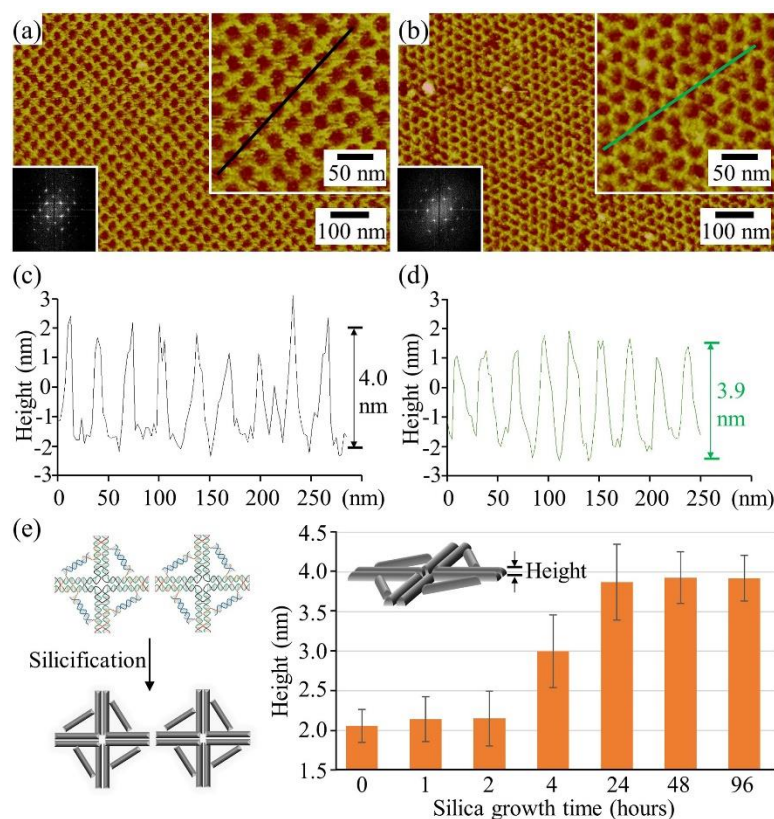
Figure 3.21. Silicification of DNA arrays. (a, b) Tetragonal arrays and hexagonal arrays with 48-hour silica growth. FFT patterns and close-up views are shown at lower left and upper right, respectively. (c, d) Height analysis of (a) and (b) along corresponding colored lines. Averaged heights are labeled beside the figures. (e) Height change of tetragonal arrays along increasing silica growth time. Process from tetragonal DNA arrays to silica-decorated structures by silicification.
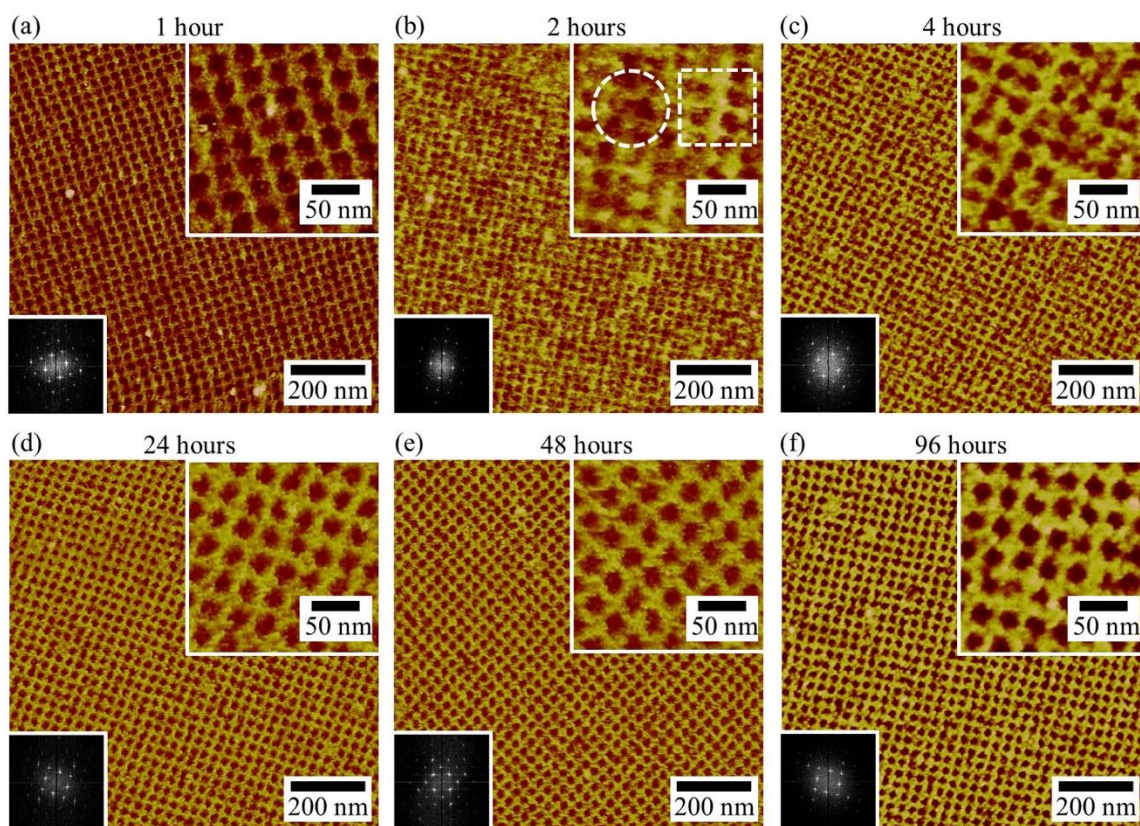
Figure 3.22. AFM images of silica-decorated tetragonal arrays with (a-f) designated silica growth time (shown at top of each image). FFT patterns and close-up views are shown at lower left and upper right, respectively. In (b), a piece of bare DNA array and silica-decorated array are highlighted by a white dashed circle and square.

3.5   Conclusion

In summary, we have developed a biotemplating strategy for ordering various NPs into expected 2D patterns via NP-surface or NP-DNA interaction. The absorption relies on non-specific charge-charge interaction, which makes it a general approach. The NPs include DNA nanomotifs, AuNPs, proteins, and silica complex, which demonstrates the versatility of this method. By tuning the concentration of NPs in bulk solution, it is feasible to achieve different cavity occupancy. This overall strategy will be expected to order a large range of NP candidates into designated patterns.

CHAPTER 4.   RATIONAL DESIGN AND SELF-ASSEMBLY OF TWO-DIMENSIONAL, DODECAGONAL DNA QUASICRYSTALS

4.1   Introduction

Quasicrystals have been extensively studied in mathematics, physics and material sciences over last three decades. This class of materials exhibits long-range order but lacks translational symmetry. The first observation of quasicrystals came from metal alloys,[117] followed by a variety of materials, including nanoparticles,[118,119] mesoporous silica,[120] hydrogen-bond-driven molecules,[121] and metal-organic frameworks.[122] Although many quasicrystal structures have been discovered in nature and in human engineered systems by serendipity, the rational design and engineering of quasicrystal structures remain a challenge. Theoretical design is straightforward in mathematics sense,[123-125] but physical realization is prohibited by the difficulty of the design of suitable building bricks.

DNA provides an excellent model system for studying quasicrystal formation because of its excellent programming capability and structural simplicity. Self-assembly of small DNA motifs into large structures allows growing crystal lattices by using small sets of short, single-stranded DNAs (ssDNAs).[11,43,52,55] Recently, we have reported a strategy to assemble large DNA 2D arrays via blunt-end stacking on solid surface with several advantages: (1) high efficiency, (2) high surface coverage and large domain size, and, very importantly, (3) increased toleration of motif flexibility and avoiding formation of 3D aggregates.[77] Inspired by these works, herein, we propose a framework to rationally engineer dodecagonal quasicrystals with 12-fold diffraction symmetry

from binary DNA tiles, bridged 5- and 6-point-star motifs (b5PS and b6PS). How can we control the flexibility/rigidity of point-star motifs? This will be a main problem solved in this chapter.

4.2 Scheme and Design

Figure 4.1 illustrates our overall design. A dodecagonal, 2D quasicrystal lattice can be dissected into three basic building blocks: two 5-branch vertices and one 6-branch vertex. While the 6-branch vertex [**III** (3^6)] has a 6-fold rotational symmetry, the 5-branch vertices adapt asymmetric configurations, either **I** ($3^2 \cdot 4 \cdot 3 \cdot 4$) or **II** ($3^3 \cdot 4^2$). DNA motifs, b5PS and b6PS, would perfectly serve as such building bricks. The DNA nanomotifs are designed to enable smart rigidity control and effective self-assembly in 2D. Each DNA motif contains six different types of single-stranded DNAs, ssDNAs (Figure 4.2). All branches in a motif are identical to each other and each branch is a 4-turn-long, DNA double crossover structure. Between any two adjacent branches in a motif, a DNA bridge is introduced to control the angle between the two adjacent branches and the rigidity of the motif. In the current design, the bridge length should range from 7.7 nm (60°) to 10.2 nm (90°), Figure 4.3 a. The bridge is a rigid, 20-base pair (bp)-long duplex (6.9 nm, Figure 4.3 b) flanked with two flexible, ssDNA spacers. Each nucleotide (nt) in an ssDNA can be stretched to ~ 0.67 nm long. For the b6PS motif, 1-nt-long spacers are used so that the inter-branch angle is fixed at approximately 60°. The requirement for the b5PS motif is quite delicate. It should be sufficiently rigid to prevent random aggregate formation. It should also be sufficiently flexible to all both conformations **I** and **II**, which have inter-branch angles both 60° and 90°. So, 3-nt-long spacers are used for b5PS. When the spacers are stretched, the inter-branch angle can reach 90°; when the spacers are relaxed, the inter-branch angle can adapt 60°. These bridges are important to control the rigidity/flexibility for those motifs. Without the bridges, similar motifs (unbridged 5PS and 6PS) are too flexible and could not maintain their designed geometry during assembly. Some

inter-branch angles become 0°, which completely ruins the self-assembly (Figure 4.4 and 4.5).

Finally, to promote inter-branch interaction between two adjacent motifs, two 1-nt-long sticky

ends are introduced at the peripheral end of each branch.
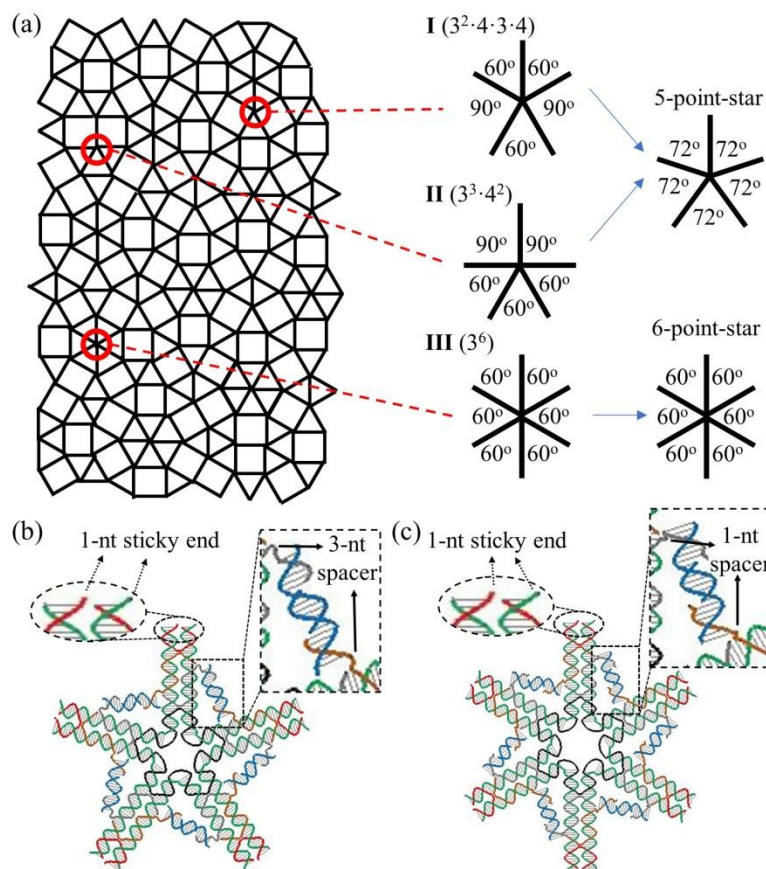
Figure 4.1. Rational design of dodecagonal quasicrystals. (a) A dodecagonal, 2D quasicrystals can be dissected into three different vertices, **I**, **II**, and **III**, highlighted by red circles. Both **I** and **II** are 5-point-star motifs (5PS) and **III** is a 6-point-star motif (6PS). (b) and (c) show the corresponding molecular designs of symmetric, bridged 5- and 6-point-star, DNA motifs, b5PS and b6PS (drawing by Tiamat). While the DNA b6PS motif is rigid, the b5PS motif is engineered to contain certain flexibility to accommodate both **I** or **II** conformations. nt: nucleotide.
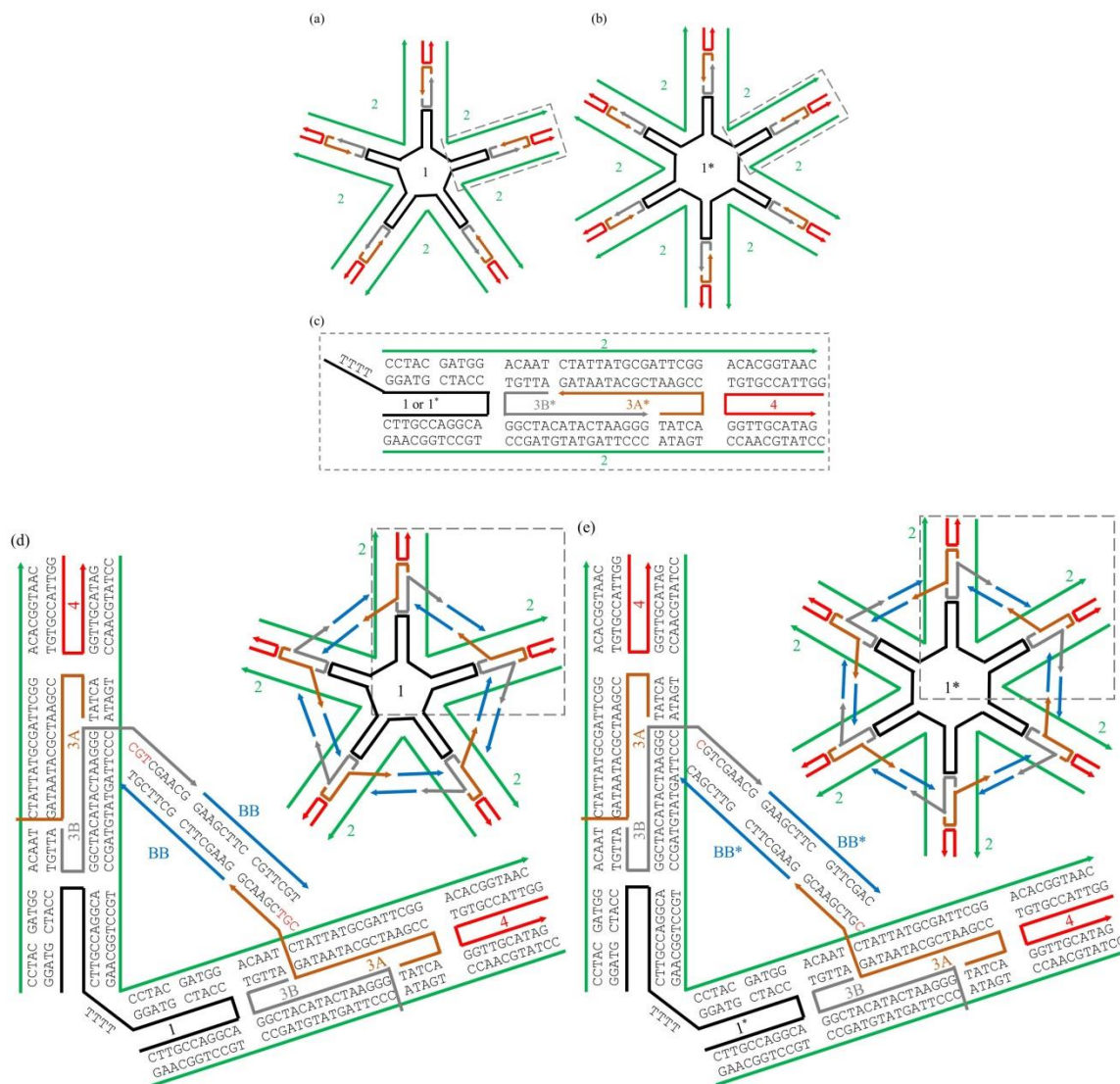
Figure 4.2. Schemes of symmetric, 5- and 6- point-star motifs without and with bridges: 5PS, 6PS, b5PS, and 6bPS. (a) 5PS motif. (b) 6PS motif. (c) Detailed view of one branch (dashed rectangular box) of (a) and (b). (d) b5PS motif. (e) b6PS motif. Each motif has either a 5- or 6-fold rotational symmetry, which renders that all the branches and bridges are identical in terms of both structure and DNA sequences. The duplex bridges between the branches in motifs b5PS and b6PS contain 3 and 1 unpaired nucleotides at both ends (sequence colored red), respectively.
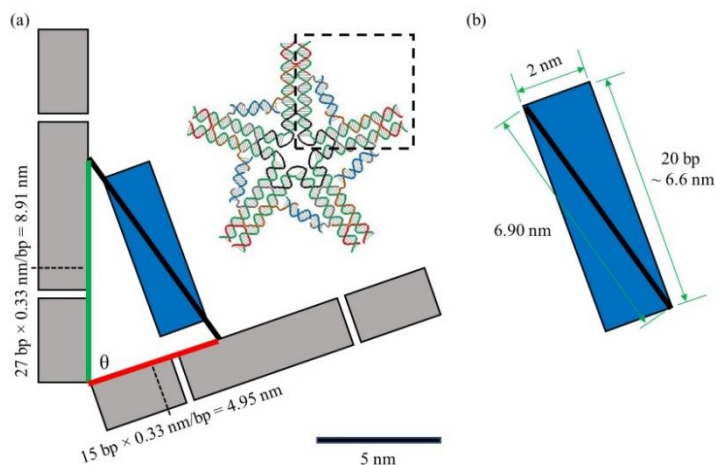
$$bridge^2 = 8.91^2 + 4.95^2 - 2 \times 8.91 \times 4.95 \times \cos\theta$$

Varying θ from 60° to 90°, the bridge should range from 7.73 nm to 10.19 nm.

Figure 4.3. Calculation of the targeted bridge length. We assume the pitch and the diameter of DNA duplexes are 0.33 nm/bp and 2 nm, respectively. The length of one base in ssDNA is 0.67 nm. Calculated number of nucleotides (nts) for the spacer is 0.62 (rounded to 1) and 2.46 (rounded to 3) for inter-branch angle of 60° and 90°, respectively. For b5PS, 3- nt spacers are used to control the inter-branch angle between 60° and 90°, which corresponds to the two configurations **I** and **II** in Figure 1a. For b6PS, 1-nt spacers are used to fix the inter-branch angle at approximately 60°.
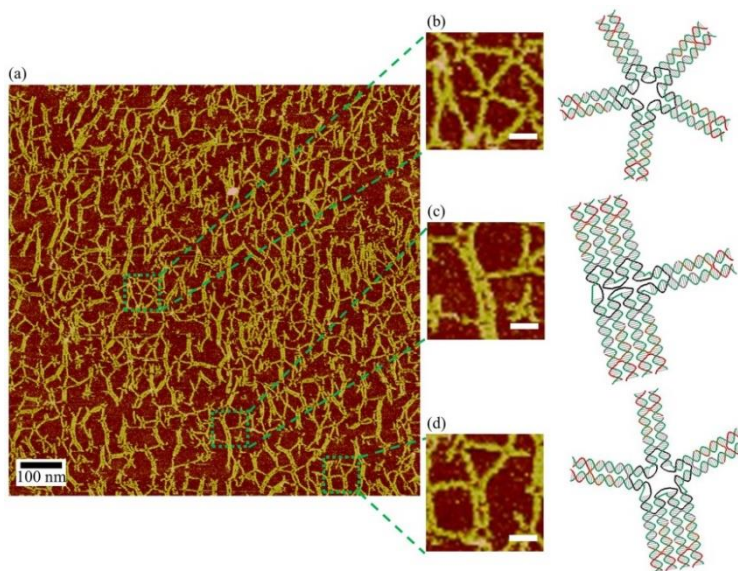
Figure 4.4. Deformation of 5PS motif during surface assembly. (a) AFM image of 2D networks assembled by 5PS. (b-d) Close-up views and corresponding structural schemes of different 5PS conformations. Scale bar: 20 nm.
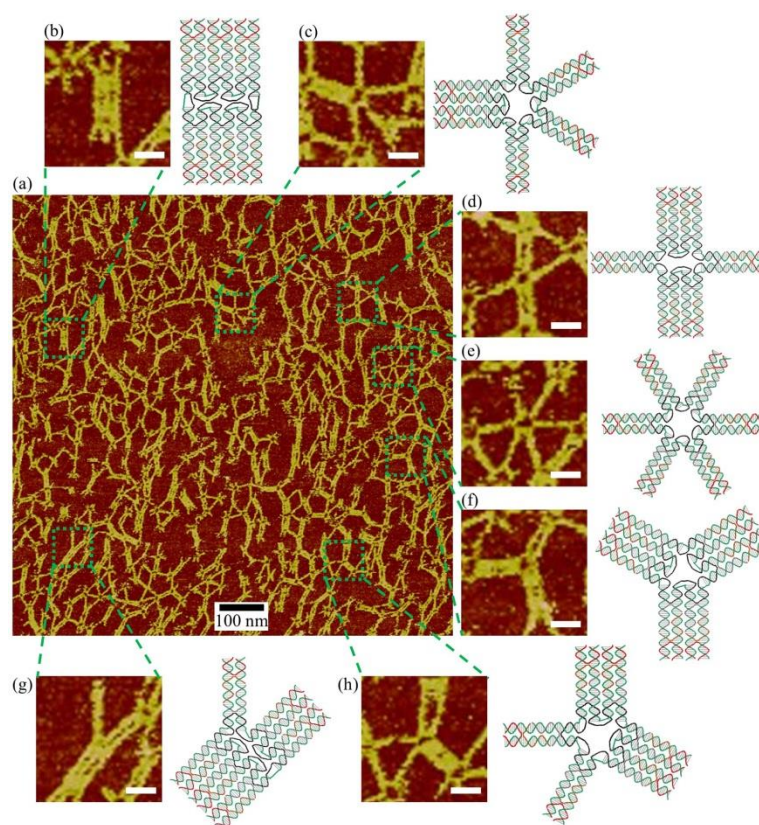
Figure 4.5. Deformation of 6PS motif. (a) AFM image of 2D networks assembled by 6PS. (b-h) Close-up views and corresponding structural schemes of different 6PS conformations. Scale bar: 20 nm.

In this design, the DNA motifs have several desired features: (1) Both DNA motifs have the same arm length, which meets the demand of identical distance between any two neighboring vertices of the quasicrystals; (2) Both DNA motifs share the same self-complementary sticky ends at each branch, which enables equal-probable and random association among b5PS and b6PS motifs; (3) With 3-nt spacers, motif b5PS has enough flexibility to allow the inter-branch angle to adapt either 60° or 90°, as demanded by dodecagonal quasicrystals; (4) Motif b6PS motif is purposely designed to be rigid by 1-nt spacers to maintain its 6-fold rotational symmetry; (5) DNA-

surface interaction will confine and stabilize the assembled DNA networks onto flat surfaces and prevent 3D aggregates formation.

4.3   Materials and Methods

4.3.1   DNA Oligonucleotides

All oligonucleotides were purchased from IDT, Inc. and purified by 6% - 20% denaturing PAGE. Oligonucleotides from b5PS, b6PS, 5PS, and 6PS motifs are listed below with their designated ratio and concentration during *in situ* assembly:

DNA Strands:

1:   5'-AGGCACCATCGTAGGTTTTCTTGCCAGGCACCATCGTAGGTTTTCTTGCC AGGCACCATCGTAGGTTTTCTTGCCAGGCACCATCGTAGGTTTTCTTGCCAGGCA CCATCGTAGGTTTTCTTGCC-3' (circular by ligation at 5' and 3' ends)

1*:   5'-AGGCACCATCGTAGGTTTTCTTGCCAGGCACCATCGTAGGTTTTCTTGCC AGGCACCATCGTAGGTTTTCTTGCCAGGCACCATCGTAGGTTTTCTTGCCAGGCA CCATCGTAGGTTTTCTTGCCAGGCACCATCGTAGGTTTTCTTGCC-3'   (circular   by ligation at 5' and 3' ends)

2:   5'-CCTATGCAACCTGATACCCTTAGTATGTAGCCTGCCTGGCAAGCCTACG ATGGACAATCTATTATGCGATTCGGACACGGTAAC-3'

3A: 5'-TATCACCGAATCGCATAATAGCGTCGAACG-3'

3A*: 5'-TATCACCGAATCGCATAATAG-3'

3B: 5'-ATTGTGGCTACATACTAAGGGCGTCGAACG-3'

3B*: 5'-ATTGTGGCTACATACTAAGGG-3'

4:   5'-GGTTACCGTGTGGTTGCATAG-3'

BB: 5'-GAAGCTTCCGTTCGT-3'

BB*: 5'-GAAGCTTCGTTCGAC-3'

DNA Motifs (motif concentration is 400 nM):

b5PS: **1**+**2**+**3A**+**3B**+**4**+ **BB** (1:5:5:5:5:10).

b6PS: **1***+**2**+**3A**+**3B**+**4**+ **BB*** (1:6:6:6:6:12).

5PS: **1**+**2**+**3A***+**3B***+**4** (1:5:5:5:5).

6PS: **1***+**2**+**3A***+**3B***+**4** (1:5:5:5:5).

4.3.2   Buffers

TA/Na buffer: 40 mM tris base, 20 mM acetic acid, and 500 mM sodium chloride; pH is adjusted to 8.0

TAE/Mg^{2+} buffer: 40 mM tris base, 20 mM acetic acid, 2 mM EDTA, and 12.5 mM magnesium acetate; pH is adjusted to 8.0

TA/Na/Mg^{2+} buffer: 40 mM tris base, 20 mM acetic acid, 20 mM magnesium acetate, and 500 mM sodium chloride; pH is adjusted to 8.0

TA/Mg^{2+}/Ni^{2+} buffer: 40 mM tris base, 20 mM acetic acid, 10 mM magnesium acetate, and 2 mM nickel chloride; pH is adjusted to 8.0

4.3.3   Preparation of Individual DNA Point-Star Motifs

For each point-star motif, mix ssDNAs (except bridge strands BB or BB*) at designated stoichiometric molar ratio in TA/Na solution to give final 40 μL 500 nM motif solution (no bridges). Sequentially incubate above solutions: 95 °C for 5 min, 65 °C for 30 min, 50 °C for 30 min, 37 °C for 30 min, and 22 °C for 30 min. For formation of motifs with bridges, add the bridge

DNA BB or BB$^{(*)}$ into the annealed solution above and stand for 1 hour at 22 °C to give final 50 uL 400 nM motif solution (with bridges).

4.3.4 Native PAGE

Mix 2 mL 40% acrylamide/bisacrylamide solution (19:1, 5% crosslinker), 2 mL 10× TAE/Mg^{2+} buffer, and 16 mL distilled water to prepare 4% native PAGE gel. The running buffer was TAE/Mg^{2+} buffer (containing 40 mM tris base, 20 mM acetic acid, 2 mM EDTA, and 12.5 mM magnesium acetate; pH is adjusted to 8.0). Gels were run on a FB-VE10-1 electrophoresis unit (FisherBiotech) at 4 °C (300V, constant voltage) for 2 hours. After electrophoresis, the gels were stained with Stains-all dye (Sigma) and scanned.

4.3.5 Surface Assembly Protocol

Our protocol includes four steps. (1) Preparation: Mix b5PS and b6PS motif at designated motif ratio to a final 200 nM DNA motif in TA/Na solution. (2) Surface assembly: Deposit 5 µL DNA solution onto a freshly cleaved mica surface and incubate for designated time (incubation time) at 22 °C for network formation. (3) Buffer wash: After surface assembly, 20 µL TA/Na/Mg^{2+} buffer is added onto mica surface and then removed. Repeat this process for four times (number of wash times can be different if mentioned otherwise). (4) AFM image capture: 20 µL TA/Mg^{2+}/Ni^{2+} buffer is added onto mica surface. Then AFM images are captured by MultiMode 8 (Bruker) using ScanAsyst-fluid mode with ScanAsyst-fluid+ probes (Bruker). The tip-surface interaction was automatically adjusted to optimize the scan set-point. All experiments are carried out at 22 °C.

Buffer washing in Step 3 is important. (*i*) Without wash, crowd of aggregates of individual DNA motifs on surface is observed. (*ii*) With single or two washes, surface is much cleaner with

a decreasing number of individual motifs. (*iii*) With four washes, satisfactory imaging condition is obtained with good network protection (Figure 4.6). Four washes between DNA incubation and AFM imaging are applied for all experiments.
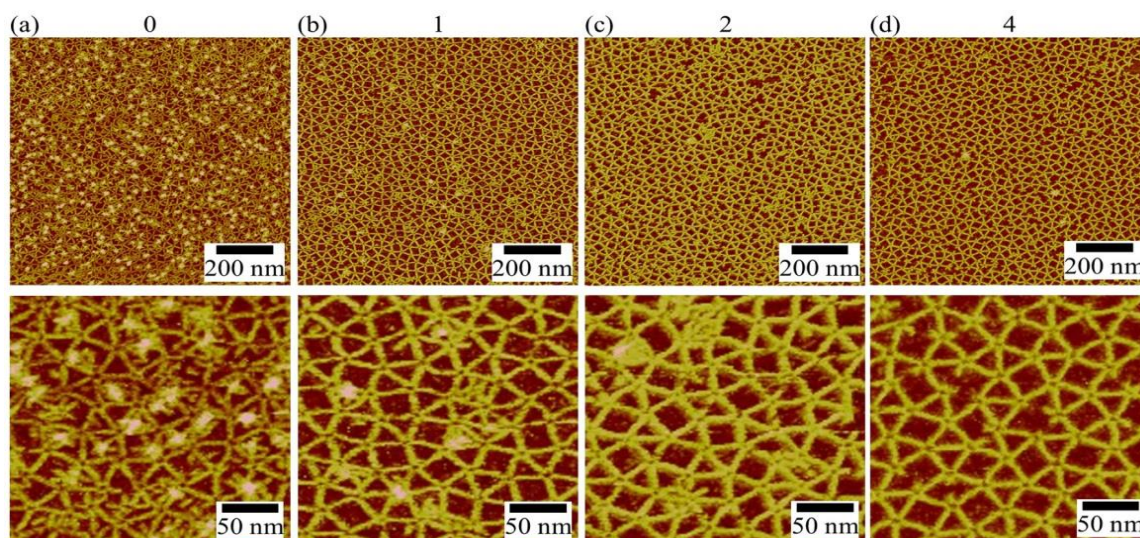
Figure 4.6. Influence of different washing times on the quality of AFM images. (a-d) A pair of AFM images (top panel: large-area images of the DNA networks; bottom panel: close-up views) of the DNA networks (incubation time: 30 min) assembled from b5PS motif after 0, 1, 2, and 4 times of buffer washing.

In Step 4, the introduction of 2 mM Ni^{2+} and and 10 mM Mg^{2+} effectively freezes the DNA structure at the specifically given time point, which is essential for time-course AFM imaging. Ni^{2+} is known to strongly bind and immobilize DNA structures on mica surface.[72,81] Mg^{2+} is for maintain the integrity of the DNA nanostructures.

4.3.6   FFT and Inverse FFT Processing

Import the original AFM images into ImageJ software.[92] Use FFT operation to obtain FFT diffraction patterns then followed by brightness-and-contrast adjustment. Pick up the targeted intense diffraction spots and use inverse FFT operation to render reconstructed images.

4.3.7   Exponential Fitting

Data is processed by Origin software developed by OriginLab Corporation. Choose exponential fitting to generate final reports.

4.4   Results and Discussion

4.4.1   Self-Assembly of DNA Motifs

DNA self-assembly was conducted in two steps according to a reported method.[77] (i) Assembly of individual DNA motifs separately in solution. All component strands were mixed at designated ratios in a Na^+-containing, neutral, aqueous buffer and thermally annealed to form individual motifs. (ii) Surface-assisted self-assembly of DNA crystals/quasicrystals from motifs. Pre-formed, individual DNA motifs were mixed at designated ratios and deposited onto mica surfaces. Isothermal incubation at 22 °C led to the assembly of large DNA 2D networks. After assembly, the formation of individual motifs was confirmed by native PAGE (Figure 4.7-4.9) and the assembled, large DNA networks were directly imaged by atomic force microscopy (AFM).
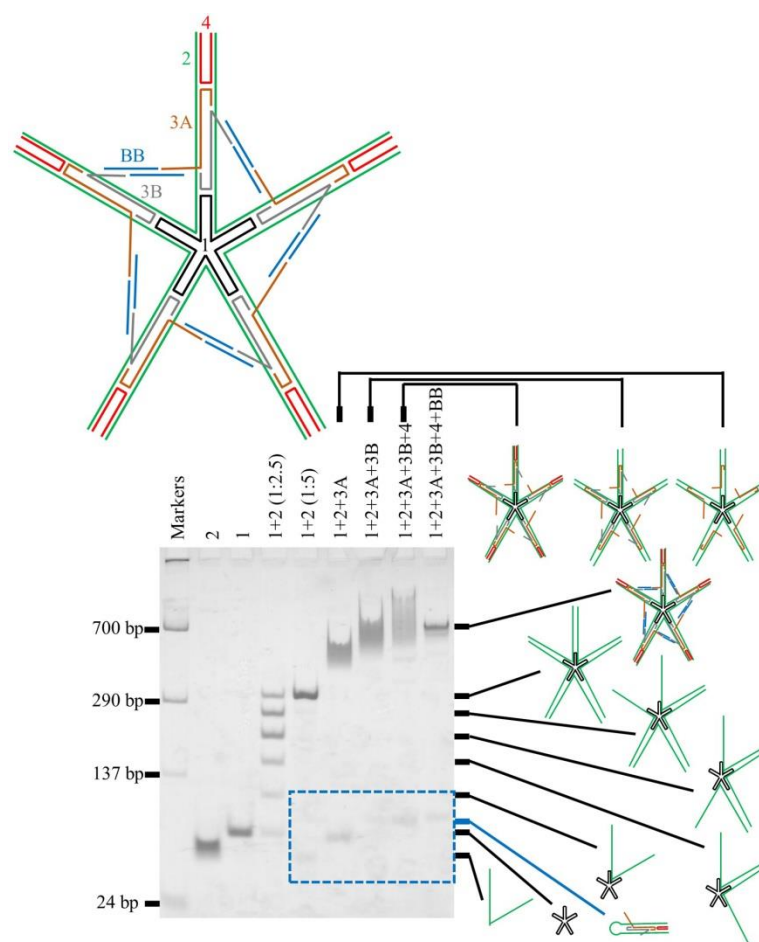
Figure 4.7. Native PAGE (4%) analysis of the individual b5PS motif (a structural scheme shown at the upper left). The sample compositions and the band identities are indicated above and beside the gel image, respectively. Strands 1, 2, 3A, 3B, 4, and BB are as shown in Figure S1d. Blue dashed box contains some byproduct bands which were caused by excessive 5% of 2, 3A and 3B and excessive 10% of 4 and BB to ensure structural integrity of b5PS motif. The smeared bands were attributed to inter- and/or intra-molecular interaction between single-stranded overhangs introduced by 3A and 3B in the partial complexes. The designed, full b5PS motif readily formed and appeared as a sharp, major band with an expected mobility in native PAGE.
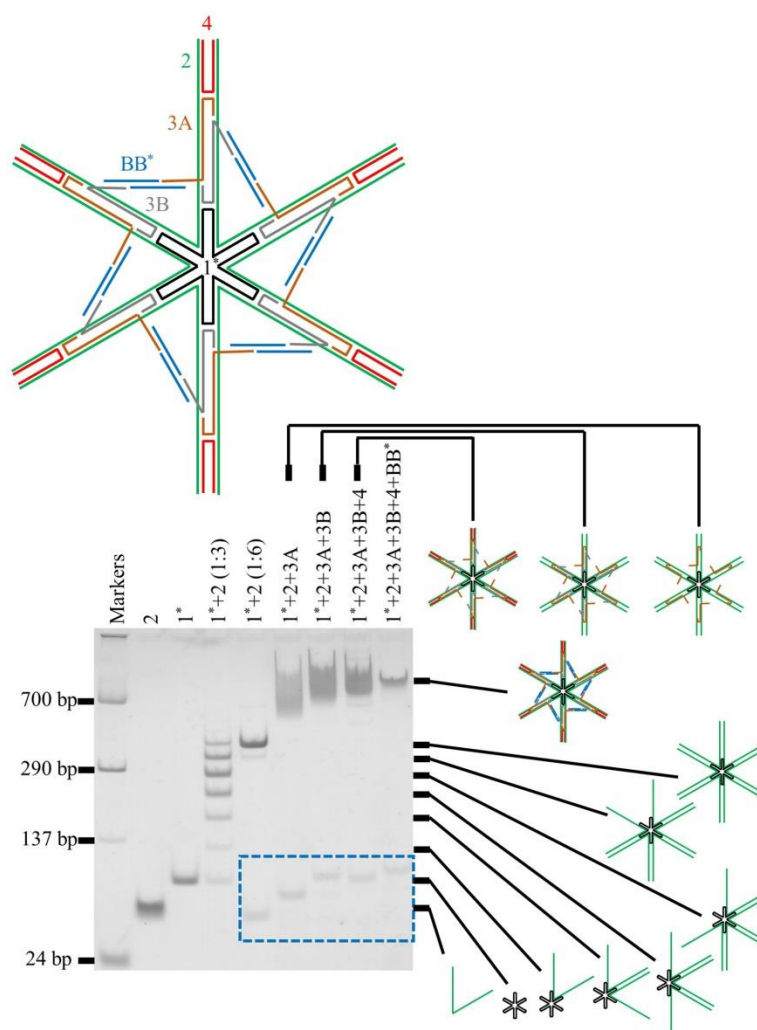
Figure 4.8. Native PAGE (4%) analysis of the individual b6PS motif (a structural scheme shown at the upper left). The sample compositions and the band identities are indicated above and beside the gel image, respectively. Strands 1*, 2, 3A, 3B, 4, and BB* are as shown in Figure S1e. Blue dashed box contains some byproduct bands which were caused by excessive 5% of 2, 3A and 3B and excessive 10% of 4 and BB* to ensure structural integrity of b6PS motif.
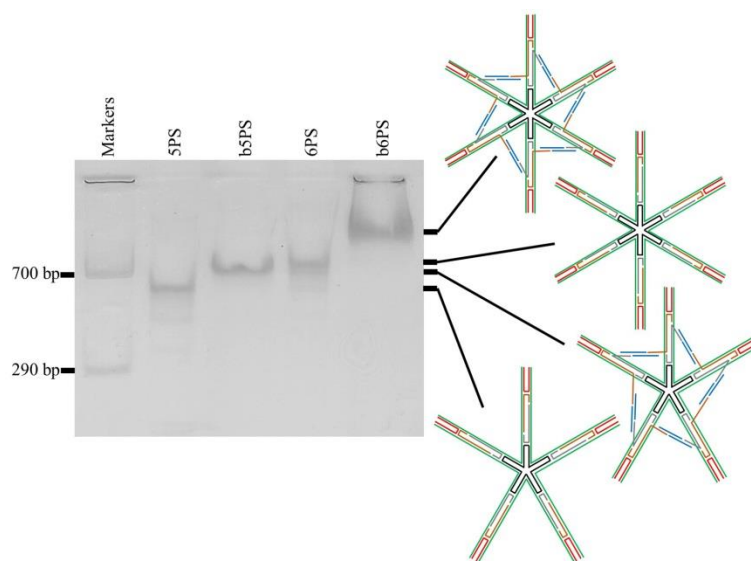
Figure 4.9. Comparison of the formation of motifs 5PS, b5PS, 6PS, and b6PS in native PAGE. The sample compositions and the band identities are indicated above and beside the gel image, respectively.

4.4.2   Formation of Crystalline and Quasicrystalline Networks

DNA 2D quasicrystals and/or crystals formed depending on the molar ratio of b5PS:b6PS in the solution (Figure 4.10). The resulting structures show clear FFT (fast Fourier transform) patterns, which allow ready analysis of the structure symmetries. All the (quasi)crystals consisted of only three types of vertices: **I** ($3^2 \cdot 4 \cdot 3 \cdot 4$), **II** ($3^3 \cdot 4^2$), and [**III** ($3^6$)]. When b5PS:b6PS = 100:0, only b5PS motif existed in the system. It took conformation **I** ($3^2 \cdot 4 \cdot 3 \cdot 4$) and assembled into tetragonal crystals (snub square tiling) as in previous study (Figure 4.10 a).[54] When small amount of b6PS motif was introduced into the system (b5PS:b6PS = 90:10, 80:20), dodecagonal quasicrystals formed, which contained both b5PS and b6PS motifs (Figure 4.10 b and c). When more b6PS motif was introduced (b5PS:b6PS = 70:30), hexagonal crystals (triangular tiling) appeared and mixtures of dodecagonal quasicrystals and hexagonal crystals were resulted (Figure 4.10 d). As b6PS motif content was further increased (b5PS:b6PS = 60:40), quasicrystals completely disappeared; only poly-domained, hexagonal crystals of b6PS motifs were assembled

(Figure 4.10 e). At the boundaries between two domains, some 5bPS motifs were observed, which probably hindered the formation of single hexagonal crystals. When b5PS:b6PS = 0:100, only b6PS existed in the system and assembled into large, hexagonal crystals as in previous study (Figure 4.10 f).[55] It extended to at least 4 µm x 4 µm and contained over 2.6 x 10^5 b6PS motifs.
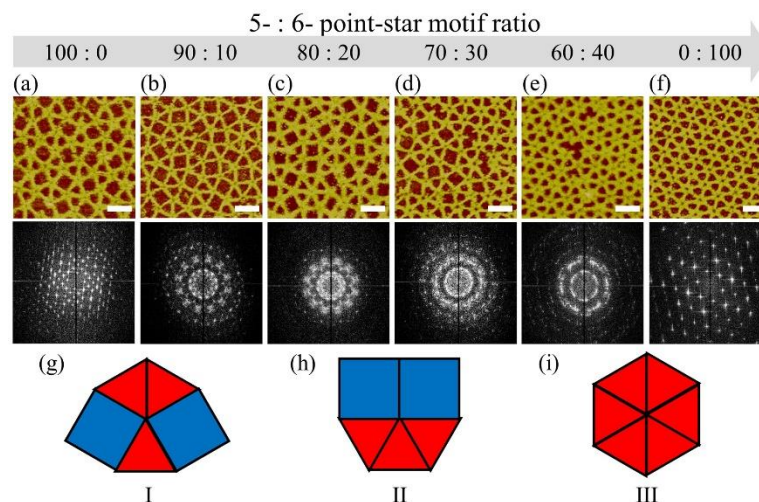
Figure 4.10. AFM study of binary networks assembled from motifs b5PS and b6PS. (a-f) AFM images (left panel) and corresponding FFT patterns (right panel) of DNA networks from DNA bulk solutions with indicated b5PS:b6PS ratios. FFT patterns are based on AFM images with area of 1 μm x 1 μm. Scale bar: 50 nm. (g-i) All vertex conformations found in these networks.

It is interesting that the composition of the DNA motifs in bulk solution and in the assembled networks on surface are related, but far away from being equal to each other. Presumably this phenomenon is a result of preferential crystal packing and differential motif adsorption to the surfaces. We have attributed this phenomenon to two factors. (i) The two motifs have different abilities to adsorb onto mica surface. The b6PS motif has larger surface area than b5PS, thus absorb onto mica surfaces more stable than b5PS. (ii) In the assembled networks, each b6PS interacts with rest of the networks by six branches, and b5PS only by five. Thus, the b6PS motif is more stable in the assembled networks than b5PS is.

4.4.3 Analysis of Quasicrystalline Networks

Fascinating dodecagonal quasicrystals were observed when b5PS and b6PS at motif ratios of 80:20 (Figure 4.11) and 90:10 (Figure 4.12) in bulk solution. The corresponding FFT patterns show distinct 12-fold symmetry. Figure 4.11 a illustrates an AFM image of the quasicrystals (b5PS:b6PS = 80:20). b5PS motifs adapt either configuration **I** ($3^2 \cdot 4 \cdot 3 \cdot 4$) or **II** ($3^3 \cdot 4^2$) and b6PS motifs take configuration **III** [(3^6)] as shown in black circles. Green circles highlight two dodecagonal motifs with 30° rotation relative to each other, confirming the important orientation requirement of dodecagonal tiling. In the FFT pattern, diffraction spots exist on five concentric rings: A, B, C, D, and E from the center to outside (Figure 4.11 c). On each ring, the diffraction spots follow a 12-fold symmetry, indicating a dodecagonal representation. Spots on circles A, B, C, D, and E are mutually vector-correlated as deduced in vector arrows. For example, diffraction spots in circle E can be derived from vector addition of two adjacent diffraction spots in circle B. The DNA quasicrystal is close to an infinite, perfect, dodecagonal quasicrystal. In a perfect dodecagonal quasicrystal, the triangle-to-square ratio is $4/\sqrt{3} = 2.31$.[126-128] In the observed AFM image, there are 695 triangles and 301 squares (Figure 4.11 b), resulting in a triangle-to-square ratio of 2.31, the same as the theoretical value. When concerning about the vertices in a perfect dodecagonal quasicrystal, the ratio between b5PS and b6PS should be ~ 12.9. Our experimentally observed ratio is 13.6 [b5PS (598): b6PS (44)], closely matching to the theoretical value. Furthermore, the defect-free quasicrystal lattice accounts for 97.0% of the observed area. Edge-tiling map indicates a near-even distribution of the six, possible edge orientations (an edge is defined by the line connecting two adjacent vertices), which corresponds to the 12-fold symmetry in the FFT pattern (Figure 4.11 d and e).[22] All the evidences indicate that this network is a near-perfect dodecagonal quasicrystal.
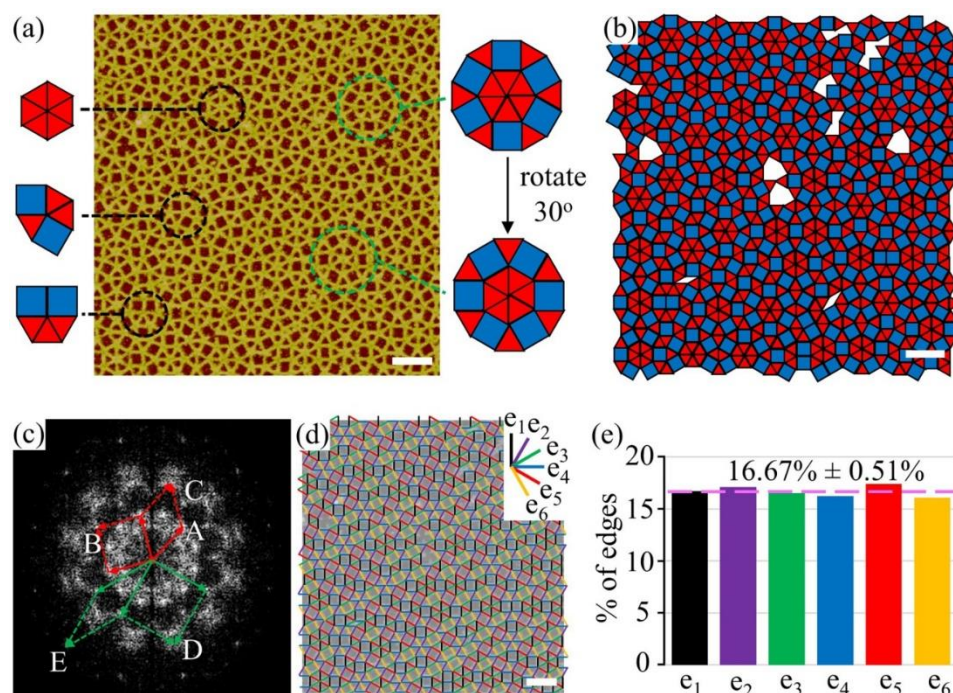
Figure 4.11. Analysis of dodecagonal quasicrystalline networks assembled from b5PS and b6PS motifs at a ratio of 80:20 in bulk solution. (a) An AFM image of the dodecagonal quasicrystals. Three vertex configurations (corresponding to individual DNA motifs) are highlighted on the left side, and two dodecagonal complex motifs with 30° relative rotation are highlighted on the right side. (b) Triangle-and-square tiling map of (a). (c) The FFT pattern of (a). Five concentric rings (A-E) of diffraction spots are related with each other by vector additions. Spots on each ring exhibit a 12-fold symmetry. (d) The edges in tiling map of (a) are distributed in six, color-coded orientations (e_1-e_6). (e) Statistics of the edge orientations. The pink, dashed line indicates the average edge percentage. Scale bar: 100 nm.

The quasicrystalline networks assembled at motif ratio of 90:10 also express dodecagonal tiling (Figure 4.12 a). The calculated triangle-to-square ratio is 2.28 (688 triangles and 302 squares, Figure 4.12 b), close to the theoretical value 2.31. The b5PS:b6PS in observed networks is 17.4 (608 b5PS motifs and 35 b6PS motifs), deviating from the theoretical value (12.9) of an infinite, defect-free dodecagonal quasicrystal. Considering the calculated triangle-to-square ratio of 2.28, this quasicrystal should have b5PS:b6PS of 14.3, which is also smaller than the observed 17.4. It is reasonable because of the low content of b6PS motif in bulk solution compared with that at the motif ratio of 80:20 discussed above, which is also demonstrated by some observed incomplete b6PS motifs (not counted in b5PS:b6PS calculation) in the network. The FFT pattern shows a 12-

fold symmetry (Figure 4.12 c), which is also supported by near-even distribution of the edge orientation (Figure 4.12 d and e). Furthermore, the defect-free area accounts for 96.8% of the imaged area. Overall, this network is a less perfect type of dodecagonal quasicrystal.
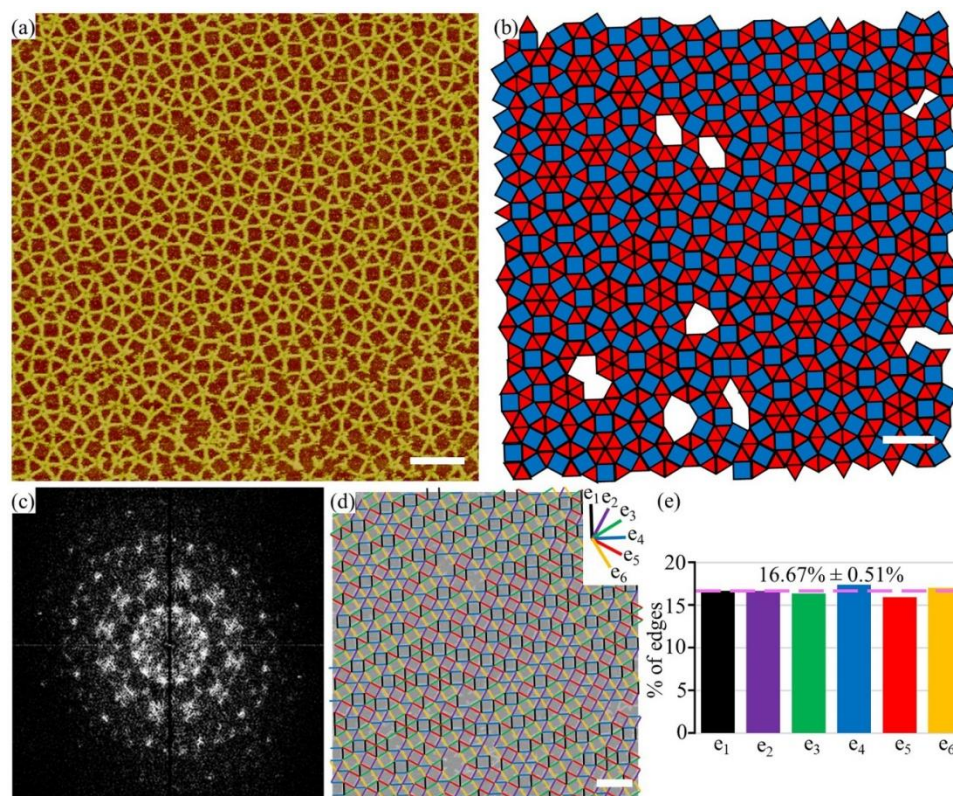
Figure 4.12. Analysis of dodecagonal quasicrystalline networks assembled from b5PS and b6PS motifs at a ratio of 80:20 in bulk solution. (a) An AFM image of the dodecagonal quasicrystals. Three vertex configurations (corresponding to individual DNA motifs) are highlighted on the left side, and two dodecagonal complex motifs with 30° relative rotation are highlighted on the right side. (b) Triangle-and-square tiling map of (a). (c) The FFT pattern of (a). Five concentric rings (A-E) of diffraction spots are related with each other by vector additions. Spots on each ring exhibit a 12-fold symmetry. (d) The edges in tiling map of (a) are distributed in six, color-coded orientations (e_1-e_6). (e) Statistics of the edge orientations. The pink, dashed line indicates the average edge percentage. Scale bar: 100 nm.

4.4.4   Deformation of DNA Motifs

In the DNA quasicrystals, some interesting motif deformations have been observed. In the quasicrystals at the motif ratio of 80:20, some b6PS motifs behave like b5PS motifs (Figure 4.13 a), likely because of the excessive b6PS motifs in bulk solution. In this deformed motif, one bridge

is broken, thus its flanking two branches are arranged in parallel and function as a single branch when associating with another motif. In contrast, in the quasicrystals at the motif ratio of 90:10, some b5PS motifs act like b6PS motifs (named pseudo-b6PS motifs, Figure 4.13 b), likely due to the insufficient b6PS motif in bulk solution. In the pseudo-b6PS motif, one bridge tears and the angle between the two adjacent branches turns into 120°. The other four angles are adjusted to 60°. This phenomenon demonstrates that the DNA motifs can, to certain degree, "smartly" tune their shapes according to the environment.
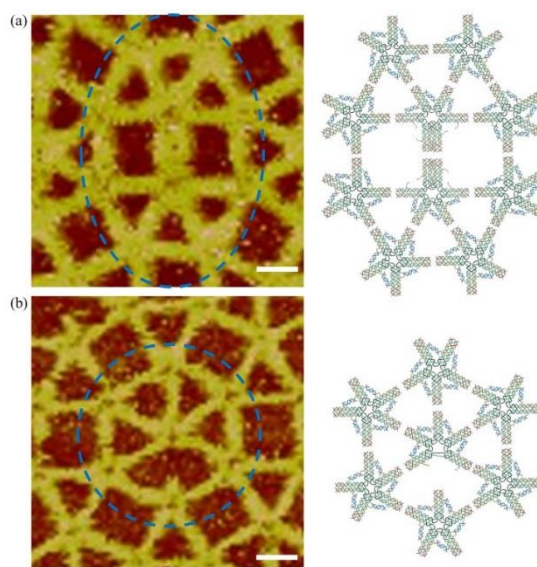
Figure 4.13. Two unusual conformations of DNA nanomotifs in DNA quasicrystalline networks. (a) A pair of elongated-triangular motifs assembled by degenerated d6PS motif: an AFM image (left) and its corresponding schematic representation (right). Assembly condition: b5PS:b6PS = 80:20 in bulk solution. . This phenomenon indicates existence of excessive b6PS motifs in bulk solution. (b) A pseudo-b6PS motif by deforming a b5PS motif: an AFM image (left) and its corresponding schematic representation (right). Assembly condition: b5PS: b6PS = 90:10 in bulk solution. This phenomenon indicates insufficiency of b6PS motifs in bulk solution. Scale bar: 20 nm.

4.5   Conclusion

This work has developed a rational approach to assemble 2D dodecagonal quasicrystals out of two nanomotifs. By tuning motif ratio in bulk solution, it is feasible to achieve a specific DNA

network including: snub square tiling, dodecagonal tiling, poly-grain crystals of triangular tiling, and single crystal of triangular tiling. The general approach has been proposed years ago,[129,130] but this is the first time to be experimentally demonstrated. The key of this study is the ability to fine tune the rigidity/flexibility balance of the DNA motifs. If too flexible, the DNA motifs will aggregate into random networks. If too rigid, the same motif cannot adapt different conformations needed for quasicrystals. This overall approach would be expected to be applicable to other systems for designing quasicrystals. In addition, DNA quasicrystals could allow further applications, *e.g.* organization of biomolecules or nanoparticles to express their own quasicrystallinity for functional exploration.

REFERENCES

1.   Wikipedia (https://en.wikipedia.org/wiki/DNA).

2.   Seeman, N. C. *Journal of Theoretical Biology* **1982**, *99*, 237.

3.   Kallenbach, N. R.; Ma, R.-I.; Seeman, N. C. *Nature* **1983**, *305*, 829.

4.   Seeman, N. C.; Kallenbach, N. R. *Biophysical Journal* **1983**, *44*, 201.

5.   Seeman. N. C. *Structural DNA Nanotechnology*. Cambridge University Press: Cambridge, U.K. (2016).

6.   Lin, C.; Liu, Y.; Yan, H. *Biochemistry* **2009**, *48*, 1663.

7.   Aldaye, F. A.; Palmer, A. L.; Sleiman, H. F. *Science* **2008**, *321*, 1795.

8.   Evans, C. G.; Winfree, E. *Chemical Society Reviews* **2017**, *46*, 3808.

9.   Jones, M. R.; Seeman, N. C.; Mirkin, C. A. *Science* **2015**, *347*.

10.   Chen, J.; Seeman, N. C. *Nature* **1991**, *350*, 631.

11.   Winfree, E.; Liu, F.; Wenzler, L. A.; Seeman, N. C. *Nature* **1998**, *394*, 539.

12.   Shih, W. M.; Quispe, J. D.; Joyce, G. F. *Nature* **2004**, *427*, 618.

13.   Rothemund, P. W. K. *Nature* **2006**, *440*, 297.

14.   Wei, B.; Dai, M.; Yin, P. *Nature* **2012**, *485*, 623.

15.   Seeman, N. C.; Sleiman, H. F. *Nature Reviews Materials* **2017**, *3*, 17068.

16.   Alivisatos, A. P.; Johnsson, K. P.; Peng, X.; Wilson, T. E.; Loweth, C. J.; Bruchez, M. P.; Schultz, P. G. *Nature* **1996**, *382*, 609.

17.   Mirkin, C. A.; Letsinger, R. L.; Mucic, R. C.; Storhoff, J. J. *Nature* **1996**, *382*, 607.

18.   Zheng, J.; Constantinou, P. E.; Micheel, C.; Alivisatos, A. P.; Kiehl, R. A.; Seeman, N. C. *Nano Letters* **2006**, *6*, 1502.

19.   Aldaye, F. A.; Sleiman, H. F. *Journal of the American Chemical Society* **2007**, *129*, 4130.

20.   Mastroianni, A. J.; Claridge, S. A.; Alivisatos, A. P. *Journal of the American Chemical Society* **2009**, *131*, 8455.

21.   Sharma, J.; Chhabra, R.; Cheng, A.; Brownell, J.; Liu, Y.; Yan, H. *Science* **2009**, *323*, 112.

22.   Udomprasert, A.; Bongiovanni, M. N.; Sha, R.; Sherman, W. B.; Wang, T.; Arora, P. S.; Canary, J. W.; Gras, S. L.; Seeman, N. C. *Nature Nanotechnology* **2014**, *9*, 537.

23.   Selmi, D. N.; Adamson, R. J.; Attrill, H.; Goddard, A. D.; Gilbert, R. J. C.; Watts, A.; Turberfield, A. J. *Nano Letters* **2011**, *11*, 657.

24.   Erben, C. M.; Goodman, R. P.; Turberfield, A. J. *Angewandte Chemie International Edition* **2006**, *45*, 7414.

25.   Wilner, O. I.; Weizmann, Y.; Gill, R.; Lioubashevski, O.; Freeman, R.; Willner, I. *Nature Nanotechnology* **2009**, *4*, 249.

26.   Fu, J.; Yang, Y. R.; Johnson-Buck, A.; Liu, M.; Liu, Y.; Walter, N. G.; Woodbury, N. W.; Yan, H. *Nature Nanotechnology* **2014**, *9*, 531.

27.   Derr, N. D.; Goodman, B. S.; Jungmann, R.; Leschziner, A. E.; Shih, W. M.; Reck-Peterson, S. L. *Science* **2012**, *338*, 662.

28.   Jungmann, R.; Avendaño, M. S.; Woehrstein, J. B.; Dai, M.; Shih, W. M.; Yin, P. *Nature Methods* **2014**, *11*, 313.

29.   Lin, C.; Jungmann, R.; Leifer, A. M.; Li, C.; Levner, D.; Church, G. M.; Shih, W. M.; Yin, P. *Nature Chemistry* **2012**, *4*, 832.

30.   Suzuki, Y.; Endo, M.; Katsuda, Y.; Ou, K.; Hidaka, K.; Sugiyama, H. *Journal of the American Chemical Society* **2014**, *136*, 211.

31.   Endo, M.; Xing, X.; Zhou, X.; Emura, T.; Hidaka, K.; Tuesuwan, B.; Sugiyama, H. *ACS Nano* **2015**, *9*, 9922.

32.   Modi, S.; Nizak, C.; Surana, S.; Halder, S.; Krishnan, Y. *Nature Nanotechnology* **2013**, *8*, 459.

33.   Tibbitt, M. W.; Dahlman, J. E.; Langer, R. *Journal of the American Chemical Society* **2016**, *138*, 704.

34.   Williford, J.-M.; Santos, J. L.; Shyam, R.; Mao, H.-Q. *Biomaterials Science* **2015**, *3*, 894.

35.   Liang, L.; Li, J.; Li, Q.; Huang, Q.; Shi, J.; Yan, H.; Fan, C. *Angewandte Chemie International Edition* **2014**, *53*, 7745.

36.   Watson, J. D.; Crick, F. H. C. *Nature* **1953**, *171*, 737.

37.   Wikipedia (https://en.wikipedia.org/wiki/Base_pair).

38.   Wikipedia (https://en.wikipedia.org/wiki/A-DNA).

39.   Seeman, N. C. *Annual Review of Biochemistry* **2010**, *79*, 65.

40.   Williams, S., Lund, K., Lin, C., Wonka, P., Lindsay, S., and Yan, H. (2008) Tiamat: A three-dimensional editing tool for complex DNA structures, The 14th International Meeting on DNA Computing, Prague, Czech Republic.

41.   Fu, T. J.; Seeman, N. C. *Biochemistry* **1993**, *32*, 3211.

42.   LaBean, T. H.; Yan, H.; Kopatsch, J.; Liu, F.; Winfree, E.; Reif, J. H.; Seeman, N. C. *Journal of the American Chemical Society* **2000**, *122*, 1848.

43.   Yan, H.; Park, S. H.; Finkelstein, G.; Reif, J. H.; LaBean, T. H. *Science* **2003**, *301*, 1882.

44.   Ding, B.; Sha, R.; Seeman, N. C. *Journal of the American Chemical Society* **2004**, *126*, 10230.

45.   Park, S. H.; Barish, R.; Li, H.; Reif, J. H.; Finkelstein, G.; Yan, H.; LaBean, T. H. *Nano Letters* **2005**, *5*, 693.

46.   Wei, B.; Mi, Y. *Biomacromolecules* **2005**, *6*, 2528.

47.   Mathieu, F.; Liao, S.; Kopatsch, J.; Wang, T.; Mao, C.; Seeman, N. C. *Nano Letters* **2005**, *5*, 661.

48.   Ke, Y.; Liu, Y.; Zhang, J.; Yan, H. *Journal of the American Chemical Society* **2006**, *128*, 4414.

49.   Reishus, D.; Shaw, B.; Brun, Y.; Chelyapov, N.; Adleman, L. *Journal of the American Chemical Society* **2005**, *127*, 17590.

50.   Liu, D.; Wang, M.; Deng, Z.; Walulu, R.; Mao, C. *Journal of the American Chemical Society* **2004**, *126*, 2324.

51.   Mao, C.; Sun, W.; Seeman, N. C. *Journal of the American Chemical Society* **1999**, *121*, 5437.

52.   He, Y.; Chen, Y.; Liu, H.; Ribbe, A. E.; Mao, C. *Journal of the American Chemical Society* **2005**, *127*, 12202.

53.   He, Y.; Tian, Y.; Chen, Y.; Deng, Z.; Ribbe, A. E.; Mao, C. *Angewandte Chemie* **2005**, *117*, 6852.

54.   Zhang, C.; Su, M.; He, Y.; Zhao, X.; Fang, P.-a.; Ribbe, A. E.; Jiang, W.; Mao, C. *Proceedings of the National Academy of Sciences* **2008**, *105*, 10665.

55. He, Y.; Tian, Y.; Ribbe, A. E.; Mao, C. *Journal of the American Chemical Society* **2006**, *128*, 15978.

56. Chen, J.; Seeman, N. C. *Nature* **1991**, *350*, 631.

57. Zhang, Y.; Seeman, N. C. *Journal of the American Chemical Society* **1994**, *116*, 1661.

58. Goodman, R. P.; Schaap, I. A. T.; Tardin, C. F.; Erben, C. M.; Berry, R. M.; Schmidt, C. F.; Turberfield, A. J. *Science* **2005**, *310*, 1661.

59. Erben, C. M.; Goodman, R. P.; Turberfield, A. J. *Journal of the American Chemical Society* **2007**, *129*, 6992.

60. Aldaye, F. A.; Sleiman, H. F. *Journal of the American Chemical Society* **2007**, *129*, 13376.

61. He, Y.; Ye, T.; Su, M.; Zhang, C.; Ribbe, A. E.; Jiang, W.; Mao, C. *Nature* **2008**, *452*, 198.

62. He, Y.; Su, M.; Fang, P.-a.; Zhang, C.; Ribbe, A. E.; Jiang, W.; Mao, C. *Angewandte Chemie International Edition* **2010**, *49*, 748.

63. Zhang, C.; Ko, S. H.; Su, M.; Leng, Y.; Ribbe, A. E.; Jiang, W.; Mao, C. *Journal of the American Chemical Society* **2009**, *131*, 1413.

64. Zhang, C.; Wu, W.; Li, X.; Tian, C.; Qian, H.; Wang, G.; Jiang, W.; Mao, C. *Angewandte Chemie International Edition* **2012**, *51*, 7999.

65. Douglas, S. M.; Dietz, H.; Liedl, T.; Högberg, B.; Graf, F.; Shih, W. M. *Nature* **2009**, *459*, 414.

66. Dietz, H.; Douglas, S. M.; Shih, W. M. *Science* **2009**, *325*, 725.

67. Benson, E.; Mohammed, A.; Gardell, J.; Masich, S.; Czeizler, E.; Orponen, P.; Högberg, B. *Nature* **2015**, *523*, 441.

68. Zheng, J.; Birktoft, J. J.; Chen, Y.; Wang, T.; Sha, R.; Constantinou, P. E.; Ginell, S. L.; Mao, C.; Seeman, N. C. *Nature* **2009**, *461*, 74.

69. Protozanova, E.; Frank-Kamenetskii, M. D.; Yakovchuk, P. *Nucleic Acids Research* **2006**, *34*, 564.

70. Kilchherr, F.; Wachauf, C.; Pelz, B.; Rief, M.; Zacharias, M.; Dietz, H. *Science* **2016**, *353*, aaf5508.

71. Gerling, T.; Wagenbauer, K. F.; Neuner, A. M.; Dietz, H. *Science* **2015**, *347*, 1446.

72. Woo, S.; Rothemund, P. W. K. *Nat Commun* **2014**, *5*.

73.   Tikhomirov, G.; Petersen, P.; Qian, L. *Nature Nanotechnology* **2016**, *12*, 251.

74.   Suzuki, Y.; Sugiyama, H.; Endo, M. *Angewandte Chemie International Edition* **2018**, *57*, 7061.

75.   Wang, R.; Kuzuya, A.; Liu, W.; Seeman, N. C. *Chemical Communications* **2010**, *46*, 4905.

76.   Avakyan, N.; Conway, J. W.; Sleiman, H. F. *Journal of the American Chemical Society* **2017**, *139*, 12027.

77.   Liu, L.; Li, Y.; Wang, Y.; Zheng, J.; Mao, C. *ChemBioChem* **2017**, *18*, 2404.

78.   Bashar, S.; Lee, C.-W.; Lee, J.; Kim, B.; Gnapareddy, B.; Shin, J.; Dugasani, S. R.; Park, S. H. *RSC Advances* **2013**, *3*, 19876.

79.   Sun, X.; Hyeon Ko, S.; Zhang, C.; Ribbe, A. E.; Mao, C. *Journal of the American Chemical Society* **2009**, *131*, 13248.

80.   Hamada, S.; Murata, S. *Angewandte Chemie International Edition* **2009**, *48*, 6820.

81.   Bezanilla, M.; Drake, B.; Nudler, E.; Kashlev, M.; Hansma, P. K.; Hansma, H. G. *Biophysical Journal* **1994**, *67*, 2454.

82.   Hart, J. R. in *Ullmann's Encyclopedia of Industrial Chemistry* (Wiley-VCH Verlag GmbH & Co. KGaA, 2000).

83.   Li, M.; Yu, J.; Li, J.; Wang, E. B.; Wang, G.; Mao, C. *RSC Advances* **2016**, *6*, 76355.

84.   Zhang, G.; Surwade, S. P.; Zhou, F.; Liu, H. *Chemical Society Reviews* **2013**, *42*, 2488.

85.   Deng, Z.; Mao, C. *Angewandte Chemie International Edition* **2004**, *43*, 4068.

86.   Surwade, S. P.; Zhao, S.; Liu, H. *Journal of the American Chemical Society* **2011**, *133*, 11868.

87.   Wang, H.; Levin, C. S.; Halas, N. J. *Journal of the American Chemical Society* **2005**, *127*, 14992.

88.   Mrksich, M.; Whitesides, G. M. *Annual Review of Biophysics and Biomolecular Structure* **1996**, *25*, 55.

89.   Veiseh, M.; Zareie, M. H.; Zhang, M. *Langmuir* **2002**, *18*, 6671.

90.   Ganesan, R.; Kratz, K.; Lendlein, A. *Journal of Materials Chemistry* **2010**, *20*, 7322.

91.	Li, X.; Zhang, C.; Hao, C.; Tian, C.; Wang, G.; Mao, C. *ACS Nano* **2012**, *6*, 5138.

92.	Rasband, W.S., ImageJ, U. S. National Institutes of Health, Bethesda, Maryland, USA, https://imagej.nih.gov/ij/ (1997-2018).

93.	Daniel, M.-C.; Astruc, D. *Chemical Reviews* **2004**, *104*, 293.

94.	He, L.; Musick, M. D.; Nicewarner, S. R.; Salinas, F. G.; Benkovic, S. J.; Natan, M. J.; Keating, C. D. *Journal of the American Chemical Society* **2000**, *122*, 9071.

95.	Kuzyk, A.; Schreiber, R.; Fan, Z.; Pardatscher, G.; Roller, E.-M.; Hogele, A.; Simmel, F. C.; Govorov, A. O.; Liedl, T. *Nature* **2012**, *483*, 311.

96.	Chou, L. Y. T.; Zagorovsky, K.; Chan, W. C. W. *Nat Nano* **2014**, *9*, 148.

97.	Schreiber, R.; Santiago, I.; Ardavan, A.; Turberfield, A. J. *ACS Nano* **2016**, *10*, 7303.

98.	Macfarlane, R. J.; Lee, B.; Jones, M. R.; Harris, N.; Schatz, G. C.; Mirkin, C. A. *Science* **2011**, *334*, 204.

99.	Nykypanchuk, D.; Maye, M. M.; van der Lelie, D.; Gang, O. *Nature* **2008**, *451*, 549.

100.	Li, Y.; Liu, Z.; Yu, G.; Jiang, W.; Mao, C. *Journal of the American Chemical Society* **2015**, *137*, 4320.

101.	Edwardson, T. G. W.; Lau, K. L.; Bousmail, D.; Serpell, C. J.; Sleiman, H. F. *Nat Chem* **2016**, *8*, 162.

102.	Ohta, S.; Glancy, D.; Chan, W. C. W. *Science* **2016**, *351*, 841.

103.	Zhang, J.; Liu, Y.; Ke, Y.; Yan, H. *Nano Letters* **2006**, *6*, 248.

104.	Pinto, Y. Y.; Le, J. D.; Seeman, N. C.; Musier-Forsyth, K.; Taton, T. A.; Kiehl, R. A. *Nano Letters* **2005**, *5*, 2399.

105.	Cheng, W.; Campolongo, M. J.; Cha, J. J.; Tan, S. J.; Umbach, C. C.; Muller, D. A.; Luo, D. *Nat Mater* **2009**, *8*, 519.

106.	He, Y.; Ye, T.; Ribbe, A. E.; Mao, C. *Journal of the American Chemical Society* **2011**, *133*, 1742.

107.	Aghebat Rafat, A.; Pirzer, T.; Scheible, M. B.; Kostina, A.; Simmel, F. C. *Angewandte Chemie International Edition* **2014**, *53*, 7665.

108.	Suzuki, Y.; Endo, M.; Sugiyama, H. **2015**, *6*, 8052.

109. He, Y.; Tian, Y.; Ribbe, A. E.; Mao, C. *Journal of the American Chemical Society* **2006**, *128*, 12664.

110. Ramakrishnan, S.; Subramaniam, S.; Stewart, A. F.; Grundmeier, G.; Keller, A. *ACS Applied Materials & Interfaces* **2016**, *8*, 31239.

111. Beeley, J. A.; Stevenson, S. M.; Beeley, J. G. *Biochimica et Biophysica Acta (BBA) - Protein Structure* **1972**, *285*, 293.

112. Nisbet, A. D.; Saundry, R. H.; Moir, A. J. G.; Fothergill, L. A.; Fothergill, J. E. *European Journal of Biochemistry* **1981**, *115*, 335.

113. Wetter, L. R.; Deutsch, H. F. *Journal of Biological Chemistry* **1951**, *192*, 237.

114. Canfield, R. E. *Journal of Biological Chemistry* **1963**, *238*, 2698.

115. Liu, X.; Zhang, F.; Jing, X.; Pan, M.; Liu, P.; Li, W.; Zhu, B.; Li, J.; Chen, H.; Wang, L.; Lin, J.; Liu, Y.; Zhao, D.; Yan, H.; Fan, C. *Nature* **2018**, *559*, 593.

116. Nguyen, L.; Döblinger, M.; Liedl, T.; Heuer-Jungemann, A. *Angewandte Chemie International Edition* **2019**, *58*, 912.

117. Shechtman, D.; Blech, I.; Gratias, D.; Cahn, J. W. *Physical Review Letters* **1984**, *53*, 1951.

118. Ye, X.; Chen, J.; Eric Irrgang, M.; Engel, M.; Dong, A.; Glotzer, Sharon C.; Murray, C. B. *Nature Materials* **2016**, *16*, 214.

119. Paßens, M.; Caciuc, V.; Atodiresei, N.; Feuerbacher, M.; Moors, M.; Dunin-Borkowski, R. E.; Blügel, S.; Waser, R.; Karthäuser, S. *Nature Communications* **2017**, *8*, 15367.

120. Xiao, C.; Fujita, N.; Miyasaka, K.; Sakamoto, Y.; Terasaki, O. *Nature* **2012**, *487*, 349.

121. Wasio, N. A.; Quardokus, R. C.; Forrest, R. P.; Lent, C. S.; Corcelli, S. A.; Christie, J. A.; Henderson, K. W.; Kandel, S. A. *Nature* **2014**, *507*, 86.

122. Urgel, J. I.; Écija, D.; Lyu, G.; Zhang, R.; Palma, C.-A.; Auwärter, W.; Lin, N.; Barth, J. V. *Nature Chemistry* **2016**, *8*, 657.

123. Penrose, R. *The Mathematical Intelligencer* **1979**, *2*, 32.

124. Stampfli, P. *Helvetica Physica Acta* **1986**, *59*, 1260.

125. Zhou, Z.; Harris, K. D. M. *ChemPhysChem* **2006**, *7*, 1649.

126. Leung; Henley; Chester *Physical review. B, Condensed matter* **1989**, *39*, 446.

127.   Kawamura, H. *Progress of Theoretical Physics* **1983**, *70*, 352.

128.   Oxborrow, M.; Henley, C. L. *Physical Review B* **1993**, *48*, 6966.

129.   van der Linden, M. N.; Doye, J. P. K.; Louis, A. A. *The Journal of Chemical Physics* **2012**, *136*, 054904.

130.   Aleks, R.; John, S. S.; Flavio, R.; Jonathan, P. K. D. *Journal of Physics: Condensed Matter* **2017**, *29*, 014006.

PUBLICATIONS

1. Liu, L.; Li, Y.; Wang, Y.; Zheng, J.; Mao, C. *ChemBioChem* **2017**, *18*, 2404.

2. Liu, L.; Zheng, M.; Li, Z.; Li, Q.; Mao, C. *ACS Applied Materials & Interfaces* **2019**.

3. Liu, L.; Li, Z.; Li, Y.; Mao, C. *Journal of the American Chemical Society* **2019**.
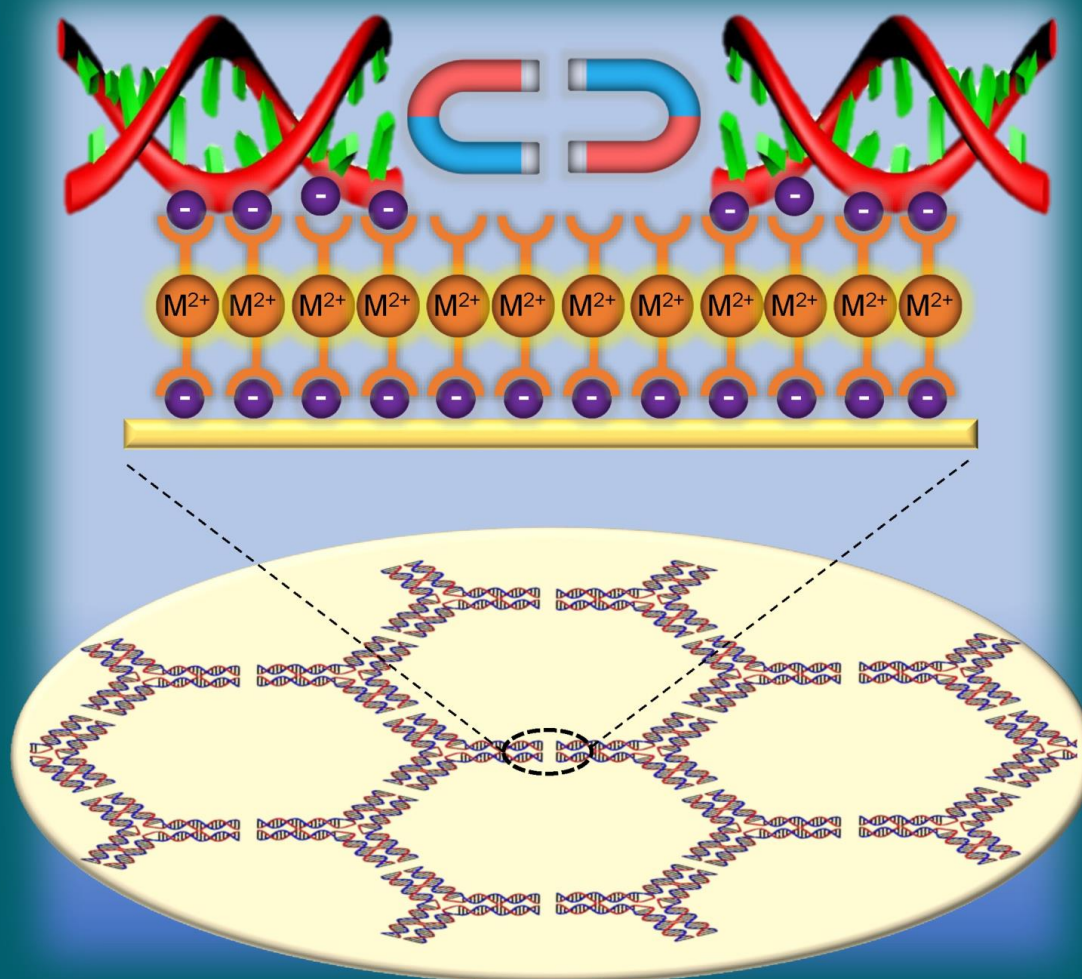
24/2017

Cover Feature:
J. Zheng, C. Mao et al.
Regulating DNA Self-assembly by DNA–Surface Interactions

A Journal of

ChemPubSoc
Europe

WILEY-VCH   www.chembiochem.org

Regulating DNA Self-assembly by DNA–Surface Interactions

Longfei Liu,[a] Yulin Li,[b] Yong Wang,[a, c] Jianwei Zheng,*[d] and Chengde Mao*[a]

DNA self-assembly provides a powerful approach for preparation of nanostructures. It is often studied in bulk solution and involves only DNA–DNA interactions. When confined to surfaces, DNA–surface interactions become an additional, important factor to DNA self-assembly. However, the way in which DNA–surface interactions influence DNA self-assembly is not well studied. In this study, we showed that weak DNA–DNA interactions could be stabilized by DNA–surface interactions to allow large DNA nanostructures to form. In addition, the assembly can be conducted isothermally at room temperature in as little as 5 seconds.

This communication reports a comprehensive study on regulating weak force-dependent DNA self-assembly on surfaces. In this study, DNA self-assembly is driven by one or two pairs of blunt-end stacking. Such a weak interaction cannot hold DNA motifs (tiles) together by itself. However, this weak interaction can be further stabilized by DNA–surface interactions to allow DNA tiles to assemble into large nanostructures. The surface stabilization can be conveniently tuned by changing the concentration of Ni^{2+}, which forms a salt bridge between DNA and the mica surface.

DNA has been exploited to construct various DNA nanostructures over the last three decades.[1–11] Most of them are constructed in free solution, and very few studies have been devoted to assembly on solid surfaces. Recently, DNA assembly on surfaces has been studied because it offers many potential advantages.[12–18] For example, DNA nanomotifs have reduced conformational freedom and higher structural rigidity,[13, 14] a very desired property for structural DNA nanotechnology.[1] DNA self-assembly on surfaces involves DNA–DNA interactions and DNA–surface interactions (Figure 1). Both interactions con-
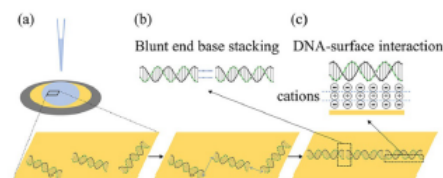
Figure 1. Process of blunt-end stacking–driven DNA self-assembly on a mica surface. A) When DNA solution (light blue) contacts a mica surface (yellow), DNA molecules will loosely adsorb onto the mica surface, then rearrange themselves on the surface to maximize base stacking (highlighted by dashed boxes) between blunt ends. B) Close-up view of the blunt-end interaction. C) DNA–surface attraction by salt bridge. DNA structures are drawn with Tiamat software.[19]

tribute to DNA self-assembly on the surface if the strengths of these two interactions are comparable. The effect of DNA–DNA interactions has been extensively studied,[1–11] but the effect of DNA–surface interactions has barely been explored.[13–15] In this report, we conducted a comprehensive study on the latter and found that DNA–surface interactions have a great effect on DNA self-assembly on the surface. The DNA systems used here are blunt-ended DNA motifs. The interaction between such motifs is only base-pair stacking, which is generally weak.

We started our study with a blunt-ended, three-pointed-star motif (tile).[20] The motif contained three branches, and each branch contained two parallel DNA duplexes. Between any two such tiles, the maximal interaction was two pairs of blunt-end stacking. It was too weak to hold tiles together in solution; thus, only individual tiles were observed in PAGE (Figure S2 in the Supporting Information). However, on a mica surface, the blunt-ended three-pointed star motif can isothermally self-assemble into designed, honeycomb-like 2D arrays within 5 seconds (Figures 2 and S3–S5).

DNA self-assembly on surfaces is influenced by three main factors

1) Ni^{2+} concentration (Figure S3): Ni^{2+} is an effective bridge between negatively charged DNA molecules and negatively charged mica surfaces.[21] A low Ni^{2+} concentration will not provide enough attractive force for DNA to the mica surface; a Ni^{2+} concentration that is too high will result in too strong of a DNA–surface attraction and hinder DNA mobility and rearrangement on the surface. This theoretical reasoning was confirmed in our study. In our experiment, pre-assembled DNA tiles in TAE/Mg^{2+}–Ni^{2+} buffer (containing 2 mM EDTA, 12.5 mM Mg^{2+}, and Ni^{2+}) was deposited onto a mica surface and incubated for a certain time at room temperature, followed by

[a] L. Liu, Prof.Dr. Y. Wang, Prof.Dr. C. Mao
Purdue University, Department of Chemistry
West Lafayette, IN 47906 (USA)
E-mail: mao@purdue.edu
[b] Prof.Dr. Y. Li
Hefei University of Technology
School of Chemistry and Chemical Engineering
Hefei, Anhui 230009 (China)
[c] Prof.Dr. Y. Wang
Nanchang University, College of Chemistry
Nanchang, Jiangxi 330031 (China)
[d] Dr. J. Zheng
Capital Medical University, Beijing Tiantan Hospital
Department of General Surgery
Beijing 100050 (China)
E-mail: zhengjianwei@bjttyy.org
Supporting information and the ORCID identification numbers for the authors of this article can be found under https://doi.org/10.1002/cbic.201700545.
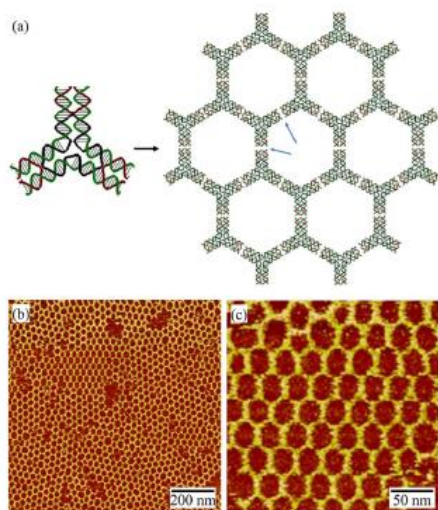
Figure 2. Hexagonal 2D arrays assembled from a blunt-ended three-pointed-star motif. A) Scheme. Blue arrows indicate blunt-end-stacking sites. B) and C) A pair of atomic force microscopy (AFM) images of the DNA chains at different magnifications. Experimental conditions: DNA (100 nm) in TAE/Mg^{2+}–Ni^{2+} (4 mm) buffer, 3 min incubation.

atomic force microscopy (AFM) imaging. No array was detected at 2 mm Ni^{2+}. At 3 mm Ni^{2+}, DNA arrays appeared, but they were fragile during AFM imaging, indicating weak interactions with the mica surface. The jump in array formation from 2 to 3 mm was likely due to the change in the effective Ni^{2+} concentration change. The buffer contained 2 mm EDTA, which can chelate Ni^{2+} nearly 10^{10} times more strongly than Mg^{2+} (judging by the association constant K_a values).[22] Thus, the added 2 mm Ni^{2+} was completely chelated by EDTA, and no free Ni^{2+} existed in the solution. When 3 mm Ni^{2+} was added, 1 mm free Ni^{2+} existed and promoted the 2D array formation. When 4 mm Ni^{2+} was added, regular 2D arrays formed with high coverage and great durability. At even higher Ni^{2+} concentrations (5 mm), 2D arrays started to contain defects. Presumably, intense DNA–surface interactions hindered the movement of DNA tiles on the surface for rearrangement. This result showed that moderate Ni^{2+} concentrations provide the optimal conditions for DNA assembly on mica surfaces.

2) DNA concentration (Figure S4): In TAE/Mg^{2+}–Ni^{2+} (4 mm) solution, DNA (100–600 nm) three-pointed stars formed regular hexagonal 2D arrays with high surface coverage. Some defects were observed, such as small gaps and deformations (mainly pentagons and heptagons). When the DNA concentration was lower than 100 nm, surface coverage decreased as DNA concentration decreased, although 2D arrays could be observed at DNA concentrations as low as 5 nm. This result suggested that overall solution DNA concentration influences the DNA concentration near the surface; in contrast, the Ni^{2+} concentration affects the DNA–surface interaction.

3) Assembly duration (Figure S5): We made an effort to explore the assembly kinetics by varying the assembly duration over a range of 5 seconds to 10 minutes. As shown in Figure S5, at 5 seconds, 2D arrays start to form, even though the surface coverage is low. When assembly duration increased to 3 minutes, high coverage of 2D arrays was observed. These results revealed that the 2D assembly on the surface through base stacking was a fast process when compared with previously reported 2D assembly, dictated by sticky-end cohesion (often > 12 h).

When we extended our study to another similar, branched, four-pointed star DNA motif,[23] an interesting phenomenon has been observed. This motif has been shown to assemble into tetragonal 2D arrays through sticky-end cohesion in solution.[23] However, when subjected to base-stacking-driven surface assembly, it behaved dramatically differently. Not only were tetragonal 2D arrays observed, but trihexagonal and rhombic arrays also existed (Figure 3). Furthermore, by rationally varying the experimental conditions, we were able to partially control the distribution of these conformations.
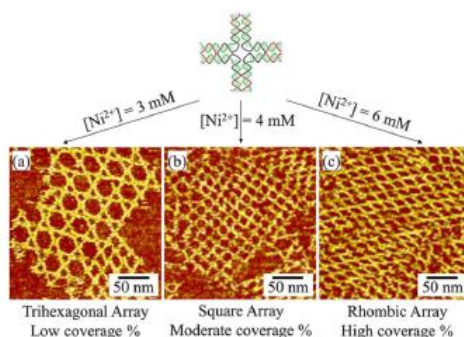
Figure 3. Three different 2D arrays assembled from four-pointed-star motif under different Ni^{2+} concentrations. Experimental conditions: DNA (200 nm) in TAE/Mg^{2+}–Ni^{2+} buffer, 5 min incubation.

The primary controlling factor is the Ni^{2+} concentration (Figure S7). At 2 mm Ni^{2+}, no array was detected, due to Ni^{2+}–EDTA chelation. When the Ni^{2+} concentration was increased to 3 mm, DNA 2D arrays covered ≈50% of the mica surface, and trihexagonal arrays dominated. With 4 mm Ni^{2+}, square arrays became dominating. At 6 mm Ni^{2+}, surface coverage reached about 100%, and dominating arrays changed from trihexagonal arrays and square arrays to squeezed rhombic arrays. When the Ni^{2+} concentration was higher than 7 mm, the surface became too densely packed, and the DNA structures could not maintain their intrinsic shapes (Figure S7 F–H).

To understand the change in the array structure corresponding to the change in Ni^{2+} concentration, we performed a statistical analysis on the DNA 2D arrays within a Ni^{2+} concentration range of 3–6 mm (Figure S8). From trihexagonal arrays to tetragonal arrays to rhombic arrays, the DNA packing density increased, and the area occupied by each four-pointed-star

CHEMBIOCHEM
Communications

motif decreased. Our statistic data showed that a linear relationship exists between the surface coverage and the percentage of the DNA motif in a tetragonal conformation. At a low Ni^{2+} concentration, surface coverage of DNA was low. Each motif could occupy a large surface area, so the DNA arrays tend to adopt a low packing density conformation: trihexagonal arrays. At a high Ni^{2+} concentration, surface coverage of DNA was high. Each motif could only occupy a small surface area, so the DNA arrays tended to adopt a high packing density conformation: rhombic arrays.

To determine the minimal requirement of blunt-end stacking in this system, we turned to 1D structure assembly, in which each DNA tile only interacted with two—instead of three or four—neighboring tiles by blunt-end stacking for DNA self-assembly. We first tested the assembly of the double-crossover (DX) molecule.[24] It contained two parallel DNA duplexes that were linked together by strand crossovers at two locations along the DNA duplexes. Each DX tile can only interact with another two DX tiles through base stacking, potentially leading to formation of long 1D chains. AFM imaging indicated that such 1D chains indeed readily formed (Figures 4 and S9–S11). On the mica surface, a large number of 1D chains could be easily observed (Figure 4). The formation of DX chains depended on both DNA and Ni^{2+} concentrations (Figures S10 and S11). At 500 nM DX, dense 1D chains could be formed in the presence of 2–8 mM Ni^{2+}. They can easily reach 200 nm (15 copies of DX tiles) in length.

An important question in this approach was the minimal number of base-stacking pairs of blunt ends needed to stably associate two building blocks together. In previous works, multiple pairs were involved.[15–18, 25–29] Here, we examined the smallest possible number (one) of pairs of blunt ends. A 24-bp, blunt-ended DNA duplex was used (Figures 5 and S12–S14). The interaction between any two component DNA molecules was only base stacking between one pair of blunt ends. Under
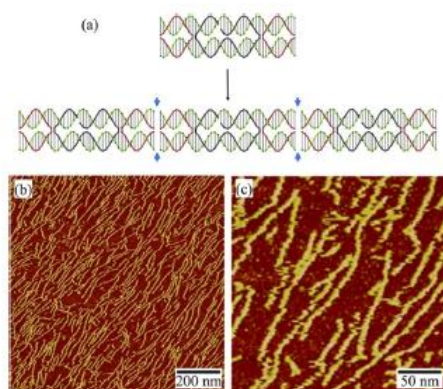
Figure 4. DNA double crossover (DX) assembles into 1D chains on surface. A) Scheme of chain formation. Blue arrows indicate blunt-end-stacking sites. B) and C) AFM images of the DNA chains at different magnifications. Experimental conditions: DNA (200 nM) in TAE/Mg^{2+}– Ni^{2+} buffer (10 mM), 3 min incubation.
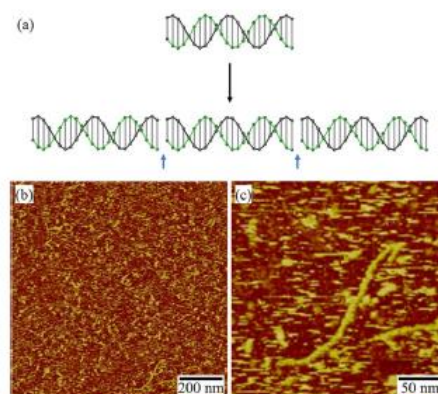
Figure 5. Short, blunt-ended DNA duplexes assemble into long chains on the surface. A) Scheme. Blue arrows indicate blunt-end-stacking sites. B) and C) AFM images of the DNA chains at different magnifications. Experimental conditions: DNA (500 nM) in TAE/Mg^{2+}–Ni^{2+} buffer (10 mM), 5 min incubation.

AFM imaging, some long chains were observed. They were 1D chains assembled from the DNA duplexes and could be up to 250 nm long, corresponding to ≈ 30 duplex molecules associated together (Figure 5). Such assembly also critically depended on both the bulk DNA concentration and Ni^{2+} concentration (Figures S13 and S14). When the Ni^{2+} concentration was lower than 8 mM, no appreciable 1D chain was observed, presumably because the small (24-bp) DNA duplex could not adsorb onto the mica surface. When the Ni^{2+} concentration was in the range of 8–10 mM, 1D DNA chains formed. When the Ni^{2+} concentration was higher than 12 mM, the surface was so densely covered that no chain structure could be distinguished. This result showed that base stacking of only one pair of blunt ends is strong enough to associate DNA building blocks together on a surface.

An interesting phenomenon regulating DNA assembly through a steric effect was found when we studied the assembly of a double six-arm junction (D6aJ) motif.[32] It dramatically changed its final assembly patterns by small structure changes (Figures 6 and S15–S17). A D6aJ motif contained four blunt ends and two short hairpins. Blunt ends can involve base stacking, leading to large structure formation. The two hairpins did not involve inter-motif interactions; however, they could regulate assembly by steric effects. When the hairpins were short, any two D6aJ motifs could stack onto each other with two pairs of blunt ends, leading to formation of 1D D6aJ arrays (Figure 6A). When the hairpins were long, two D6aJ motifs could stack onto each other with one pair instead of two pairs of blunt ends because of the steric hindrance imposed by the long hairpins, leading to 2D array formation (Figure 6B).

In summary, this study provides a new strategy to weak force-driven DNA self-assembly by introducing an orthogonal interaction: DNA–surface interactions. This allows us to regulate DNA self-assembly by tuning the DNA–surface interac-

Figure 6. Sterically controlled DNA self-assembly of DNA double six-arm junction (D6aJ) motif with short hairpins (A and C) and with long middle hairpins (B and D). In each panel, scheme is shown at left and AFM image is shown at right. Experimental conditions: DNA (200 nm) in TAE/Mg^{2+}–Ni^{2+} buffer, 5 min incubation (6 mm Ni^{2+} for D6aJ; 7 mm Ni^{2+} for D6aJ*).

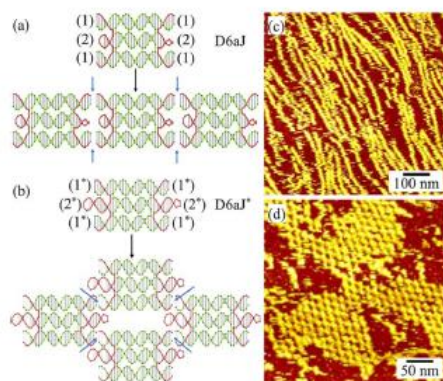tions. It is related to other studies, such as blunt end stacking–driven assembly and surface assembly.[12–18, 25–31] However, this study showed that we could regulate DNA–DNA interactions by weak interaction (base stacking between one or two pairs of blunt ends) by DNA–surface interaction. Long structures arising from assembly of short DNA duplexes, as observed in this study, might be relevant to prebiotic development of life. In addition, this study also demonstrates that large, complex DNA arrays can be assembled isothermally and quickly (≈ 5 s), which is very desirable when concerning the introduction of heat-sensitive guests, such as proteins. In addition, the resulting structures could potentially be useful for high-resolution molecular lithography.[33–35]

Acknowledgements

Conflict of Interest

The authors declare no conflict of interest.

[1] N. C. Seeman Structural DNA Nanotechnology, Cambridge University Press, Cambridge, **2016**.
[2] C. Lin, Y. Liu, H. Yan, Biochemistry **2009**, 48, 1663–1674.
[3] F. A. Aldaye, A. L. Palmer, H. F. Sleiman, Science **2008**, 321, 1795–1799.
[4] C. G. Evans, E. Winfree, Chem. Soc. Rev. **2017**, 46, 3808–3829.
[5] M. R. Jones, N. C. Seeman, C. A. Mirkin, Science **2015**, 347, 1260901.
[6] J. Chen, N. C. Seeman, Nature **1991**, 350, 631–633.
[7] E. Winfree, F. Liu, L. A. Wenzler, N. C. Seeman, Nature **1998**, 394, 539–544.
[8] W. M. Shih, J. D. Quispe, G. F. Joyce, Nature **2004**, 427, 618–621.
[9] P. W. K. Rothemund, Nature **2006**, 440, 297–302.
[10] B. Wei, M. Dai, P. Yin, Nature **2012**, 485, 623–626.
[11] N. C. Seeman, J. Theor. Biol. **1982**, 99, 237–247.
[12] S. Hamada, S. Murata, Angew. Chem. Int. Ed. **2009**, 48, 6820–6823; Angew. Chem. **2009**, 121, 6952–6955.
[13] S. Bashar, C.-W. Lee, J. Lee, B. Kim, B. Gnapareddy, J. Shin, S. R. Dugasani, S. H. Park, RSC Adv. **2013**, 3, 19876–19879.
[14] X. Sun, S. Hyeon Ko, C. Zhang, A. E. Ribbe, C. Mao, J. Am. Chem. Soc. **2009**, 131, 13248–13249.
[15] S. Woo, P. W. K. Rothemund, Nat. Commun. **2014**, 5, 4889.
[16] R. Wang, A. Kuzuya, W. Liu, N. C. Seeman, Chem. Commun. **2010**, 46, 4905–4907.
[17] N. Avakyan, J. W. Conway, H. F. Sleiman, J. Am. Chem. Soc. **2017**, 139, 12027–12034.
[18] G. Tikhomirov, P. Petersen, L. Qian, Nat. Nanotechnol. **2017**, 12, 251–259.
[19] S. Williams, K. Lund, C. Lin, P. Wonka, S. Lindsay, H. Yan in DNA Computing: 14th International Meeting on DNA Computing, DNA 14, Prague, Czech Republic, June 2–9, 2008, Revised Selected Papers (Eds.: A. Goel, F. C. Simmel, P. Sosík), Springer, Berlin, **2009**, pp. 90–101.
[20] Y. He, Y. Chen, H. Liu, A. E. Ribbe, C. Mao, J. Am. Chem. Soc. **2005**, 127, 12202–12203.
[21] M. Bezanilla, B. Drake, E. Nudler, M. Kashlev, P. K. Hansma, H. G. Hansma, Biophys. J. **1994**, 67, 2454–2459.
[22] J. R. Hart in Ullmann's Encyclopedia of Industrial Chemistry, Wiley-VCH, Weinheim, **2000**.
[23] H. Yan, S. H. Park, G. Finkelstein, J. H. Reif, T. H. LaBean, Science **2003**, 301, 1882.
[24] T. J. Fu, N. C. Seeman, Biochemistry **1993**, 32, 3211–3220.
[25] T. Gerling, K. F. Wagenbauer, A. M. Neuner, H. Dietz, Science **2015**, 347, 1446.
[26] H. Yan, T. H. LaBean, L. Feng, J. H. Reif, Proc. Natl. Acad. Sci. USA **2003**, 100, 8103–8108.
[27] A. Aghebat Rafat, T. Pirzer, M. B. Scheible, A. Kostina, F. C. Simmel, Angew. Chem. Int. Ed. **2014**, 53, 7665–7668; Angew. Chem. **2014**, 126, 7797–7801.
[28] S. Kocabey, S. Kempter, J. List, Y. Xing, W. Bae, D. Schiffels, W. M. Shih, F. C. Simmel, T. Liedl, ACS Nano **2015**, 9, 3530–3539.
[29] Y. Suzuki, M. Endo, H. Sugiyama, Nat. Commun. **2015**, 6, 8052.
[30] M. Li, J. Yu, J. Li, E. B. Wang, G. Wang, C. Mao, RSC Adv. **2016**, 6, 76355–76359.
[31] P. R. Dahlgren, Y. L. Lyubchenko, Biochemistry **2002**, 41, 11372–11378.
[32] M. Brucale, G. Zuccheri, L. Rossi, A. Bazzani, G. Castellani, B. Samori, Org. Biomol. Chem. **2006**, 4, 3427–3434.
[33] G. Zhang, S. P. Surwade, F. Zhou, H. Liu, Chem. Soc. Rev. **2013**, 42, 2488–2496.
[34] Z. Deng, C. Mao, Angew. Chem. Int. Ed. **2004**, 43, 4068–4070; Angew. Chem. **2004**, 116, 4160–4162.
[35] S. P. Surwade, S. Zhao, H. Liu, J. Am. Chem. Soc. **2011**, 133, 11868–11871.

Patterning Nanoparticles with DNA Molds

Longfei Liu, Mengxi Zheng, Zhe Li, Qian Li, and Chengde Mao*

Department of Chemistry, Purdue University, West Lafayette, Indiana 47907, United States

S Supporting Information

ABSTRACT: We report a nanopatterning strategy in which self-assembled DNA nanostructures serve as structural templates. In previous work, ordering of NPs primarily relied on specific recognition, e.g., DNA–DNA hybridization. Only a few cases have been reported on nonspecific adsorption. Unfortunately, these studies were limited by the integrity and homogeneity of templates and the variety of patterned nanoparticles (NPs). Herein, we have developed a general method to pattern various NPs. The NPs adsorb onto substrate via NP–substrate direct interactions and the substrates are patterned into large arrays (>4 × 4 μm) of tiny, accessible cavities by self-assembled DNA arrays. As a demonstration, DNA templates include tetragonal and hexagonal arrays and the NPs include individual DNA nanomotifs, gold nanoparticles (AuNPs), and proteins. All nanostructures have been confirmed by atomic force microscopy and corresponding fast Fourier transform (FFT) analysis.

KEYWORDS: DNA nanotechnology, DNA nanostructure, self-assembly, blunt-ended stacking, DNA–surface interaction, nanoparticle

INTRODUCTION

DNA is a promising material to construct programmable nanostructures with excellent precision and shape control. Over the last three decades, a variety of DNA nano-architectures has been constructed.[1–11] Recently, we reported a method to fabricate DNA 2D arrays on solid surfaces from blunt-ended DNA motifs.[12] This method provides large, continuous, and monocrystalline DNA templates. Ordered nanoparticle (NP) arrays have many applications in physics, biosensing, etc. For example, AuNP arrays can serve as substrates for surface-enhanced Raman spectroscopy (SERS) detections.[13] Protein patterning is promising in studying biosensor systems and expanding knowledge in protein–protein and protein–cell interactions.[14–16] Here we develop a general strategy to order various NPs into predesigned patterns by DNA templates (2D arrays) via nonspecific surface adsorption. In this process, DNA templates are first self-assembled on a fresh mica surface from individual, small, blunt-ended DNA motifs. Then the mica surface is coated with positively charged "glues", e.g., Ni²⁺ and poly-L-lysine (PLL). Finally, various NPs are deposited onto the solid surfaces into patterns defined by the DNA templates.

EXPERIMENTAL DESIGN

Figure 1 illustrates the process of patterning NPs by DNA 2D arrays. It is exemplified by a DNA tetragonal arrays from bridged 4-point-star (b4PS) motifs (Figure 1a and Figure S1a). Bridges are introduced to enhance the motif rigidity because unbridged 4-point-star motif could easily adapt different conformations.[12] Another type of DNA array is hexagonal array assembled from rhombus motif (Figure S1b).[17] Between any two motifs, two pairs of blunt-end stacking will offer adequate interaction to associate motifs. The assembly of DNA motifs
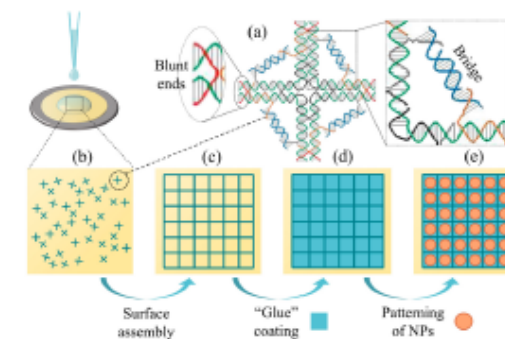
Figure 1. Process of nanoparticle (NP) patterning directed by DNA arrays. (a) Molecular design of bridged 4-point-star (b4PS) motifs. (b) When DNA solution (light blue) contacts a mica surface (yellow), b4PS motifs (blue) will randomly adsorb onto mica surface. (c) Driven by base stacking between blunt ends, b4PS motifs rearrange themselves on the solid surface into 2D arrays. (d) The mica surface is then coated by "glues", which are positively charged materials (poly-L-lysine or Ni²⁺). They are used to trap negatively charged NPs. (e) Patterning NPs (red) by DNA arrays.

on surface results in 2D arrays (Figure 1b, c). Then we modify the surface with positively charged "glues" (Figure 1d). These "glues" can

be Ni^{2+} for DNA motifs and proteins patterning or PLL for AuNPs patterning. In the last step, NPs are trapped by "glues" and patterned by DNA arrays (Figure 1e).

DNA arrays were assembled in two steps according to our previous method.[12] (i) Assembly of individual DNA motifs in solution. All component strands were mixed at designated ratios in TA/Mg^{2+} buffer and the mixture solutions were thermal annealed (see the Supporting Information for details). The formation of individual motifs was confirmed by native polyacrylamide gel electrophoresis, PAGE (Figures S2 and S3). (ii) Surface-assisted self-assembly of DNA arrays from motifs. Preformed, individual DNA motifs were deposited onto a freshly cleaved mica surface. Isothermal incubation at 22 °C led to the assembly of large single-crystal arrays (Figure 1b, c and Figure S4b, e). One advantage of the surface-assisted self-assembly is that it allows readily optimizing integrity and global homogeneity of single-crystal arrays by tuning concentration of Mg^{2+}, $[Mg^{2+}]$. The strength of DNA-surface interaction positively correlates with $[Mg^{2+}]$. Too low $[Mg^{2+}]$ leads to insufficient DNA-surface interaction, resulting in small pieces of DNA arrays (Figure S4a, d); too high $[Mg^{2+}]$ leads to too strong DNA-surface interaction, resulting in poly crystals (Figure S4c, f). Only at proper $[Mg^{2+}]$, DNA-surface interaction is moderate and large-scale arrays can form with global homogeneity. The arrays are over 4 μm × 4 μm in area and contain more than 20 000 and 34 000 wells for tetragonal and hexagonal arrays, respectively, as observed by AFM (Figure S4b, e).

One question is whether the formed DNA arrays can be preserved during "glue" coating process. To test the integrity of DNA arrays, we imaged the samples after each step of the process (Figure S5). Before coating, DNA arrays were checked to ensure intactness (Figure S5a). For patterning of AuNPs, poly-L-lysine (PLL), a type of strong "glue", was required. To enhance DNA-surface interaction, 2 mM Ni^{2+} was added to PLL solution. After coating with PLL, DNA arrays remained intact (Figure S5b). Next step was to remove excessive, unbound or loosely bound PLL by washing with $TA/Mg^{2+}/Ni^{2+}$ solution (see the Supporting Information for details), containing 10 mM Mg^{2+} and 2 mM Ni^{2+}. Mg^{2+} was for stabilizing DNA nanostructures and Ni^{2+} was for enhancing DNA-surface interaction. AFM images also confirmed the integrity of DNA arrays after washes (Figure S5c). For patterning of DNA motifs and proteins, PLL coating process was removed because Ni^{2+} is strong enough as "glue". So washing with $TA/Mg^{2+}/Ni^{2+}$ solution would also function as "glue" coating process.

■ RESULTS

Patterning DNA Nanostructures. We started our study with patterning of DNA 3-point-star (3PS) motifs (Figure 2). This motif contains three identical branches, and each branch contains two parallel DNA duplexes (Figure S1c). One duplex is blunt-ended while the other has a 10T single-stranded overhang at the peripheral end to prevent intermotif association via blunt-end stacking (Figure S1e). After forming tetragonal or hexagonal arrays, exposure of the mica surfaces to 3PS motifs resulted in cavity-occupied patterning of 3PS motifs (Figure 2a–d). By increasing the concentration of 3PS motif, [3PS], the cavity occupancy increased from low to high level (Figure S6). Our statistical analysis indicated that the cavity occupancy rate could reach almost 100% when [3PS] was 75 nM (Figure 2e).

Then we extended our study to another DNA motif, 4-point-star (4PS) motif. 4PS motif has the same design as 3PS motif except that it contains 4 branches (Figure S 1d, e). Similar tunable patterning results were obtained (Figure 3 and Figure S7). Almost 100% cavity occupancy was obtained at [4PS] of 50 nM for tetragonal arrays and 60 nM for hexagonal arrays. Due to the space limit of the cavity, most DNA motif patterns followed the single-motif-per-cavity rule. However, when the concentration of DNA motifs was high enough, one cavity could trap two motifs, highlighted by circles in Figures S6c, f
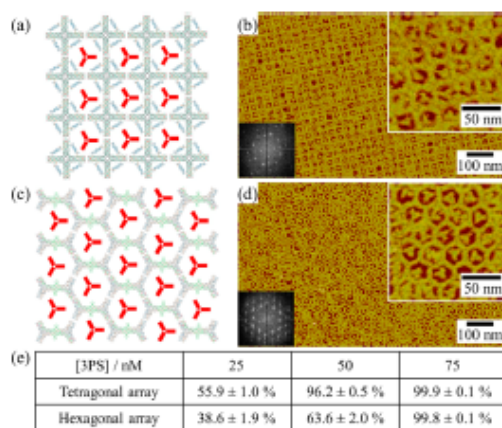
Figure 2. Patterning of DNA three-point-star nanomotifs (3PS motifs) by DNA arrays. Schematic presentation of patterning by (a) tetragonal arrays and (c) hexagonal arrays. 3PS motifs are colored red. (b, d) AFM images of a and c. FFT patterns and close-up views are shown at lower left and upper right, respectively. (e) Statistics of cavity occupancy against [3PS].

[3PS] / nM	25	50	75
Tetragonal array	55.9 ± 1.0 %	96.2 ± 0.5 %	99.9 ± 0.1 %
Hexagonal array	38.6 ± 1.9 %	63.6 ± 2.0 %	99.8 ± 0.1 %
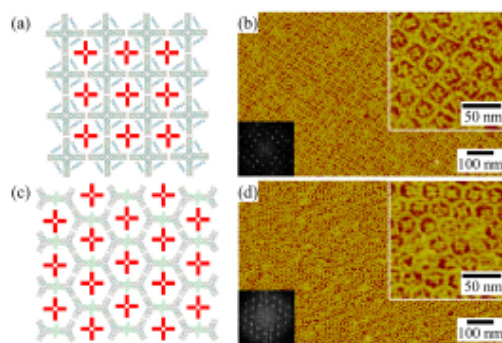
Figure 3. Patterning of DNA four-point-star nanomotifs (4PS motifs) by DNA arrays. Schematic presentation of patterning by (a) tetragonal arrays and (c) hexagonal arrays. 4PS motifs are colored red. (b, d) AFM images of a and c. FFT patterns and close-up views are shown at lower left and upper right, respectively.

and S7c, f. This was probably because the DNA motifs contained certain flexibility to adapt themselves to a more compact space.

Patterning AuNPs. AuNPs are one of the most important metal colloids for their unique physical properties and wide applications in electronics, plasmonics, biomaterials, etc.[18−21] Since Mirkin et al. first reported modification of AuNPs with DNA oligonucleotides,[22] this method has been broadly applied to organize AuNPs in various one- (1D),[23] two- (2D),[23] and three-dimensional (3D) lattices,[24,25] and satellite shapes.[26−28] An alternative strategy to order AuNPs is self-assembly of AuNPs templated by DNA nanostructures.[29−31] Both methods require strict DNA sequence design to enable specific DNA−DNA hybridization. To achieve AuNP patterning in a nonspecific way, Cheng and co-workers reported a free-standing NP superlattice by using DNA-modified AuNPs.[32] In

their work, DNA was used as a "dry ligand" instead of a recognizable tool. However, their nanopatterning was limited to close-packed hexagonal shape due to lack of templating guidance. Our previous work showed a DNA-templated fabrication of AuNPs by thermal evaporation coating.[35] But it suffered from discrete distribution of AuNPs on DNA templates and difficult control of uniform size of AuNPs. Herein, we used our current method to pattern AuNPs by DNA arrays. AuNPs of 5 and 10 nm were used after modification with 22-nt, single-stranded, random-sequenced DNA. To ensure efficient adsorption, mica surfaces were coated with PLL, a strong positively charged "glue" (Figure S5). Note that the overall diameters of DNA-modified AuNPs at dry conditions are ~5.8 nm (for 5 nm AuNP) and ~10.5 nm (for 10 nm AuNP). Both are much smaller than the cavities of the DNA 2D arrays (~27.4 nm for square wells and ~30.3 nm for hexagonal wells).

Figure 4 illustrated AuNPs patterned by tetragonal DNA arrays. AuNPs (red spheres) stood in the cavities formed by

Figure 4. (a) Schematic presentation of AuNPs patterning by tetragonal DNA arrays. AuNPs are colored red. (b) AFM image of tetragonal arrays. (c, d) AFM image of patterned 5 and 10 nm AuNPs, respectively. A set of white dashed lines indicate the orientation of patterned AuNPs. In b–d, FFT patterns and close-up views are shown at lower left and upper right, respectively.

tetragonal arrays as shown in Figure 4a. After formation of tetragonal arrays from b4PS motifs (Figure 4b) and PLL coating, 5 or 10 nm AuNPs were deposited onto mica surfaces and visualized by AFM. AFM images of both 5 and 10 nm AuNP patterns indicated tetragonal ordering directed by DNA arrays, and their FFT patterns showed clear tetragonal symmetry (Figure 4c, d), which was obviously different from template-free, random adsorption (Figure S8). White lines in Figure 4c, d indicated the orientations of patterned AuNPs, which agreed with the corresponding FFT patterns. Because of the different sizes of two AuNPs, one cavity of tetragonal DNA arrays preferred to hold multiple 5 nm AuNPs (Figure 4c) but a single 10 nm AuNP (Figure 4d).

To further investigate DNA arrays' templating effect on AuNPs, we determined their spatial relationship and compared their repeating distances. Because of the height difference between DNA duplexes and AuNPs, AFM images only displayed higher AuNP patterns when AuNPs were compactly

packed. To determine the relative position of AuNPs on DNA arrays, we required simultaneous observation of DNA arrays and AuNPs. One method was to reduce the density of AuNPs. A map of sparse AuNPs was obtained, which allowed observation of AuNPs and DNA arrays at the same time (Figure S9a). A close-up view indicated most AuNPs stood in the cavities formed by DNA arrays, which confirmed our hypothesis (Figure S9b). Furthermore, Figure S10 showed measured repeating distances of 5 and 10 nm AuNP patterns, which were close to that of DNA arrays. This also confirmed DNA arrays' templating effect on AuNPs regardless of their sizes.

To study the percentage of cavities occupied by AuNPs, we performed an FFT analysis (Figures S11–13). Briefly, FFT patterns were generated from the AFM images. Then diffraction spots of tetragonal symmetry, highlighted by green circles, were selected (Figure S11a, c) and were used to generate inverse FFT images via inverse FFT operation (Figure S11b, d). In the inverse FFT images, dot patterns of tetragonal symmetry were shown in three different colors: (i) yellow dots represent AuNP-occupied cavities, highlighted by circles; (ii) red dots represent AuNP-unoccupied cavities, highlighted by squares; (iii) white dots represented AuNP aggregates, highlighted by hexagons. Their positions in original AFM images were also matched, highlighted by corresponding shapes. Statistical analysis indicated cavity occupancy of 94.9 ± 0.3% for 5 nm AuNPs and 80.8 ± 1.2% for 10 nm AuNPs. The higher occupancy for 5 nm AuNPs is probably due to their higher concentration in bulk solution.

We also examined 5 nm AuNPs patterned by the hexagonal arrays (Figure 5 and Figure S14). Similarly, white dashed lines showed three organizing orientations, which agreed with the FFT diffraction patterns of hexagonal symmetry (Figure 5c). In the inverse FFT images, colored dot patterns revealed the
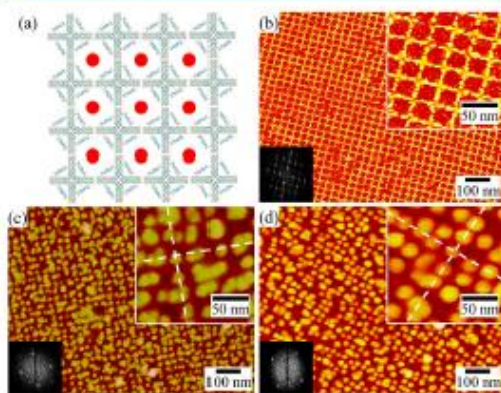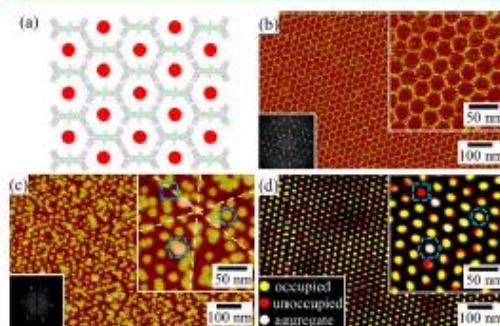

Figure 5. Patterning of AuNPs by hexagonal DNA arrays. (a) Schematic presentation of AuNPs patterning by hexagonal arrays. AuNPs are colored red. (b) AFM image of hexagonal arrays. (c) AFM image of patterned 5 nm AuNPs. A set of white dashed lines indicate the orientation of patterned AuNPs. In b and c, FFT patterns and close-up views are shown at lower left and upper right, respectively. (d) Inverse FFT image of c is generated from diffraction spots. Yellow dots stand for AuNP-occupied cavities, highlighted by blue dashed circles; red dots stand for AuNP-unoccupied cavities, highlighted by blue dashed squares; and white dots stand for AuNP aggregates, highlighted by blue dashed hexagons. In close-up views at upper right, three types of dots are highlighted, corresponding to those in c.

C

ordering of AuNPs and the cavity occupancy (Figure 5d). This also demonstrated the versatility of DNA templates.

Patterning Proteins. Patterning proteins directed by DNA arrays has been broadly reported. Specific binding was the most commonly used technique, e.g., streptavidin−biotin binding[7,34−36] and antigen−antibody interaction.[37] Recently, Ramakrishnan et al. reported nonspecific adsorption of various negatively charged proteins directed by surface-assembled DNA origami nanostructures.[38] Herein, we used our system to pattern proteins, both negatively and positively charged. Moreover, our DNA arrays contained denser cavities (~1200 or 2000 cavities per μm^2) compared with those in the origami arrays (~100 cavities per μm^2).[38]

We first studied the negatively charged ovalbumin (OVA, pI ~ 4.52).[39] OVA is a main protein in egg white, consisting of 385 residues with a molecular weight of ~42.7 kDa.[40] OVA adsorption on mica surface was controlled by [OVA] in bulk solution. Figure 6 showed AFM images of patterned OVAs by
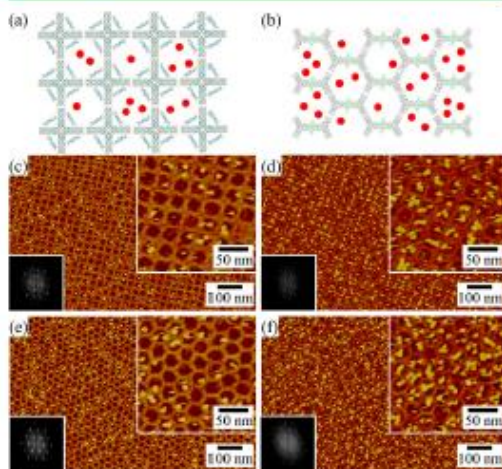

Figure 6. (a, b) Schematic presentations of ovalbumin (OVA) patterning by DNA arrays. OVAs are colored red. (c, d) AFM images of patterned OVAs by tetragonal arrays at different concentration of OVA ([OVA]). (e, f) AFM images of patterned OVAs by hexagonal arrays at different [OVA]. In (c-f), FFT patterns and close-up views are shown at lower left and upper right, respectively. [OVA] is 25 nM for (c, e) and 75 nM for (d, f).

tetragonal and hexagonal arrays at [OVA] of 25 and 75 nM. At 25 nM, cavities were partially occupied and preferred to load single OVA per cavity (Figure 6c, e). Increasing [OVA] resulted in higher cavity occupancy (Figures S15 and 16). When [OVA] reached 75 nM, almost all cavities were occupied, and each cavity preferred to load multiple OVAs (Figure 6d, f). When we further investigated OVA patterning directed by tetragonal arrays by increasing [OVA] up to 400 nM, almost all cavities were occupied with crowded OVAs (Figure S15).

Then, we studied the positively charged lysozyme (LYZ, pI ~ 11.35).[41] LYZ is also abundant in egg white, consisting of 129 residues with a molecular weight of ~14.3 kDa.[42] Different from OVA, LYZ could directly adsorb on either mica surfaces or DNA backbones. Figure S17 showed AFM images of

patterned LYZs by tetragonal and hexagonal arrays at [LYZ] of 100, 150, and 200 nM. LYZs could easily be identified in the cavities but LYZ concentration had relatively less influence on the cavity occupancy. Interestingly, at high [LYZ] of 200 nM, the DNA arrays blurred possibly due to massive accumulation of LYZ on DNA backbones (Figure S17c, f).

DNA−Silica Hybrid Networks. In a recent milestone works, a general method was introduced by Yan, Fan et al. to grow silica nanostructures with DNA nanostructures as templates.[43,44] Herein, we applied this method to construct DNA-silica hybrid networks, in other words, organizing in situ synthesized, tiny silica particles along DNA backbones. Figure 7a, b showed a pair of AFM images of tetragonal and hexagonal
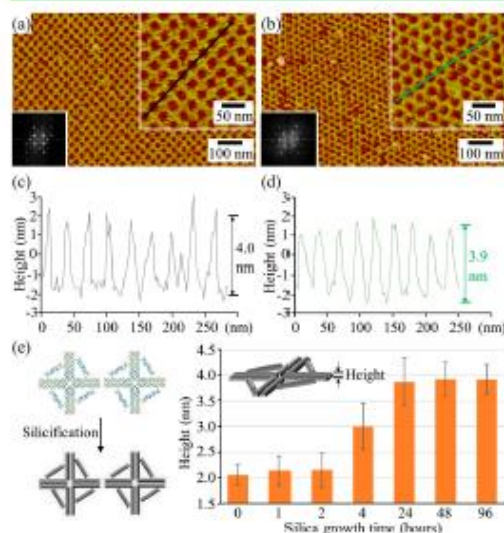
Figure 7. Silicification of DNA arrays. (a, b) Tetragonal arrays and hexagonal arrays with 48 h silica growth. FFT patterns and close-up views are shown at lower left and upper right, respectively. (c, d) Height analysis of a and b along corresponding colored lines. Averaged heights are labeled beside the figures. (e) Height change of tetragonal arrays along increasing silica growth time. Process from tetragonal DNA arrays to silica-decorated structures by silicification.

arrays with 48-h silica growth. Height analysis indicated that the height of network backbones increased to ~4 nm, which was twice the height of DNA duplexes (Figure 7c, d). To investigate the process of the silica growth, we captured AFM images at different incubation time points (Figure S18). At 1 h, silica complex was rarely observed on DNA backbones. At 2 h, silica complex started to partially covered DNA backbones. Both bared DNA backbones and silica-decorated backbones were observed (Figure S18b). At 4 h, silica complex continued to cover more area of DNA arrays. Starting from 24 h, the silica-covered DNA arrays reached about ~100%. Statistical analysis revealed an increasing height between 0 to 24 h and a stable, maximum height of ~4 nm after 24 h (Figure 7e).

CONCLUSION

In summary, we have developed a biotemplating strategy for ordering various NPs into expected 2D patterns via NP−

surface or NP–DNA interaction. The adsorption relies on nonspecific charge–charge interaction, which makes it a general approach. The NPs include DNA nanomotifs, AuNPs, proteins, and silica complex, which demonstrates the versatility of this method. By tuning the concentration of NPs in bulk solution, it is feasible to achieve different cavity occupancy. This overall strategy will be expected to order a large range of NP candidates into designated patterns.

■ ASSOCIATED CONTENT

Ⓢ Supporting Information

The Supporting Information is available free of charge on the ACS Publications website at DOI: 10.1021/acsami.8b22691.

> Materials, methods, DNA sequences, design of DNA nanomotifs, and additional experimental data (native PAGEs and AFM images) (PDF)

■ AUTHOR INFORMATION

Corresponding Author
*Email: mao@purdue.edu.

ORCID Ⓘ
Chengde Mao: 0000-0001-7516-8666

Notes
The authors declare no competing financial interest.

■ ACKNOWLEDGMENTS

■ REFERENCES

(1) Seeman, N. C. Structural DNA Nanotechnology; Cambridge University Press: Cambridge, U.K., 2016.
(2) Lin, C.; Liu, Y.; Yan, H. Designer DNA Nanoarchitectures. Biochemistry 2009, 48, 1663–1674.
(3) Aldaye, F. A.; Palmer, A. L.; Sleiman, H. F. Assembling Materials with DNA as the Guide. Science 2008, 321, 1795–1799.
(4) Evans, C. G.; Winfree, E. Physical Principles for DNA Tile Self-Assembly. Chem. Soc. Rev. 2017, 46, 3808–3829.
(5) Jones, M. R.; Seeman, N. C.; Mirkin, C. A. Programmable Materials and the Nature of the DNA Bond. Science 2015, 347, 1260901.
(6) Chen, J.; Seeman, N. C. Synthesis from DNA of a Molecule with the Connectivity of a Cube. Nature 1991, 350, 631–633.
(7) Winfree, E.; Liu, F.; Wenzler, L. A.; Seeman, N. C. Design and Self-Assembly of Two-Dimensional DNA Crystals. Nature 1998, 394, 539–544.
(8) Ge, Z.; Gu, H.; Li, Q.; Fan, C. Concept And Development of Framework Nucleic Acids. J. Am. Chem. Soc. 2018, 140, 17808–17819.
(9) Rothemund, P. W. Folding DNA to Create Nanoscale Shapes and Patterns. Nature 2006, 440, 297–302.
(10) Wei, B.; Dai, M.; Yin, P. Complex Shapes Self-Assembled from Single-Stranded DNA Tiles. Nature 2012, 485, 623–626.
(11) Seeman, N. C. Nucleic Acid Junctions and Lattices. J. Theor. Biol. 1982, 99, 237–247.
(12) Liu, L.; Li, Y.; Wang, Y.; Zheng, J.; Mao, C. Regulating DNA Self-Assembly by DNA–Surface Interactions. ChemBioChem 2017, 18, 2404–2407.
(13) Wang, H.; Levin, C. S.; Halas, N. J. Nanosphere Arrays with Controlled Sub-10-nm Gaps as Surface-Enhanced Raman Spectroscopy Substrates. J. Am. Chem. Soc. 2005, 127, 14992–14993.
(14) Mrksich, M.; Whitesides, G. M. Using Self-Assembled Monolayers to Understand the Interactions of Man-made Surfaces with Proteins and Cells. Annu. Rev. Biophys. Biomol. Struct. 1996, 25, 55–78.
(15) Veiseh, M.; Zareie, M. H.; Zhang, M. Highly Selective Protein Patterning on Gold–Silicon Substrates for Biosensor Applications. Langmuir 2002, 18, 6671–6678.
(16) Ganesan, R.; Kratz, K.; Lendlein, A. Multicomponent Protein Patterning of Material Surfaces. J. Mater. Chem. 2010, 20, 7322–7331.
(17) Li, X.; Zhang, C.; Hao, C.; Tian, C.; Wang, G.; Mao, C. DNA Polyhedra with T-Linkage. ACS Nano 2012, 6, 5138–5142.
(18) Daniel, M. C.; Astruc, D. Gold Nanoparticles: Assembly, Supramolecular Chemistry, Quantum-Size-Related Properties, and Applications toward Biology, Catalysis, and Nanotechnology. Chem. Rev. 2004, 104, 293–346.
(19) He, L.; Musick, M. D.; Nicewarner, S. R.; Salinas, F. G.; Benkovic, S. J.; Natan, M. J.; Keating, C. D. Colloidal Au-Enhanced Surface Plasmon Resonance for Ultrasensitive Detection of DNA Hybridization. J. Am. Chem. Soc. 2000, 122, 9071–9077.
(20) Kuzyk, A.; Schreiber, R.; Fan, Z.; Pardatscher, G.; Roller, E. M.; Högele, A.; Simmel, F. C.; Govorov, A. O.; Liedl, T. DNA-Based Self-Assembly of Chiral Plasmonic Nanostructures with Tailored Optical Response. Nature 2012, 483, 311–314.
(21) Chou, L. Y.; Zagorovsky, K.; Chan, W. C. DNA Assembly of Nanoparticle Superstructures for Controlled Biological Delivery and Elimination. Nat. Nanotechnol. 2014, 9, 148–155.
(22) Mirkin, C. A.; Letsinger, R. L.; Mucic, R. C.; Storhoff, J. J. A DNA-Based Method for Rationally Assembling Nanoparticles into Macroscopic Materials. Nature 1996, 382, 607–609.
(23) Schreiber, R.; Santiago, I.; Ardavan, A.; Turberfield, A. J. Ordering Gold Nanoparticles with DNA Origami Nanoflowers. ACS Nano 2016, 10, 7303–7306.
(24) Macfarlane, R. J.; Lee, B.; Jones, M. R.; Harris, N.; Schatz, G. C.; Mirkin, C. A. Nanoparticle Superlattice Engineering with DNA. Science 2011, 334, 204–208.
(25) Nykypanchuk, D.; Maye, M. M.; Van Der Lelie, D.; Gang, O. DNA-Guided Crystallization of Colloidal Nanoparticles. Nature 2008, 451, 549–552.
(26) Li, Y.; Liu, Z.; Yu, G.; Jiang, W.; Mao, C. Self-Assembly of Molecule-Like Nanoparticle Clusters Directed by DNA Nanocages. J. Am. Chem. Soc. 2015, 137, 4320–4323.
(27) Edwardson, T. G.; Lau, K. L.; Bousmail, D.; Serpell, C. J.; Sleiman, H. F. Transfer of Molecular Recognition Information from DNA Nanostructures to Gold Nanoparticles. Nat. Chem. 2016, 8, 162–170.
(28) Ohta, S.; Glancy, D.; Chan, W. C. DNA-Controlled Dynamic Colloidal Nanoparticle Systems for Mediating Cellular Interaction. Science 2016, 351, 841–845.
(29) Zhang, J.; Liu, Y.; Ke, Y.; Yan, H. Periodic Square-Like Gold Nanoparticle Arrays Templated by Self-Assembled 2D DNA Nano-grids on a Surface. Nano Lett. 2006, 6, 248–251.
(30) Pinto, Y. Y.; Le, J. D.; Seeman, N. C.; Musier-Forsyth, K.; Taton, T. A.; Kiehl, R. A. Sequence-Encoded Self-Assembly of Multiple-Nanocomponent Arrays by 2D DNA Scaffolding. Nano Lett. 2005, 5, 2399–2402.
(31) Zheng, J.; Constantinou, P. E.; Micheel, C.; Alivisatos, A. P.; Kiehl, R. A.; Seeman, N. C. Two-Dimensional Nanoparticle Arrays Show the Organizational Power of Robust DNA Motifs. Nano Lett. 2006, 6, 1502–1504.
(32) Cheng, W.; Campolongo, M. J.; Cha, J. J.; Tan, S. J.; Umbach, C. C.; Muller, D. A.; Luo, D. Free-Standing Nanoparticle Superlattice Sheets Controlled by DNA. Nat. Mater. 2009, 8, 519–525.
(33) He, Y.; Ye, T.; Ribbe, A. E.; Mao, C. DNA-Templated Fabrication of Two-Dimensional Metallic Nanostructures by Thermal Evaporation Coating. J. Am. Chem. Soc. 2011, 133, 1742–1744.
(34) Yan, H.; Park, S. H.; Finkelstein, G.; Reif, J. H.; LaBean, T. H. DNA-Templated Self-Assembly of Protein Arrays and Highly Conductive Nanowires. Science 2003, 301, 1882–1884.
(35) Aghebat Rafat, A.; Pirzer, T.; Scheible, M. B.; Kostina, A.; Simmel, F. C. Surface-Assisted Large-Scale Ordering of DNA Origami Tiles. Angew. Chem., Int. Ed. 2014, 53, 7665–7668.

(36) Suzuki, Y.; Endo, M.; Sugiyama, H. Lipid-Bilayer-Assisted Two-Dimensional Self-Assembly of DNA Origami Nanostructures. *Nat. Commun.* **2015**, *6*, 8052.

(37) He, Y.; Tian, Y.; Ribbe, A. E.; Mao, C. Antibody Nanoarrays with a Pitch of ~ 20 Nanometers. *J. Am. Chem. Soc.* **2006**, *128*, 12664−12665.

(38) Ramakrishnan, S.; Subramaniam, S.; Stewart, A. F.; Grundmeier, G.; Keller, A. Regular Nanoscale Protein Patterns via Directed Adsorption through Self-Assembled DNA Origami Masks. *ACS Appl. Mater. Interfaces* **2016**, *8*, 31239−31247.

(39) Beeley, J. A.; Stevenson, S. M.; Beeley, J. G. Polyacrylamide Gel Isoelectric Focusing of Proteins: Determination of Isoelectric Points Using an Antimony Electrode. *Biochim. Biophys. Acta, Protein Struct.* **1972**, *285*, 293−300.

(40) Nisbet, A. D.; Saundry, R. H.; Moir, A. J.; Fothergill, L. A.; Fothergill, J. E. The Complete Amino-Acid Sequence of Hen Ovalbumin. *Eur. J. Biochem.* **1981**, *115*, 335−345.

(41) Wetter, L. R.; Deutsch, H. F. Immunological Studies on Egg White Proteins. *J. Biol. Chem.* **1951**, *192*, 237−242.

(42) Canfield, R. E. The Amino Acid Sequence of Egg White Lysozyme. *J. Biol. Chem.* **1963**, *238*, 2698−2707.

(43) Liu, X.; Zhang, F.; Jing, X.; Pan, M.; Liu, P.; Li, W.; Zhu, B.; Li, J.; Chen, H.; Wang, L.; Lin, J.; Liu, Y.; Zhao, D.; Yan, H.; Fan, C. Complex Silica Composite Nanomaterials Templated with DNA Origami. *Nature* **2018**, *559*, 593−598.

(44) Nguyen, L.; Döblinger, M.; Liedl, T.; Heuer-Jungemann, A. DNA−Origami−Templated Silica Growth by Sol−Gel Chemistry. *Angew. Chem., Int. Ed.* **2019**, *58*, 912−916.

Rational Design and Self-Assembly of Two-Dimensional, Dodecagonal DNA Quasicrystals

Longfei Liu,[†] Zhe Li,[†] Yulin Li,[†,‡] and Chengde Mao*,[†]

[†]Department of Chemistry, Purdue University, West Lafayette, Indiana 47907, United States
[‡]School of Chemistry and Chemical Engineering, Hefei University of Technology, Hefei, Anhui 230009, China

S *Supporting Information*

ABSTRACT: Quasicrystals are a class of materials with long-range order but no translational periodicity. Though many quasicrystals have been discovered, rational design and engineering of quasicrystals remain a great challenge. Herein, we have developed a rational strategy to assemble two-dimensional (2D), dodecagonal quasicrystals from branched DNA nanomotifs. The key of our strategy is to balance the rigidity and flexibility of the motifs, which is controlled by the introduction of interbranch "bridges". By fine-tuning the experimental conditions, we are able to predictably produce either 2D quasicrystals or conventional crystals. This study presents a rational design, prediction and realization of quasicrystal formation.

Quasicrystals have been extensively studied over last three decades. They exhibit long-range orientational orders but lack translational symmetries. Although quasicrystals have been discovered in a wide range of materials,[1−6] it remains a challenge to rationally design and engineer quasicrystal structures. Theoretical design is straightforward in mathematics sense,[7−9] but physical realization is prohibited by the difficulty of the design of suitable building bricks.

DNA provides an excellent model system for studying quasicrystal formation. Over the last 35 years, DNA has been exploited to construct a wide range of nanostructures because of its excellent programming capability and structural simplicity.[10−14] Small DNA nanomotifs can self-assemble into large crystalline structures.[11,12,15,16] Recently, we have reported a strategy to assemble large DNA 2D arrays via blunt-end stacking on solid surface with great toleration of motif flexibility and avoiding formation of 3D aggregates.[17] Inspired by these works, herein, we propose a framework to rationally engineer dodecagonal quasicrystals with 12-fold diffraction symmetry from binary DNA tiles, bridged 5- and 6-point-star motifs (b5PS and b6PS).

Figure 1 illustrates our overall design. A dodecagonal, 2D quasicrystal can be dissected into three basic blocks: two 5-branch vertices and one 6-branch vertex. While the 6-branch vertex [III (3^6)] has a 6-fold rotational symmetry, the 5-branch vertices adapt asymmetric configurations, either I ($3^2·4·3·4$) or II ($3^3·4^2$). DNA motifs, b5PS and b6PS, would perfectly serve as such building blocks. The DNA nanomotifs are designed to enable smart rigidity control and effective self-assembly in 2D. All branches in a motif are identical to each other and each is a 4-turn-long, DNA double crossover (Figure S1c,d). Between
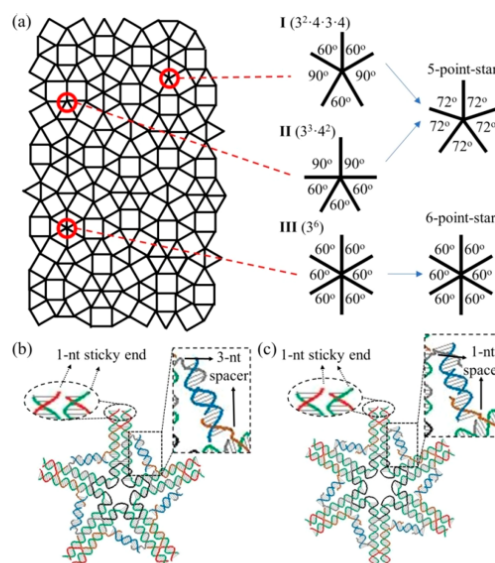
Figure 1. Rational design of dodecagonal quasicrystals. (a) A dodecagonal, 2D quasicrystal consists of three different vertices, I, II, and III, highlighted by red circles. I/II and III are 5- and 6-point-star motifs (5PS and 6PS), respectively. Panels b and c show the corresponding molecular designs of symmetric, bridged 5- and 6-point-star, DNA motifs, b5PS and b6PS (drawing by Tiamat). While the DNA b6PS motif is rigid, the b5PS motif is engineered to contain certain flexibility to accommodate both I or II conformations. nt: nucleotide.

any two adjacent branches, a bridge is introduced to control the interbranch angle and the rigidity of the motif. In the current design, the bridge length should range from 7.7 nm (60°) to 10.2 nm (90°), Figure S2a. The bridge is a rigid, 20-base pair (bp)-long duplex (6.9 nm, Figure S2b) flanked with two flexible, ssDNA spacers. Each nucleotide (nt) in an ssDNA can be stretched to ~0.67 nm long. For the b6PS motif, 1-nt-long spacers are used to fix the interbranch angle at approximately 60°. For the b5PS motif, 3-nt-long spacers are

used. As such, it is sufficiently rigid to avoid random aggregation and sufficiently flexible to adapt both conformations I and II, which both have interbranch angles 60° and 90°. When the spacers are stretched, the interbranch angle can reach 90°; when the spacers are relaxed, the interbranch angle can adapt 60°. These bridges provide important control for the rigidity/flexibility of the motifs. Without the bridges, similar motifs (unbridged 5PS and 6PS) are too flexible and could not maintain their designed geometry during assembly (Figures S3 and S4). To promote intermotif interactions, two 1-nt, sticky ends are introduced at the peripheral end of each branch.

In this design, the DNA motifs have several desired features: (1) Both motifs have the same arm length, meeting the demand of identical distance between any two neighboring vertices of the quasicrystals; (2) Both motifs have the same self-complementary sticky ends, enabling equal-probable and random association among b5PS and b6PS motifs; (3) With 3-nt spacers, motif b5PS can adapt the interbranch angle of either 60° or 90°, as demanded by dodecagonal quasicrystals; (4) Motif b6PS is rigid to maintain its 6-fold rotational symmetry; (5) DNA-surface interaction will confine and stabilize the assembled DNA networks onto flat surfaces and prevent 3D aggregates formation.

DNA self-assembly was conducted in two steps according to a reported method:[17] (i) Assembly of individual DNA motifs separately in solution and then (ii) surface-assisted self-assembly of DNA networks from the two-motif mixtures. The formation of the individual motifs was confirmed by native polyacrylamide gel electrophoresis PAGE (Figures S5−S7) and the assembled, large DNA networks were directly imaged by atomic force microscopy (AFM).

DNA 2D quasicrystals and/or crystals formed depending on the molar ratio of b5PS:b6PS in the solution (Figure 2). The resulting structures show clear FFT (fast Fourier transform) patterns, which allow ready analysis of the structure symmetries. All the (quasi)crystals consisted of only three types of vertices: I ($3^2 \cdot 4 \cdot 3 \cdot 4$), II ($3^3 \cdot 4^2$), and III ($3^6$). When b5PS:b6PS = 100:0, b5PS motif took conformation I and assembled into tetragonal crystals (snub square tiling) as in previous study (Figures 2a and S8).[18] When small amount of b6PS motif was introduced into the system (b5PS:b6PS = 95:5), dodecagonal quasicrystals started to form besides the tetragonal-crystal (Figure S9). In close-up views, both tetragonal crystals (Figure S9b,d) and quasicrystals (Figure S9c,f) were observed. Increasing b5PS:b6PS ratio to 90:10, 85:15, or 80:20, dodecagonal quasicrystals formed, which contained both b5PS and b6PS motifs (Figures 2b,c, S10−12). When more b6PS motif was introduced (b5PS:b6PS = 75:25), dodecagonal quasicrystal feature started to fade (Figure S13). FFT patterns still showed 12-fold symmetry but became less distinct (Figure S13d,e). Small hexagonal crystalline domains (triangular tiling) assembled as b6PS motif amount increased (Figure S13f). When the ratio reached 70:30, hexagonal crystals expanded and mixtures of dodecagonal quasicrystals and hexagonal crystals were resulted (Figures 2d and S14). With even more b6PS (b5PS:b6PS = 60:40), quasicrystals completely disappeared; only poly domained, hexagonal crystals of b6PS motifs were assembled (Figure 2e and S15). At domain boundaries, some 5bPS motifs were observed (Figure S15c), which hindered the formation of single hexagonal crystals. When b5PS:b6PS = 0:100, b6PS assembled into large, hexagonal crystals as in previous study (Figures 2f
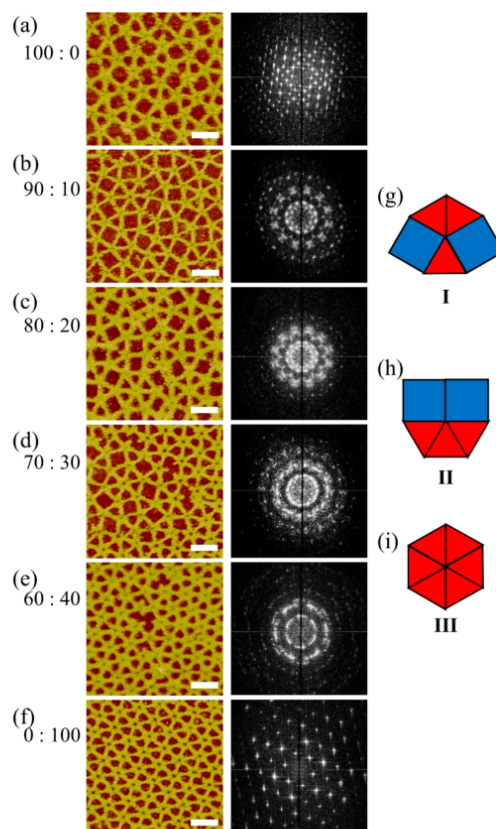

Figure 2. AFM study of b5PS-b6PS binary networks. (a–f) AFM images (left) and corresponding FFT patterns (right) of DNA networks from DNA solutions with indicated b5PS:b6PS ratios. FFT patterns are based on 1 μm × 1 μm AFM images. Scale bar: 50 nm. (g–i) All vertex conformations observed in these networks.

and S16),[16] extending to at least 4 μm × 4 μm and containing over 2.6 × 10^5 b6PS motifs.

The motif compositions in bulk solutions and in the assembled networks on surface are related, but far away from being equal. For example, hexagonal crystals prevails when b5PS:b6PS = 60:40. We have attributed this phenomenon to two factors. (i) Differential motif adsorption. b6PS has larger surface area, thus adsorbs onto mica surfaces more stably than b5PS. (ii) Preferential crystal packing. In the assembled networks, each b6PS interacts with rest of the networks by six branches, and b5PS by five. Thus, the b6PS motif is more stable in the assembled networks than b5PS is. On the other hand, in quasicrystalline networks, b5PS:b6PS on surface is larger than that in bulk solution. Presumably, more b6PS motif is required to disturb the tetragonal crystals (snub square tiling) because tetragonal crystals are more thermostable than quasicrystals.

Fascinating dodecagonal quasicrystals were observed at b5PS:b6PS = 80:20 (Figure 3) and 90:10 (Figure S17) in bulk solution. The corresponding FFT patterns show distinct
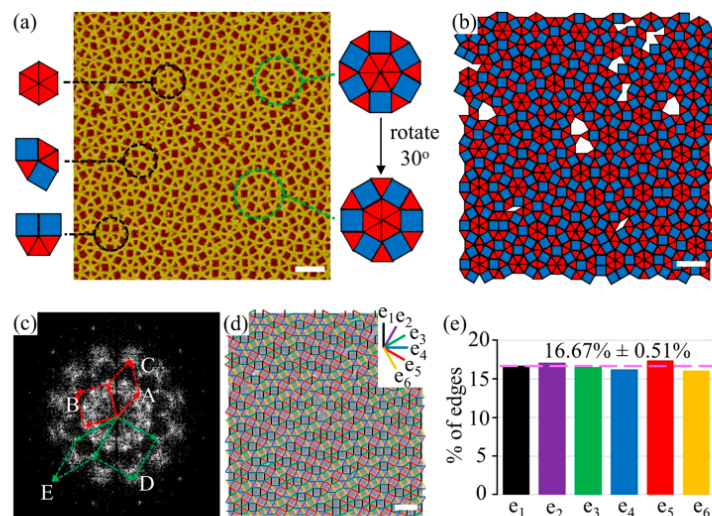
Figure 3. Analysis of dodecagonal quasicrystalline networks assembled from b5PS and b6PS motifs at a ratio of 80:20 in bulk solution. (a) An AFM image of the quasicrystals. Three vertex configurations (corresponding to individual DNA motifs) and two dodecagonal complex motifs with 30° relative rotation are highlighted on the left and right, respectively. (b) Triangle-and-square tiling map of panel a. (c) The FFT pattern of (a). Five concentric rings (A–E) of diffraction spots are related with each other by vector additions. Spots on each ring exhibit a 12-fold symmetry. (d) The edges in tiling map of panel a are distributed in six, color-coded orientations (e_1–e_6). (e) Statistics of the edge orientations. The pink, dashed line indicates the average edge percentage. Scale bar: 100 nm.

12-fold symmetry. Figure 3a illustrates an AFM image of the quasicrystals (b5PS:b6PS = 80:20). b5PS motifs adapt either configuration I ($3^2 \cdot 4 \cdot 3 \cdot 4$) or II ($3^3 \cdot 4^2$) and b6PS motifs adapt configuration III (3^6). Green circles highlight two dodecagonal motifs with 30° rotation relative to each other, confirming the important orientation requirement of dodecagonal tiling (Figure S18). In the FFT pattern, diffraction spots exist on five concentric rings: A, B, C, D, and E from the center to outside (Figure 3c). On each ring, the diffraction spots follow a 12-fold symmetry. Spots on circles A, B, C, D, and E are mutually vector-correlated as deduced in vector arrows. For example, diffraction spots in circle E can be derived from vector addition of two adjacent diffraction spots in circle B. Furthermore, the 12-fold symmetry in FFT pattern exists for large-area of the assembled DNA networks, indicating large domains (4 μm × 4 μm) of the quasicrystals (Figure S12d). In a perfect dodecagonal quasicrystal, the triangle-to-square ratio is $4/\sqrt{3} = 2.31$.[19−21] In the observed AFM image, there are 695 triangles and 301 squares (Figure 3b), resulting in a triangle-to-square ratio of 2.31, the same as the theoretical value. When concerning about the vertices in a perfect dodecagonal quasicrystal, the ratio between b5PS and b6PS should be ~12.9 (Figure S19). The observed ratio is 13.6 [b5PS (598): b6PS (44)], closely matching to the theoretical value. Furthermore, the defect-free quasicrystal lattice accounts for 97.0% of the observed area. Edge-tiling map indicates a near-even distribution of the six, possible edge orientations (an edge is defined by the line connecting two adjacent vertices), which corresponds to the 12-fold symmetry in the FFT pattern (Figure 3d,e).[22] Thus, the assembled DNA networks are close to a near-perfect dodecagonal quasicrystal.

The quasicrystalline networks assembled at ratio of 90:10 also express dodecagonal tiling (Figure S17a). Its triangle

(688)-to-square (302) ratio is 2.28 (Figure S17b), close to the theoretical value 2.31. The b5PS (608):b6PS (35) in observed networks is 17.4, deviating from the theoretical value (12.9) of an infinite, defect-free dodecagonal quasicrystal. Considering the calculated triangle-to-square ratio of 2.28, this quasicrystal should have b5PS:b6PS of 14.3 (Figure S19), which is also smaller than the observed 17.4. It is reasonable because of the low content of b6PS motif in bulk solution compared with that at the motif ratio of 80:20 discussed above, which is also demonstrated by some observed incomplete b6PS motifs (not counted in b5PS:b6PS calculation) in the network. The FFT pattern shows a 12-fold symmetry (Figure S17c), which is also supported by near-even distribution of the edge orientation (Figure S17d,e). Furthermore, the defect-free area accounts for 96.8% of the imaged area. Overall, this network is a less perfect type of dodecagonal quasicrystal.

In the DNA quasicrystals, some interesting motif deformations have been observed. At the motif ratio of 80:20, some b6PS motifs behave like b5PS motifs (Figure S20a), likely because of the excessive b6PS motifs in bulk solution. In this deformed motif, one bridge is broken, thus its flanking two branches are arranged in parallel and function as a single branch when associating with another motif. In contrast, at the motif ratio of 90:10, some b5PS motifs act like b6PS motifs (named pseudo-b6PS motifs, Figure S20b), likely due to the insufficient b6PS motif in bulk solution. In the pseudo-b6PS motif, one bridge tears and the angle between the two adjacent branches turns into 120°. The other four angles are adjusted to 60°. DNA motifs seem able to "smartly" tune their shapes according to the environment. Alternatively, though unlikely, the pseudo-b6PS motif could be a b6PS motif somehow missing one branch.

In summary, we have developed a rational approach to assemble 2D dodecagonal quasicrystals. Similar approaches have been proposed before,[23,24] but remain elusive for experimental demonstration. The key of this study is the ability to fine-tune the rigidity/flexibility balance of the DNA motifs. If too flexible, the DNA motifs will aggregate into random networks; if too rigid, the same motif cannot adapt different conformations needed for quasicrystals. This approach might be adapted for other systems for designing quasicrystals. In addition, it is also possible to stabilize DNA quasicrystals, e.g. by coating the DNA with a thin layer of silica.[25,26] That would allow further applications, e.g. organization of biomolecules or nanoparticles to express their own quasicrystallinity for functional exploration.

■ ASSOCIATED CONTENT

ⓢ Supporting Information

The Supporting Information is available free of charge on the ACS Publications website at DOI: 10.1021/jacs.9b00843.

Materials, methods, nanomotif designs, and additional experimental data (native PAGEs and AFM images) (PDF)

■ AUTHOR INFORMATION

Corresponding Author

*mao@purdue.edu

ORCID ⓞ

Chengde Mao: 0000-0001-7516-8666

Notes

The authors declare no competing financial interest.

■ ACKNOWLEDGMENTS

■ REFERENCES

(1) Shechtman, D.; Blech, I.; Gratias, D.; Cahn, J. W. Metallic Phase with Long-Range Orientational Order and No Translational Symmetry. *Phys. Rev. Lett.* **1984**, *53*, 1951.

(2) Ye, X.; Chen, J.; Eric Irrgang, M.; Engel, M.; Dong, A.; Glotzer, S. C.; Murray, C. B. Quasicrystalline Nanocrystal Superlattice with Partial Matching Rules. *Nat. Mater.* **2017**, *16*, 214.

(3) Paßens, M.; Caciuc, V.; Atodiresei, N.; Feuerbacher, M.; Moors, M.; Dunin-Borkowski, R. E.; Blügel, S.; Waser, R.; Karthäuser, S. Interface-Driven Formation of a Two-Dimensional Dodecagonal Fullerene Quasicrystal. *Nat. Commun.* **2017**, *8*, 15367.

(4) Xiao, C.; Fujita, N.; Miyasaka, K.; Sakamoto, Y.; Terasaki, O. Dodecagonal Tiling in Mesoporous Silica. *Nature* **2012**, *487*, 349.

(5) Wasio, N. A.; Quardokus, R. C.; Forrest, R. P.; Lent, C. S.; Corcelli, S. A.; Christie, J. A.; Henderson, K. W.; Kandel, S. A. Self-Assembly of Hydrogen-Bonded Two-Dimensional Quasicrystals. *Nature* **2014**, *507*, 86.

(6) Urgel, J. I.; Écija, D.; Lyu, G.; Zhang, R.; Palma, C.-A.; Auwärter, W.; Lin, N.; Barth, J. V. Quasicrystallinity Expressed in Two-Dimensional Coordination Networks. *Nat. Chem.* **2016**, *8*, 657.

(7) Penrose, R. Pentaplexity: A Class of Non-Periodic Tilings of the Plane. *Math. Intell.* **1979**, *2*, 32.

(8) Stampfli, P. A Dodecagonal Quasi-Periodic Lattice in 2 Dimensions. *Helv. Phys. Acta* **1986**, *59*, 1260.

(9) Zhou, Z.; Harris, K. D. M. Design of a Molecular Quasicrystal. *ChemPhysChem* **2006**, *7*, 1649.

(10) Rothemund, P. W. K. Folding DNA to Create Nanoscale Shapes and Patterns. *Nature* **2006**, *440*, 297.

(11) Yan, H.; Park, S. H.; Finkelstein, G.; Reif, J. H.; LaBean, T. H. DNA-Templated Self-Assembly of Protein Arrays and Highly Conductive Nanowires. *Science* **2003**, *301*, 1882.

(12) He, Y.; Chen, Y.; Liu, H.; Ribbe, A. E.; Mao, C. Self-Assembly of Hexagonal DNA Two-Dimensional (2D) Arrays. *J. Am. Chem. Soc.* **2005**, *127*, 12202.

(13) Ke, Y.; Ong, L. L.; Shih, W. M.; Yin, P. Three-Dimensional Structures Self-Assembled from DNA bricks. *Science* **2012**, *338*, 1177.

(14) Benson, E.; Mohammed, A.; Gardell, J.; Masich, S.; Czeizler, E.; Orponen, P.; Högberg, B. DNA Rendering of Polyhedral Meshes at the Nanoscale. *Nature* **2015**, *523*, 441.

(15) Winfree, E.; Liu, F.; Wenzler, L. A.; Seeman, N. C. Design and Self-Assembly of Two-Dimensional DNA Crystals. *Nature* **1998**, *394*, 539.

(16) He, Y.; Tian, Y.; Ribbe, A. E.; Mao, C. Highly Connected Two-Dimensional Crystals of DNA Six-Point-Stars. *J. Am. Chem. Soc.* **2006**, *128*, 15978.

(17) Liu, L.; Li, Y.; Wang, Y.; Zheng, J.; Mao, C. Regulating DNA Self-Assembly by DNA−Surface Interactions. *ChemBioChem* **2017**, *18*, 2404.

(18) Zhang, C.; Su, M.; He, Y.; Zhao, X.; Fang, P.-a.; Ribbe, A. E.; Jiang, W.; Mao, C. Conformational Flexibility Facilitates Self-Assembly of Complex DNA Nanostructures. *Proc. Natl. Acad. Sci. U. S. A.* **2008**, *105*, 10665.

(19) Leung, P. W.; Henley, C. L.; Chester, G. V. Dodecagonal Order in a Two-Dimensional Lennard-Jones System. *Phys. Rev. B: Condens. Matter Mater. Phys.* **1989**, *39*, 446.

(20) Kawamura, H. Statistics of Two-Dimensional Amorphous Lattice. *Prog. Theor. Phys.* **1983**, *70*, 352.

(21) Oxborrow, M.; Henley, C. L. Random Square-Triangle Tilings: A Model for Twelvefold-Symmetric Quasicrystals. *Phys. Rev. B: Condens. Matter Mater. Phys.* **1993**, *48*, 6966.

(22) Ishimasa, T. Dodecagonal Quasicrystals Still in Progress. *Isr. J. Chem.* **2011**, *51*, 1216.

(23) van der Linden, M. N.; Doye, J. P. K.; Louis, A. A. Formation of Dodecagonal Quasicrystals in Two-Dimensional Systems of Patchy Particles. *J. Chem. Phys.* **2012**, *136*, 054904.

(24) Reinhardt, A.; Schreck, J. S.; Romano, F.; Doye, J. P. K. Self-Assembly of Two-Dimensional Binary Quasicrystals: A Possible Route to a DNA Quasicrystal. *J. Phys.: Condens. Matter* **2017**, *29*, 014006.

(25) Liu, X.; Zhang, F.; Jing, X.; Pan, M.; Liu, P.; Li, W.; Zhu, B.; Li, J.; Chen, H.; Wang, L.; Lin, J.; Liu, Y.; Zhao, D.; Yan, H.; Fan, C. Complex Silica Composite Nanomaterials Templated with DNA Origami. *Nature* **2018**, *559*, 593−598.

(26) Liu, L.; Zheng, M.; Li, Z.; Li, Q.; Mao, C. Patterning Nanoparticles with DNA Molds. *ACS Appl. Mater. Interfaces* ASAP (online released Feb. 22, 2019). DOI: 10.1021/acsami.8b22691.